Experimental and Modeling Studies of the Combustion Characteristics of Conventional and Alternative Jet Fuels

Final Report

Ellen Meeks, Chitral V. Naik, Karthik V. Puduppakkam, and Abhijit Modak
Reaction Design, San Diego, California

Fokion N. Egolfopoulos and Theo Tsotsis
University of Southern California, Los Angeles, California

Charles K. Westbrook
Reaction Design, Livermore, California

NASA STI Program . . . in Profile

Since its founding, NASA has been dedicated to the advancement of aeronautics and space science. The NASA Scientific and Technical Information (STI) program plays a key part in helping NASA maintain this important role.

The NASA STI Program operates under the auspices of the Agency Chief Information Officer. It collects, organizes, provides for archiving, and disseminates NASA's STI. The NASA STI program provides access to the NASA Aeronautics and Space Database and its public interface, the NASA Technical Reports Server, thus providing one of the largest collections of aeronautical and space science STI in the world. Results are published in both non-NASA channels and by NASA in the NASA STI Report Series, which includes the following report types:

- TECHNICAL PUBLICATION. Reports of completed research or a major significant phase of research that present the results of NASA programs and include extensive data or theoretical analysis. Includes compilations of significant scientific and technical data and information deemed to be of continuing reference value. NASA counterpart of peer-reviewed formal professional papers but has less stringent limitations on manuscript length and extent of graphic presentations.

- TECHNICAL MEMORANDUM. Scientific and technical findings that are preliminary or of specialized interest, e.g., quick release reports, working papers, and bibliographies that contain minimal annotation. Does not contain extensive analysis.

- CONTRACTOR REPORT. Scientific and technical findings by NASA-sponsored contractors and grantees.

- CONFERENCE PUBLICATION. Collected papers from scientific and technical conferences, symposia, seminars, or other meetings sponsored or cosponsored by NASA.

- SPECIAL PUBLICATION. Scientific, technical, or historical information from NASA programs, projects, and missions, often concerned with subjects having substantial public interest.

- TECHNICAL TRANSLATION. English-language translations of foreign scientific and technical material pertinent to NASA's mission.

Specialized services also include creating custom thesauri, building customized databases, organizing and publishing research results.

For more information about the NASA STI program, see the following:

- Access the NASA STI program home page at *http://www.sti.nasa.gov*

- E-mail your question via the Internet to *help@ sti.nasa.gov*

- Fax your question to the NASA STI Help Desk at 443–757–5803

- Telephone the NASA STI Help Desk at 443–757–5802

- Write to:
  NASA Center for AeroSpace Information (CASI)
  7115 Standard Drive
  Hanover, MD 21076–1320

NASA/CR—2011-216356

Experimental and Modeling Studies of the Combustion Characteristics of Conventional and Alternative Jet Fuels
Final Report

Ellen Meeks, Chitral V. Naik, Karthik V. Puduppakkam, and Abhijit Modak
Reaction Design, San Diego, California

Fokion N. Egolfopoulos and Theo Tsotsis
University of Southern California, Los Angeles, California

Charles K. Westbrook
Reaction Design, Livermore, California

National Aeronautics and
Space Administration

Glenn Research Center
Cleveland, Ohio 44135

May 2011

Level of Review: This material has been technically reviewed by NASA technical management.

Contents

List of Tables

List of Figures

Experimental and Modeling Studies of the Combustion Characteristics of Conventional and Alternative Jet Fuels

Final Report

Ellen Meeks, Chitral V. Naik, Karthik V. Puduppakkam, and Abhijit Modak
Reaction Design
San Diego, California 92121

Fokion N. Egolfopoulos and Theo Tsotsis
University of Southern California
Los Angeles, California 90089

Charles K. Westbrook
Reaction Design
Livermore, California 94550

1.0   Overview of Project Objectives

The objectives of this project have been to develop a comprehensive set of fundamental data regarding the combustion behavior of jet fuels and appropriately associated model fuels. Based on the fundamental study results, an auxiliary objective was to identify differentiating characteristics of molecular fuel components that can be used to explain different fuel behavior and that may ultimately be used in the planning and design of optimal fuel-production processes.

The fuels studied in this project were Fischer-Tropsch (F-T) fuels and biomass-derived jet fuels that meet certain specifications of currently used jet propulsion applications. Prior to this project, there were no systematic experimental flame data available for such fuels. One of the key goals has been to generate such data, and to use this data in developing and verifying effective kinetic models. The models have then been reduced through automated means to enable multidimensional simulation of the combustion characteristics of such fuels in real combustors. Such reliable kinetic models, validated against fundamental data derived from laminar flames using idealized flow models, are key to the development and design of optimal combustors and fuels. The models provide direct information about the relative contribution of different molecular constituents to the fuel performance and can be used to assess both combustion and emissions characteristics.

2.0   Executive Summary of Results

Throughout this project, Reaction Design has collaborated closely with researchers at the University of Southern California (USC) and Dr. Charles Westbrook, a consultant to Reaction Design, in the analysis and testing of jet fuels and fuel surrogates. Led by Professors Egolfopoulos and Tsotsis, USC performed fundamental combustion studies that directly compared the combustion behavior of alternative jet fuels with conventional fuels, such as JP-7 and JP-8, in terms of flame-propagation and flame-extinction characteristics. These experiments provided insight into the differences and similarities between the different fuels. In addition, extensive flame experiments were performed on candidate surrogate-fuel components, as well as selected surrogate-fuel blends. The focus on surrogate fuels allowed verification and improvement of detailed kinetics mechanisms for these fuel components, through comparison of one-dimensional flame simulations with data from the USC experiments. The flame experiments were designed to facilitate accurate simulation of the flow-field using such one-dimensional models, allowing focus on kinetics and species-transport effects. The collaboration between Reaction Design and USC

involved iterative comparisons between data and model that led to the discovery of issues with the experimental procedures as well as with the chemistry models; improvements to both were important outcomes of the project.

Reaction Design's efforts were centered on assembling and improving the kinetics mechanism for the fuel surrogates, using both the fundamental data provided by USC as well as supplementary data available from the literature for non-flame conditions. As part of this activity, simulations were performed for a wide variety of experimental conditions, as well as a wide range of temperatures and equivalence ratios for fuel/air mixtures. A new flame-extinction model was tested during the project, supplementing the flame-speed calculation capabilities already available in CHEMKIN-PRO (Ref. 1). These two models provided complementary tests of the high-temperature kinetics representation in the mechanisms. Another result of the project was the demonstration of flame simulations using a comprehensive soot-formation model, including prediction of particle-size distribution functions. From the literature, shock-tube measurements of ignition and stirred-reactor measurements of species profiles were obtained and modeled to provide a more comprehensive test of the models' predictive capabilities. The results of these activities include well validated models of key fuel components that are important to modeling alternative jet fuels.

In addition to fundamental experiments and detailed-kinetics mechanism validation, two other tasks were undertaken as part of this project. One was the testing of a systematic method for matching a surrogate-fuel blend to a real fuel, based on chemical analysis and physical properties of the targeted fuel. The other task was to take the final "master" mechanism for our surrogate fuel blends and perform automated mechanism reduction over a range of conditions that would be appropriate for jet combustor simulations. A skeletal approach was taken to mechanism reduction, based on the Directed Relation Graph Method (Refs. 2 and 3). The results of these activities are a recommended surrogate blend for typical F-T and bio-derived jet fuels, as well as a validated and reduced mechanism for that surrogate, ready for use in combustor simulations.

Several general observations and conclusions can be made from the results of this study. These are summarized as follows:

1. In comparing F-T fuels to bio-derived jet fuels, we find almost no discernible difference in the combustion behavior, based on the limited samples available for the bio-derived jet fuel. This is largely due to the strict jet-fuel standard that both alternative fuels must meet, but also due to the chemical nature of the process used to produce the bio-derived fuel. Fuels derived from plant oils are typically in the form of long-chain methyl esters. To meet the jet-fuel requirements, these are further processed (through hydrogenation) to remove the oxygen from the oxygenate compounds. This processing results in a dominant composition of long-chain alkane molecules, very similar to what the chemical analysis showed for F-T jet fuels.

2. Similarly, despite significant differences in the chemical analysis results for two different F-T fuels, particularly in carbon-number distribution, the combustion behavior measured for the two fuels appears to be identical. This can be explained by the very similar combustion behavior observed for different long-chain, unbranched alkane molecules that have chain length greater than ~6. In this way, different distributions of alkane chain length do not have a significant effect on flame propagation or flame extinction, although modeling studies suggest they might affect the quantitative degree of NO_x production.

3. In experimentally comparing the alternative fuels with JP-7 and JP-8, we find that the alternative fuels have almost the same flame-propagation speed as JP-7 and that the flame speed for JP-7 is slightly higher than for JP-8. This is consistent with JP-8 fuel containing more aromatic compounds than JP-7 (or than the F-T and bio-derived fuels), which tends to lower the flame speed. For flame-extinction measurements, a similar trend is apparent, although the difference in extinction between JP-7 and JP-8 is smaller in that case and close to experimental uncertainty for those measurements.

4. In comparing the flame-propagation and flame-extinction behavior of the normal alkane, *n*-dodecane, which matches the typical average carbon number of an F-T fuel, with the same

measurements for the alternative and conventional jet fuels, we find that *n*-dodecane has about the same laminar flame speeds and slightly higher resistance to extinction. This makes *n*-dodecane a reasonable single-component surrogate for all of these fuels under some conditions. However, a multicomponent surrogate blend is needed to match other fuel properties, such as cetane number, NO_x emissions, and sooting propensity.

5. Laminar flame-speed, flame-extinction strain rate, ignition time, autoignition temperature, NO_x and other species-concentration measurements are well predicted by the chemistry models developed for *n*-alkane/*iso*-alkane surrogate blends. In most cases, predictions are within experimental uncertainty of the data. The mechanisms underwent significant improvement during the project. The only area where the mechanisms provide mixed results is for PAH and soot predictions, but systematic improvement of these mechanisms was beyond the scope of this project.

6. Surrogate blends are recommended for F-T blends that consist of mixtures of *n*-dodecane, *n*-decane, and *iso*-octane. Specific compositions have been proposed for two different F-T fuels that provide a best match to cetane number, H/C ratio, lower heating value, T50 boiling point, and chemical-analysis data. Tests of these blends against experimental data for flame-propagation and flame-extinction strain rate show good agreement.

7. A successful reduction of the high-temperature mechanism has been achieved that provides a ~90 percent reduction in the number of species without loss of accuracy in model predictions over a range of temperatures and equivalence ratios.

The remainder of this report provides technical details on the methods employed in each of the tasks performed under the project, as well as the data and results that support the conclusions from this study.

3.0   Technical Discussion

The 2-year project was divided into several technical tasks, with the first year's tasks providing the foundation necessary to achieve the second year's goals. The following provides detailed description of the methods used for experiment and modeling, as well as the final data obtained in each task.

3.1   Survey of Alternative Fuels and Their Chemical Properties

To understand how best to represent alternative jet fuels with a detailed kinetics model, we first sought to collect as much data as possible on the chemical composition and properties of the fuels. We were interested in both F-T jet fuels as well as biomass-derived jet fuels, which had been certified by the Air Force for jet applications. Through external collaboration between the Air Force Research Laboratory (AFRL) and USC, we were easily able to obtain the desired information for F-T fuels. Data on bio-derived fuels proved much more difficult to obtain, due to the proprietary nature of the processes currently in development for such fuels and the limited number of facilities involved with jet-fuel production. However, the AFRL was able to provide a fuel sample that USC could test in the flame experiments as well as some qualitative information about the chemical properties. This allowed us to make some comparisons and draw some conclusions about the differences between the different alternative fuels. Data obtained on specific fuel properties are described below.

3.1.1   Fischer-Tropsch Fuels

During the first year of the project, the AFRL provided USC with a F-T fuel for testing in the USC Combustion and Fuels Laboratory. This particular fuel is labeled by AFRL as S-8 with a designated code POSF 4734. The AFRL had performed detailed analysis of the F-T fuel with a gas chromatography—mass spectrometry method. Later in the project, a second sample was obtained from AFRL, which was labeled F-T 5172 and is from Shell.

The results of the detailed qualitative analysis for S-8 are provided in Table 1, and it can be seen that the composition is dominated by *n*- and *iso*-paraffins, consisting of C_8 to C_{15} chains. The numbered peaks are the largest peak areas recorded on the total ion chromatogram (1 percent or higher). It was noted that these areas are raw-data areas and have not been calibrated with a standard. Lettered peaks are for components between 0.7 and 1 percent, which were examined when the chromatography was good. Double lettered peaks are very early eluting components that were included to provide a suite of light components for model development. These peaks were chosen in part for their elution order and in part for their chromatographic purity.

TABLE 1.—DETAILED ANALYSIS FOR S-8, POSF 4734, USING GAS CHROMATOGRAPHY PROVIDED BY AFRL

Peak no.	Retention time, min	Peak profile	Correlation coefficient	Confidence	Name	CAS no.	Area %
aa	2.119	S	72.2	H	2-methyl heptane	592-27-8	0.323
bb	2.162	A	41.4	H	3-methyl heptane	589-81-1	0.437
a	2.310	A	26.3	H	1,2,3-trimethyl cyclopentane	15890-40-1	0.965
1	2.564	A	44.2	H	2,5-dimethyl heptane	2216-30-0	1.131
2	2.803	A	33.9	H	4-methyl octane	2216-34-4	2.506
3	2.869	A	16.9	H	3-methyl octane	2216-33-3	1.323
4	3.123	A	21.6	H	*n*-nonane	111-84-2	1.623
5	3.358	A	18.5	M	3,5-dimethyl octane	15869-96-9	1.035
b	3.456	A	29.0	H	2,6-dimethyl octane	2051-30-1	0.756
6	3.682	A	54.4	H	4-ethyl octane	15869-86-0	1.032
7	3.757	A	39.8	H	4-methyl nonane	17301-94-9	1.904
8	3.792	S	39.2	H	2-methyl nonane	871-83-0	1.019
9	3.866	A	26.9	H	3-methyl nonane	5911-04-6	1.385
10	4.186	A	51.4	H	*n*-decane	124-18-5	2.050
11	4.390	A	16.7	M	2-5-dimethyl nonane	17302-27-1	1.175
12	4.750	S	12.0	M	5-ethyl-2-methyl octane	62016-18-6	1.015
13	4.820	A	37.7	H	5-methyl decane	13151-35-4	1.315
14	4.859	A	42.1	H	4-methyl decane	2847-72-5	1.134
15	4.902	A	35.4	H	2-methyl decane	6975-98-0	1.529
16	4.980	A	44.1	H	3-methyl decane	13151-34-3	1.583
17	5.312	A	50.1	H	*n*-undecane	1120-21-4	2.420
c	5.484	A	NA	M	x-methyl undecane	NA	1.590
18	5.664	A	11.9	M	3-methyl undecane	1002-43-3	1.15
19	5.906	A	37.3	H	5-methyl undecane	1632-70-8	1.696
20	5.949	A	29.5	H	4-methyl undecane	2980-69-0	1.045
21	5.996	A	15.1	M	2-methyl undecane	7045-71-8	1.072
22	6.074	A	7.9	U	2,3-dimethyl undecane	17312-77-5	1.213
23	6.387	A	43.9	H	*n*-dodecane	112-40-3	2.595
d	6.606	A	8.3	M	4-methyl dodecane	6117-97-1	0.929
e	6.668	A	NA	H	x-methyl dodecane	NA	0.744
24	7.024	S	28.7	H	2-methyl dodecane	1560-97-0	1.293
25	7.094	S	NA	M	x-methyl dodecane	NA	1.281
28	7.383	A	36.0	H	*n*-tridecane	629-50-5	1.739
f	7.923	A	8.7	U	4-methyl tridecane	26730-12-1	0.836
29	7.970	A	9.8	U	6-propyl tridecane	55045-10-8	1.052
30	8.040	A	NA	M	x-methyl tridecane	NA	1.066
31	8.306	A	23.3	H	*n*-tetradecane	629-59-4	1.562
32	8.396	A	NA	M	x-methyl tetradecane	NA	1.198
g	8.490	S	6.4	M	5-methyl tetradecane	25117-32-2	0.720
33	8.728	S	10.2	H	*n*-pentadecane	629-62-9	1.032
H	9.232	A	NA	M	x-methyl tetradecane	NA	0.727

Several cautions apply to these analyses, which were recorded in internal AFRL reports. The first column is the peak designator. The second column provides the retention time in minutes, obtained from the total ion chromatogram at the peak apex. The peak profile chosen for analysis is next, and is either "S" (for a single slice through the chromatographic peak) or "A" (for an average over all or part of the chromatographic peak). The correlation coefficient is a fit parameter provided by the software used in the analysis, while the confidence (H, for high, M, for medium, and U for uncertain) is assigned on the basis of many chromatographic and mass spectral features, and is subjective. The remaining table entries are self explanatory. It should be noted that occasionally, one cannot discern the isomerization from the mass spectrum. In these instances, the position of a branch is left as a variable x (such as x-methyl dodecane; the position of the methyl group is uncertain, even if there is a high level of confidence in the assignment). The main application of the detailed analysis is to provide a framework for the modeling. In this respect, even if there were a large number of such minor uncertainties, it will not be problematic.

The analysis of the F-T 5172 fuel composition was also obtained from AFRL and is shown in comparison to another sample of the previous F-T fuel (S-8) in Figure 1. Here we can see that the Shell fuel (F-T 5172) is similar in chemical class composition, but has a narrower molecular weight range and is missing the C_{12} and greater fractions. This difference suggested that an appropriate surrogate-fuel composition would need to be determined for each specific fuel. In other words, one fuel surrogate definition might not be appropriate for all F-T fuels, depending on which characteristics of the fuel and the combustion behavior need to be modeled. On the other hand, both F-T fuels had the same ignition characteristics, as measured by cetane number, with a value of ~60, and both fuels had a H:C ratio of about 2.2. A summary of some of the other properties obtained for these fuels is given in Table 2. All of this information was important input to the determination of appropriate surrogate-fuel blends, as discussed further below.
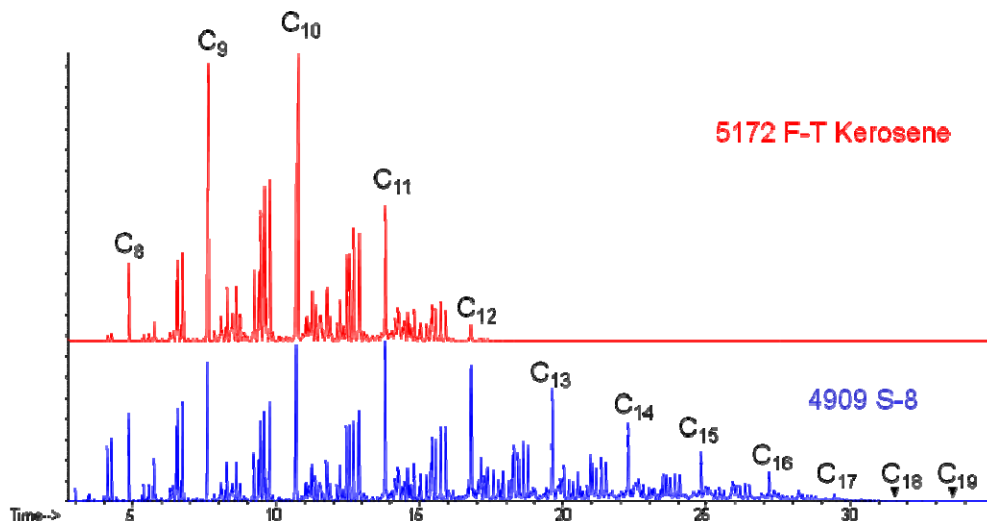
Figure 1.—Comparison of fuel analysis for the new F-T 5172 (Shell) sample versus the previously analyzed F-T fuel (S-8).

TABLE 2.—OTHER MEASURED PROPERTIES
FOR THE F-T FUEL SAMPLES

Fuel property	Shell GTL	S-8
Cetane number	61	60
H/C molar ratio	2.17	2.17
Lower heating value, MJ/kg	44.14	44.14
T50 boiling point, K	445	474
T20 boiling point, K	433	449
T90 boiling point, K	456	522

3.1.2 Biomass-Derived Jet Fuels

During this project, USC contacted many fuel manufacturers concerning existing and emerging processes for production of various biofuels in order to compile technical specifications of existing processes. They identified a new process developed by UOP, which involves the catalytic deoxygenation of biologically derived feedstocks. The process, branded "Ecofining" by UOP, results in a renewable fuel called "green diesel." This fuel is an alternative to both standard petroleum diesel and biodiesel and may be acceptable as a jet fuel. The process involves processing vegetable oil through a catalytic reaction with hydrogen as the reactant in order to remove the oxygen contained in the oil. Typically, vegetable oil consists primarily of triglycerides with 1 to 2 percent free fatty acids, and contains 10 to 12 wt% oxygen. The removal of oxygen results in an *iso*-paraffin-rich oil that is free from aromatics and sulfur. Propane and naphtha are potentially marketable co-products of the Ecofining process, while water and carbon oxides are the undesirable by-products.

The yield of diesel fuel by the UOP process can range from 88 to 99 liquid vol%, dependent upon the feedstock type and operating severity. "Green diesel" has the benefit, according to UOP, of having a high cetane number (70 to 90), good cold-flow properties, and a heating value comparable to petroleum diesel (green diesel 44 MJ/kg, petroleum diesel 43 MJ/kg). A full-scale production facility is currently being constructed in Italy, in collaboration between UOP and the European refiner ENI, and the plan is for the facility to come online in 2009. However, a production output of only 6500 barrels per day is planned at the initial start-up. This facility will be the only commercial manufacturer, using the Ecofining process, to produce "green diesel."

A request for a 3 to 4 liter sample of "green diesel" was sent to the director of UOP's Renewable Energy & Chemicals business unit, and a sample was obtained for experimental testing at USC. Although detailed chemical analysis of the sample was not possible, the application of elution techniques confirmed that the sample had about 4 percent esters, compared to ~95 percent for biodiesel fuels. Based on the known chemical characteristics of biodiesel and this result, we would expect to have a very similar chemical composition to the F-T fuels described above.

Later in the project, Dr. Tim Edwards of AFRL provided USC with R-8, a certified jet "biofuel." The feedstock for this fuel is an animal fat/vegetable oil blend from Tyson, which is hydrotreated and is very similar to the S-8, which is the standard F-T fuel that has been tested in the past. The R-8 fuel was made by Syntroleum and it is very similar to the UOP fuels previously obtained by USC, as well as to the other F-T fuel samples. The chemical composition of the R-8 fuel was reported by AFRL to be very similar to R-8, although detailed results were again not available.

3.2   Fundamental Combustion Studies of Jet Fuels and Alternative Fuels

3.2.1   Experimental Methods and Facility Description

In the first year of this project, USC designed a heated counterflow burner for the fundamental combustion studies of conventional and alternative jet fuels; a general schematic of this burner design is shown in Figure 2. This burner system is unique in that it contains both internal liquid heating and external heating by ceramic heaters. The burner can be heated up to 300 °C. The design will ensure temperature uniformity throughout the reactant gas lines. In addition, the internal liquid heat also serves to regulate nozzle temperatures over time. The burner system consists of two concentric nozzles and can use three different nozzle diameters, 7, 14, and 22 mm, to cover a wide range of flow conditions. In addition, each nozzle is aerodynamically shaped so the flow is of a flat top at the exit of the nozzle. The overall experimental configuration is shown in Figure 3. The fuel is injected into the first mixing chamber along with heated nitrogen and the mixture is further heated in both the first and the second mixing chambers, which are maintained at high temperatures using electrically heated elements surrounding their walls. Subsequently, sampling is performed to determine the composition of the mixture using Gas Chromatography (GC).
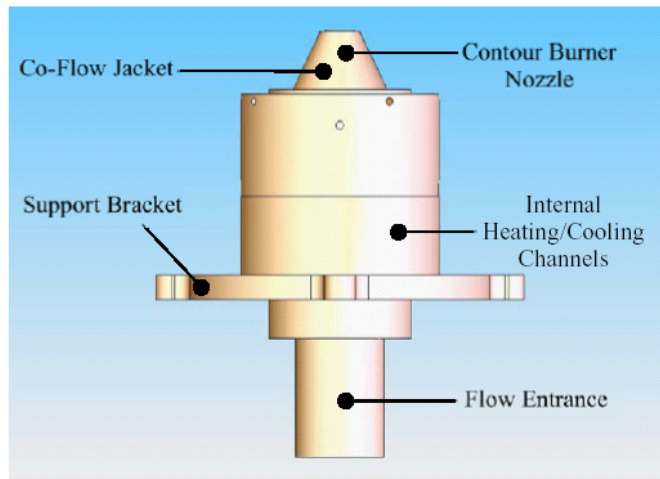
Figure 2.—Schematic of the heated burner.
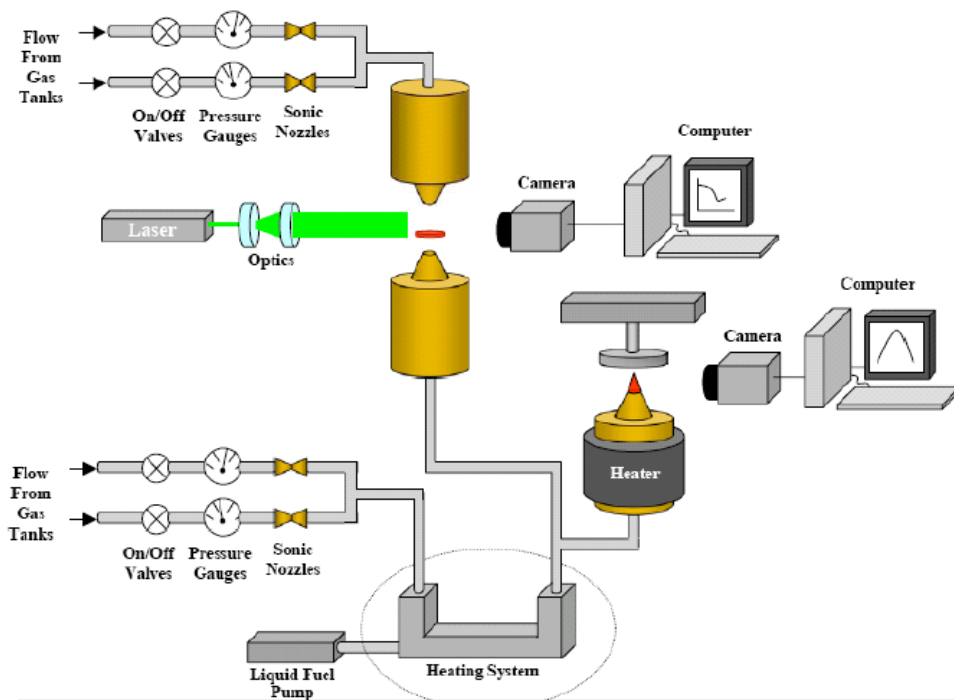
Figure 3.—Overall experimental configuration.

Figure 4.—Stable bunsen flame.

The development of the system included several challenges. The main ones pertain to achieving steady operation while maintaining the fuel unreacted until it reaches the burner. These are two partially contradicting requirements. Achieving steady flow requires that the vaporization is obtained rapidly, which in turn implies that the temperatures of the vaporization chamber have to be high. On the other hand, high temperatures can result in fuel cracking and this has been confirmed experimentally. So it required several iterations through trial and error as well as design modifications to achieve those goals. As a result the flames are stable, as shown in Figure 4, and the fuels are uncracked as has been confirmed through detailed gas chromatography analysis.

The experiments utilize steady, laminar, planar premixed and non-premixed flames that are stabilized in the counterflow configuration. For laminar flame-speed determination, the twin-flame technique is employed, which involves two identical counter-flowing fuel/air jets establishing two symmetrical, planar, near adiabatic flames. The premixed extinction configuration involves a N_2 jet counter-flowing against an opposing fuel/air jet resulting in a single premixed flame.

Flow-field measurements were performed using the digital particle image velocimetry (DPIV) and the laser Doppler velocimetry (LDV) techniques. The axial velocity profile along the stagnation streamline is measured, and the absolute value of the maximum velocity gradient just upstream of the flame is determined as the local strain rate, K. For flame speed measurements, the minimum point of the velocity profile is chosen as a reference upstream flame speed $S_{u,\mathrm{ref}}$, corresponding to the imposed stretch rate K. Thus by plotting $S_{u,\mathrm{ref}}$ against K, the laminar flame speed S_u^o can be determined through extrapolation to $K = 0$. For premixed extinction, K is determined on the fuel/air jet. Extinction strain rates, K_{ext}, cannot be directly measured due to the fact that at the extinction condition, the flow-field is unstable and the flame goes out. To avoid extrapolations in the determination of the K_{ext}, a flame is established for a near-extinction condition, and the prevailing K is measured. Subsequently, the fuel flow rate in the fuel/air jet is slightly modified to achieve extinction.

A vaporization system is used to convert the liquid into vapor prior to entering the burners. This is accomplished by injecting the liquid fuel into a vaporization chamber as shown in Figure 5, with a preheated N_2 coflow. Oxygen is subsequently added to the exit flow to create a fuel/air mixture at the required equivalence ratio. The reactant gas lines, all the way to the burner exit, are maintained at elevated temperatures to ensure that the partial pressure of the liquid fuel is maintained below its vapor pressure to prevent condensation.
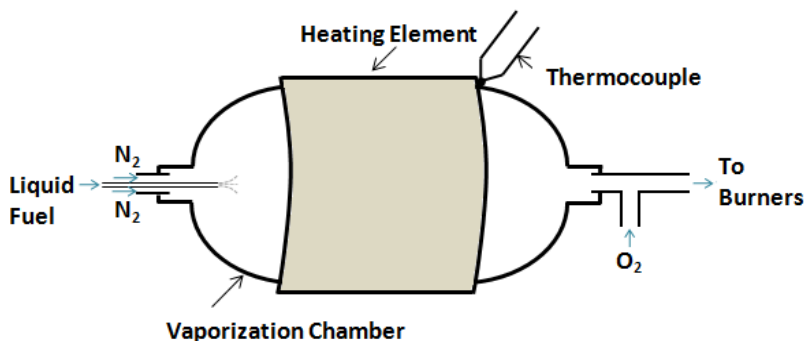
Figure 5.—Schematic of the vaporization process for the flame experiments involving liquid fuels.
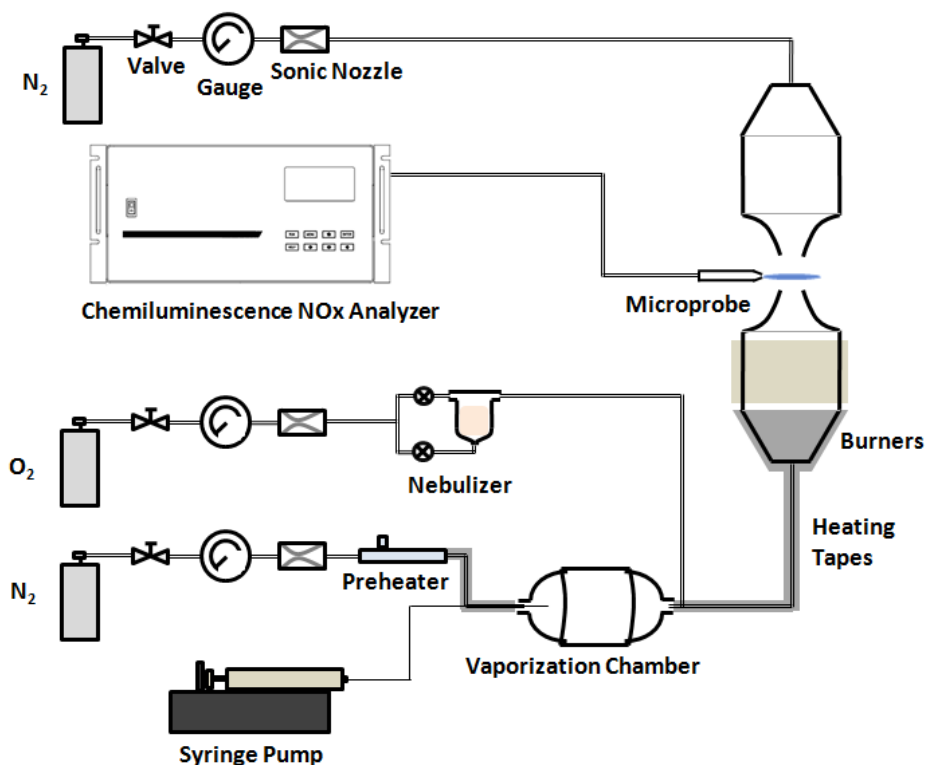
Figure 6.—USC heated counter-flow burner rig used for NO_x measurements.

A NO_x sampling system was also constructed. A water-cooled quartz microprobe that is connected to a vacuum pump is used to withdraw the sample, as shown schematically in Figure 6. The sample is directed afterwards through Teflon tubing towards a Chemiluminescence NO_x Analyzer. The microprobe is mounted on a linear stage thus allowing it to be vertically adjustable and, therefore, enabling us to determine the NO_x concentration structures throughout the flame. The Chemiluminescence analyzer is of high accuracy with a lower detectable limit of 0.05 ppm. A new probe positioning system that includes a Cathetometer was later established to accurately locate the initial position of the probe within 25 μm, therefore eliminating a major experimental uncertainty.

3.2.2 Uncertainties Identified and Addressed in Initial Experimental System

Despite the care in the design of the burner system, USC discovered some issues with reproducibility for the liquid-fuel experiments, discovered due to the duplication of facilities and operation by two different students. As a result, USC undertook a very thorough study of the reproducibility and reliability

of the experimental procedures used to handle heavy (liquid) hydrocarbon fuels in flame experiments. These experiments are difficult and they have learned that, without such care and rigorous testing of assumptions, it is relatively easy to produce data that are neither reliable nor accurate. With a focus on scientific integrity of the methods being used, then, USC spent significant time reviewing the measurements to assure that they were of the highest quality. One outcome of this study was a re-design of the vaporization system to provide more reliable vaporization-without-cracking of the liquid fuels. They also determined the effect of the thermal boundary layer near the burner and the sensitivity of the measurement to the radial location of the probe. These additional studies provided a much better idea of the uncertainty and potential pitfalls for these types of measurements. In addition, a deeper understanding of the experimental sensitivities enables better use of the data in model development and validation. Details of the system upgrades are provided below.

3.2.3 Vaporization System Upgrade

The upgraded vaporization system has the capability to handle heavier liquid fuels, including real biodiesels. The stainless steel vaporization chamber used previously was substituted with a glass chamber to prevent cracking and coking at high temperatures. Additionally, a quartz nebulizer with a flush capillary-lapped nozzle has been integrated to the system to introduce the fuel as a fine aerosol into the chamber; details are shown in Figure 7. Photographs of the actual setup are also shown in Figure 8. This allows for complete vaporization to occur at lower temperatures. The result is more constant vaporization and the prevention of fuel cracking.
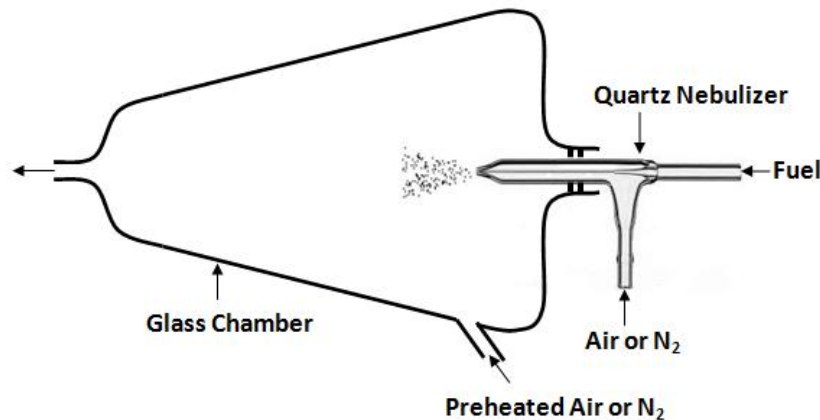
Figure 7.—Schematic of the upgraded vaporization system.
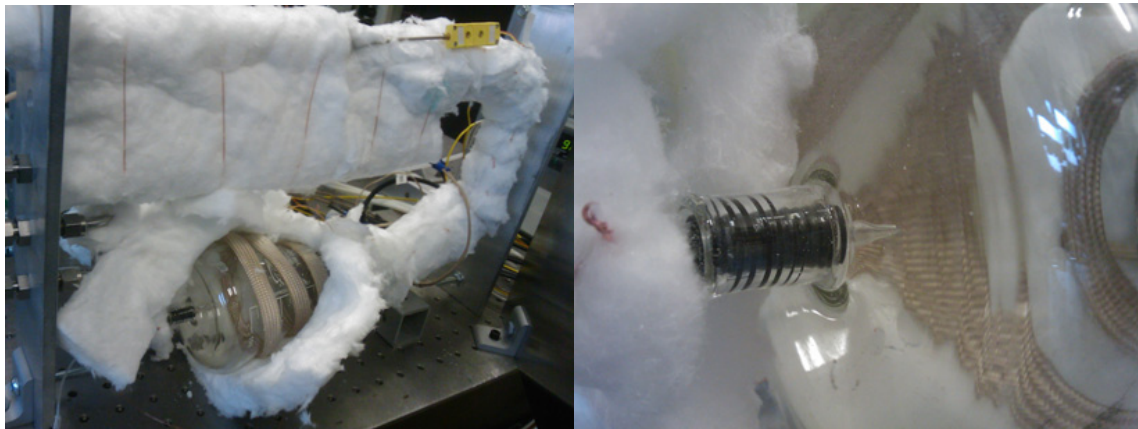
Figure 8.—Photographs of the upgraded vaporization system.

3.2.4 Effect of Thermal Boundary Layer on Radial Temperature Profile

In addition to vaporization, USC undertook a thorough investigation of the effects of thermal boundary layers in the burner on the measurement of laminar flame speeds and extinction strain rates. Figure 9 depicts the configuration of the heated burner used for the current experiments. To attain an unburned gas temperature of ~130 °C for the lower jet, the burner walls are heated with high-performance ceramic heating jackets. When the entire system reaches thermal steady state, the temperatures of the burner and nozzle walls are ~150 and 140 °C, respectively. The unburned gas temperature is measured at the center of the nozzle with an uncoated R-type thermocouple. The tip of the thermocouple is 0.1 mm in diameter, and can provide fast response and highly accurate measurements.

Due to the heat transfer between the nozzle wall and the fuel/air mixture, the radial temperature profile at the exit of the nozzle is non-uniform, as shown in Figure 10. The non-uniformity is more severe at higher exit temperatures. This thermal boundary layer directly affects the velocity profile of the jet, and hence the shape of the flame, as shown in Figure 11. Therefore, the measurement point for velocity should be aligned very carefully to the burner centerline. Otherwise the non-uniform velocity profile may introduce errors into the reference flame speed's measurement. For example, accidental placement of the laser probe 1 to 2 mm away from the system centerline can result in higher reference flame speeds due to thermal effects.
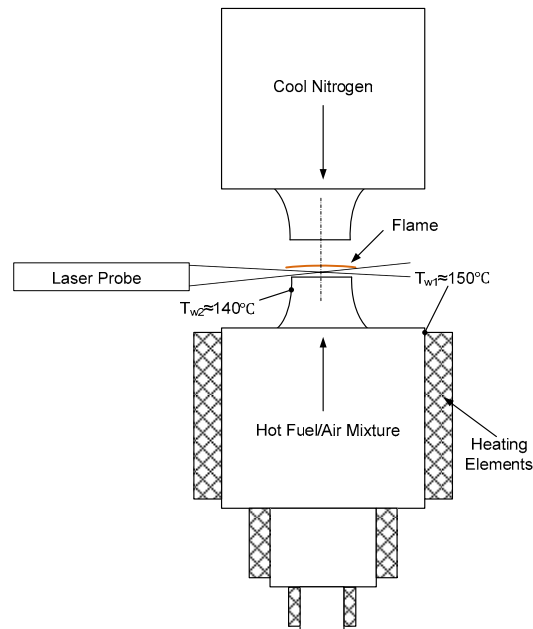
Figure 9.—Burner configuration.
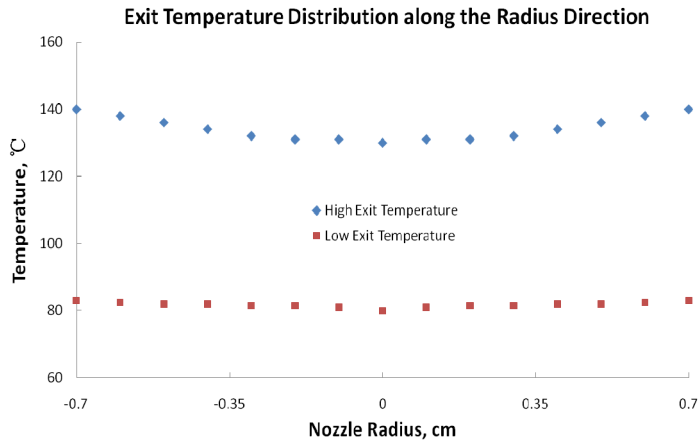
Figure 10.—Radial temperature distribution at the nozzle exit.
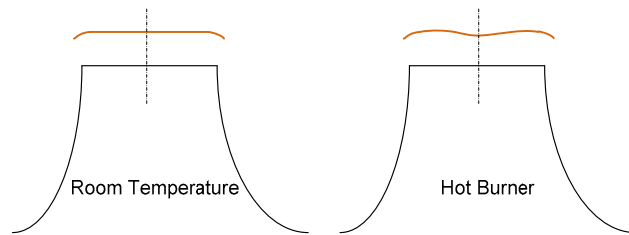
Figure 11.—Flame shape at different exit temperatures.

3.2.5   Effect of Flow Rate on Burner Exit Temperature

By plotting the reference flame speed, $S_{u,\mathrm{ref}}$, against the strain rate, K, the laminar flame speed, S_u^o, could be determined by extrapolating the reference flame speed to zero stretch as indicated in Figure 12. K is varied by changing the flow rate through the burner using a bypass system. However, along with the change of flow rate, the heat-transfer rate between the mixture and the wall also changes, thus affecting the gas exit temperature. Figure 13 depicts the exit temperature variation with K. As expected, results indicate that if the flow rate decreases by opening the bypass, the gas exit temperature increases. The typical effect of the unburned gas temperature on laminar flame speed is shown in Figure 14. Consequently, if a temperature correction is not applied to the raw data, the extrapolation would yield incorrect laminar flame speeds at elevated temperatures.

Figure 15 shows the reference flame-speed variation for stoichiometric toluene/air mixtures at different exit temperatures with no temperature correction. As observed, the slope of the raw data is positive at room temperature. However, if the exit temperature is increased to 80 °C, the slope becomes flatter and finally becomes negative when the temperature reaches 130 °C. From the theory of stretched flames, it is known that the slope of the raw data should be sensitive only to the mixture Lewis number, such that the unburned mixture temperature should not change the slope of the data. Figure 16 shows the raw data from Figure 15 corrected using the results from Figure 13. Here, as expected, the slope of the raw data at different exit temperatures remains the same.
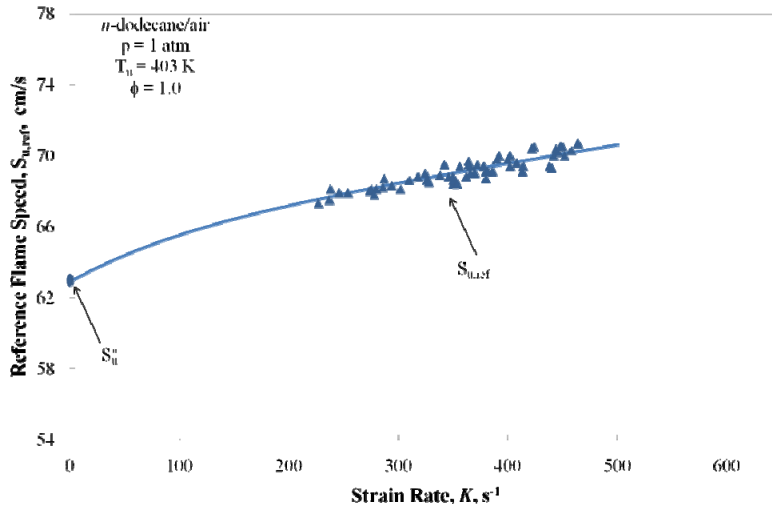
Figure 12.—Laminar flame speed determination.
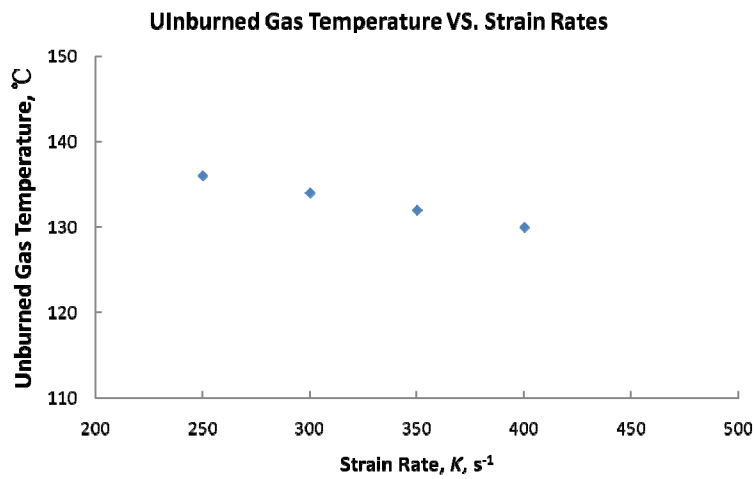
Figure 13.—Variation of exit temperature versus strain rate.
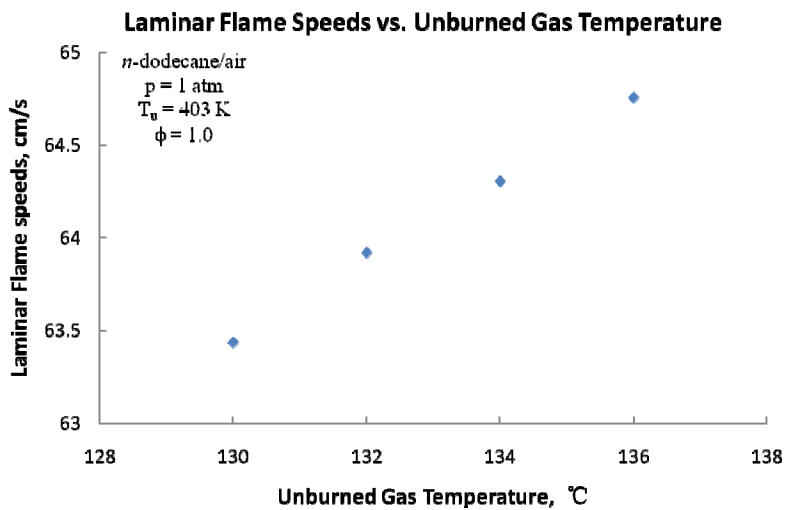
Figure 14.—Variation of laminar flame speed with unburned gas temperature.

Reference Flame Speeds vs. Strain Rates without Temperature Correction
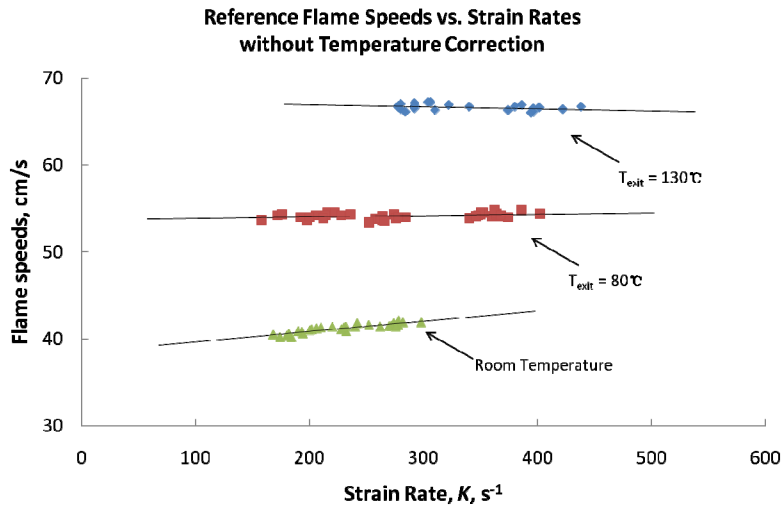
Figure 15.—Variation of the reference flame speed with strain rate with no temperature correction.

Reference Flame Speeds vs. Strain Rates with Temperature Correction
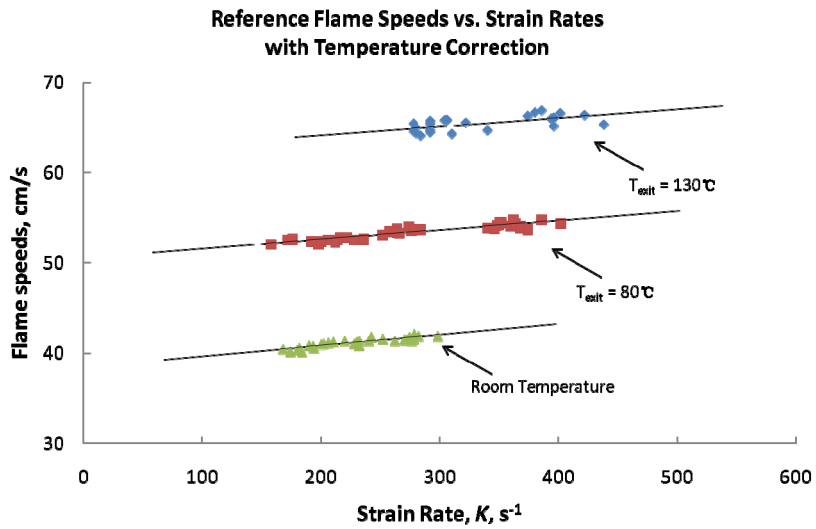
Figure 16.—Variation of the reference flame speed versus strain rate with temperature correction, showing the expected independence of slope versus strain rate with initial temperature.

3.2.6 Effect of Radial Location on Reference Flame Speeds in the Counterflow Configuration

Next, USC looked at the effect of radial location on the exit velocity components, reference flame speeds and stretch rates. Figure 17 depicts the variation along the radial distance from the centerline, r, of the radial velocity component, v, and the axial velocity component, u, near the nozzle exit, for a stoichiometric methane/air flame at room temperature. The variation of v along r is linear, as is expected for the counterflow configuration. However, away from the centerline, the u profile starts deviating away from that of a plug flow. Figure 18 indicates that the measured $S_{u,\mathrm{ref}}$ and K also increase away from the centerline. The deviation of the above values is significant for $r > 1$ mm.

Similar results are shown in Figures 19 and 20, for the case of a stoichiometric methane/air flame at an unburned mixture temperature of 130 °C. The deviation of $S_{u,\mathrm{ref}}$ and K is even more severe in this case due to the higher flame speeds and the thermal boundary layer discussed earlier.

The increase of $S_{u,\mathrm{ref}}$ away from the centerline cannot be attributed solely to the increase in stretch rate due to the axial velocity gradient. Two-dimensional and curvature effects play a much more significant role in the deviation of measurements away from the centerline. Therefore, from the investigations above, we conclude the absolute necessity of taking the reference flame speed and axial strain rate measurements very close to the nozzle centerline. Thus, discrepancies frequently observed with data obtained from other research groups using the counterflow configuration could be attributed to such effects.
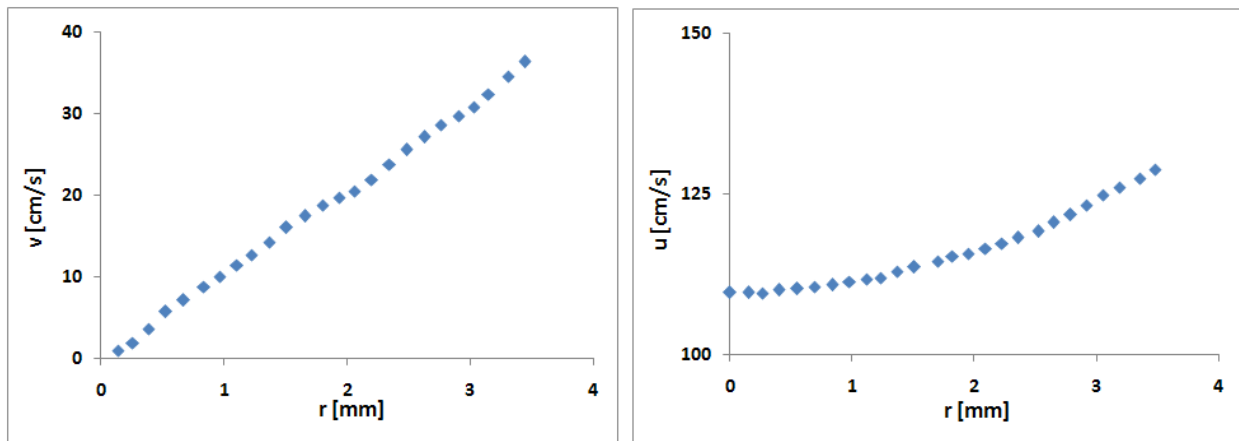
Figure 17.—Radial variation of the radial and axial exit velocity components of counterflow jet at room temperature.
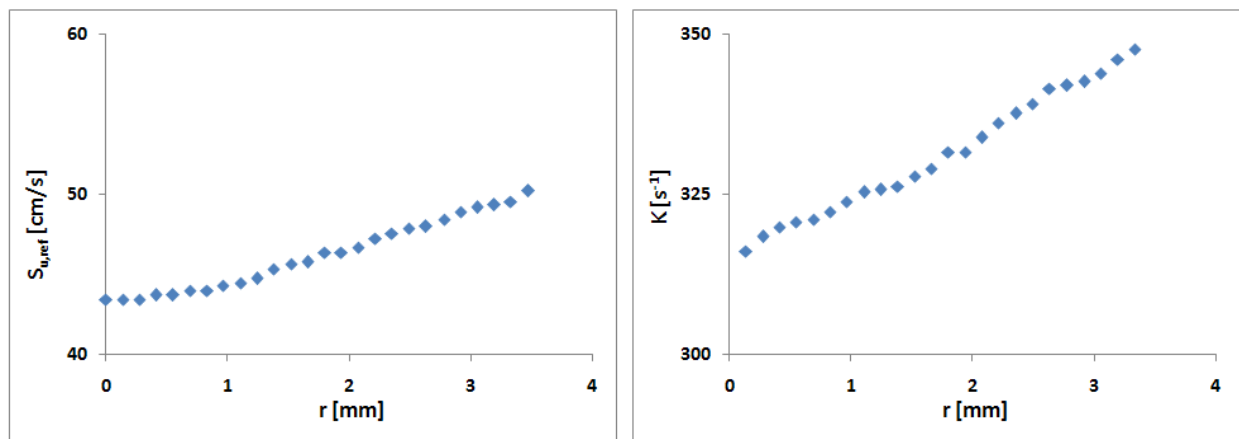
Figure 18.—Radial variation of the reference flame speed and stretch rate for flames at room temperature.
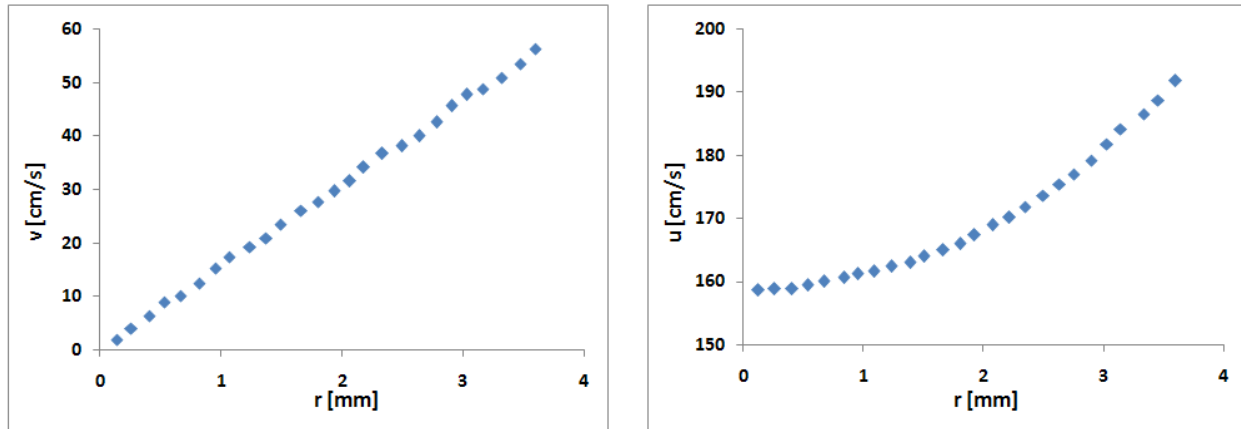
Figure 19.—Radial variation of the radial and axial exit velocity components of counterflow jet at elevated temperature.
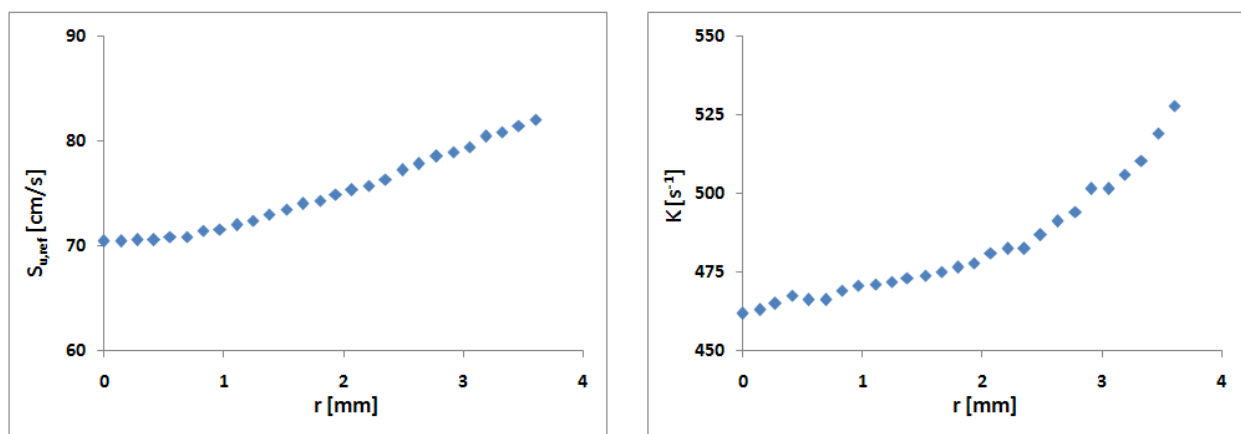
Figure 20.—Radial variation of the reference flame speed and stretch rate for flame at elevated temperature.

A more thorough explanation of some of the observed phenomena can be provided. Figure 21 again depicts the variation along the radial distance from the centerline, r, of the radial velocity component, v, and the axial velocity component, u, near the nozzle exit, for a stoichiometric methane/air flame at room temperature. The variation of v along r is linear, as expected for the counterflow configuration. However, the u profile starts deviating away from that of the plug flow away from the centerline. Figure 22 depicts the flame shape defined by the axial location of the measured reference flame speed. It is noticed that the measured reference flame speed, $S_{u,\mathrm{ref}}$, increases significantly away from the centerline.

After extensive analysis, it was realized that the slight curvature of the counterflow flame away from the centerline has a significant effect on the measurements, since the reference flame speed measured in the vertical direction actually is not the true reference flame speed normal to the flame surface. If the total velocity at the location of measured reference flame speed is projected onto the normal of the flame surface, the corrected and true reference flame speed is obtained. As expected, the profile of the true reference flame speed does remain flat in the radial direction. Again, we conclude from the investigations above the absolute necessity of taking the reference flame speed and axial strain rate measurements very close to the nozzle centerline. Otherwise, the reference flame speed measured would not be the true value normal to the flame surface.
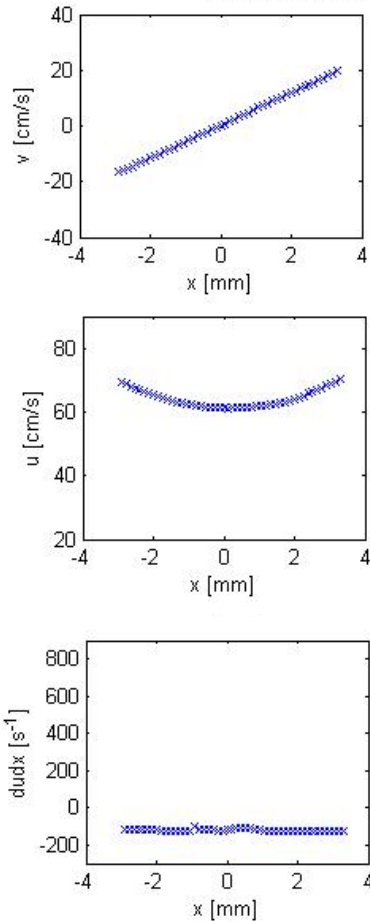
Figure 21.—Radial variation of the radial and axial exit velocity components of a counterflow jet.
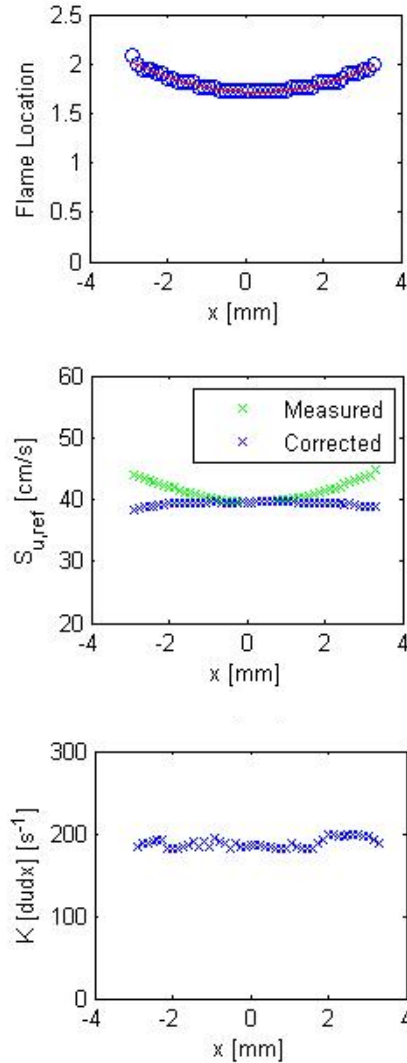
Figure 22.—Flame shape and radial variation of the reference flame speed and stretch rate for a counterflow flame.

3.2.7   Development of a Laser Extinction System for Measuring Soot Volume Fractions

In preparation for measurements of sooting characteristics in flames, USC upgraded their experimental capabilities with the addition of a system for high-resolution laser extinction measurements of soot volume concentration. Soot, a cluster of carbon atoms larger than the surrounding fuel, air, and N_2, absorbs light. By transmitting a laser through a sooting flame, the amount of light absorbed can be calculated and, through an established process, be reversed to find the soot volume fraction.

The system consists of a 1-mW helium-neon laser mounted on a precision y-z traverse. The laser beam can be focused to a minimum thickness of 0.1 mm with a 20-cm plano-convex lens and mounted so as to traverse the flames between our burners in the horizontal plane. Laser-beam intensity is recorded by a ThorLabs PDA 100A amplified photo-detector. This photo-detector has a sensitive diameter of approximately 6 to 8 mm. The traverse mechanism is manually operated and allows for better than 10-μm stepping resolution. Due to the large detection area of the photo-detector the system can be configured to permit the detector to remain stationary while only the laser is moved; this greatly simplifies the implementation of this technique on more complex apparatuses and limits its susceptibility

to vibrations. Photo-detector output is recorded by both a Fluke Digital Multimeter averaged over a period of 20 sec for each position and a Tektronix 3630 oscilloscope. The reference readings (I_0) are performed without a flame or with a non-sooting flame and then readings with a sooting flame (I) are taken to yield the line of sight transmittance (I/I_0). Following Wang, Du, Sung, and Law (Ref. 4), the local extinction coefficient k_{ext} is obtained through deconvolution of the integral:

$$-\ln\left(\frac{I(y)}{I_0}\right) = \int_y^\infty k_{ext}(r)\frac{r}{\sqrt{r^2 - y^2}}dr .$$

The soot volume fraction (F_v) is then obtained from the relationship,

$$k_{ext} = \frac{6\pi}{\lambda}\text{Im}\left[\frac{m^2-1}{m^2+2}\right]F_v,$$

where λ is the wavelength of the laser beam—632.8 nm—and m is the complex refractive index, $m = 1.58$ to $0.57i$. Figure 23 shows a schematic of the set-up and Figure 24 shows a photo of the experimental setup.

The apparatus was tested using an ethylene-N_2 mixture with a 0.297 fuel mole fraction and a 0.339 fuel mole fraction. One data set for the 0.297 fuel mole fraction (Flame A), and one for the 0.339 fuel mole fraction (Flame B), are plotted as line of sight transmittance (I/I_0) versus distance from the bottom burner in Figure 25. Flames A and B start sooting and stop sooting in roughly the same location from the exit of the bottom burner, but show significant difference across the flame. The reported data in Figure 25 are very preliminary (with large uncertainty bars) and are meant just to demonstrate that the system output is what is expected qualitatively. During the testing it was found that it is necessary to allow the laser and photo-detector to warm up for at least 30 min to ensure stable reference readings.

As seen in Figure 25, there is significant scatter in the data and attendant uncertainty bars. This is likely associated with unsteadiness of the flame related to air currents and burner alignment. Repeatability and reliability of the data will have to be assured before any definitive data is produced, but the system has been shown to function correctly and has sufficient sensitivity to be of great use in measuring liquid fuels once it is properly configured. An enclosure will need to be built to accommodate the sooting flames, for health purposes, an N_2 environment for eliminating the secondary diffusion flames caused by reaction with the ambient air is needed, and the flame must be shielded from air currents associated with manually adjusting the traverse mechanism. Adding pure O_2 to the top flow will increase the temperature and provide a larger range of soot-producing flames. A special thermocouple will also need to be incorporated, which will sample the temperature of the flame allowing it to be regulated or held constant.
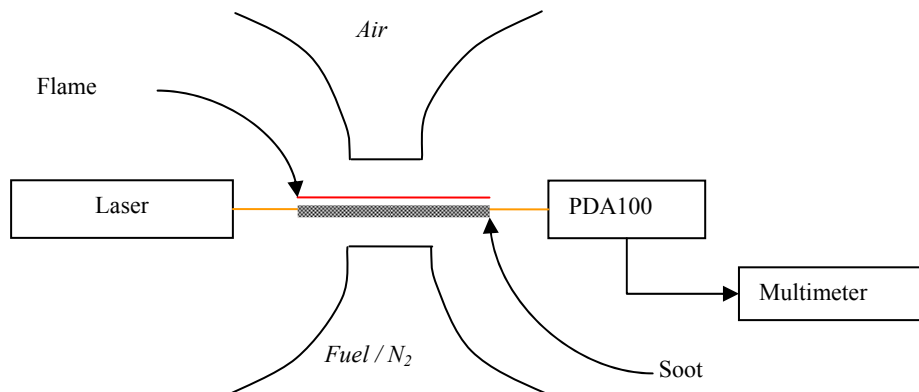
Figure 23.—Schematic of a non-premixed sooting flame set-up with laser light extinction.
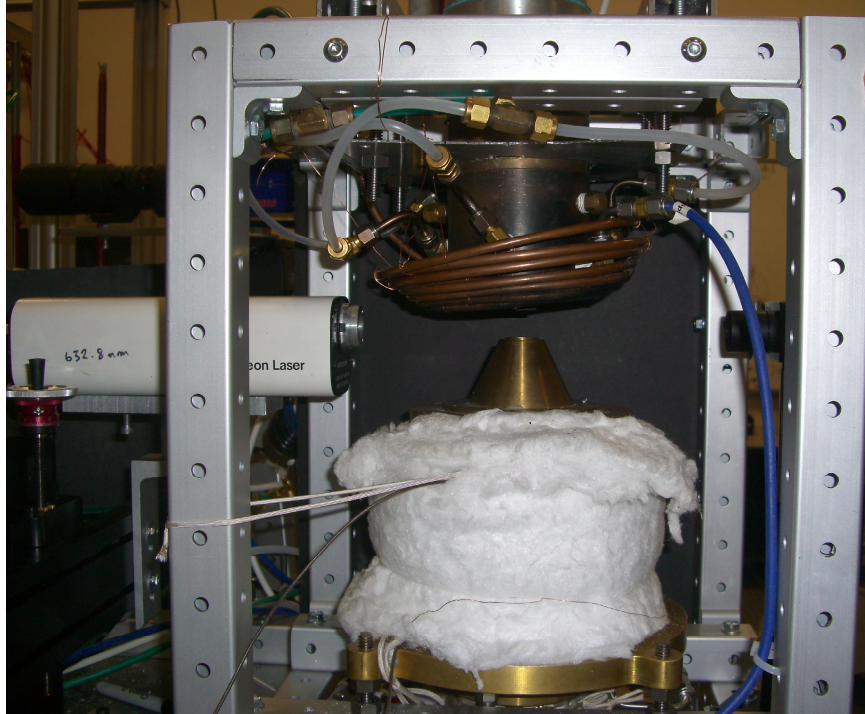
Figure 24.—Photograph of a non-premixed sooting flame set-up with a laser light extinction.
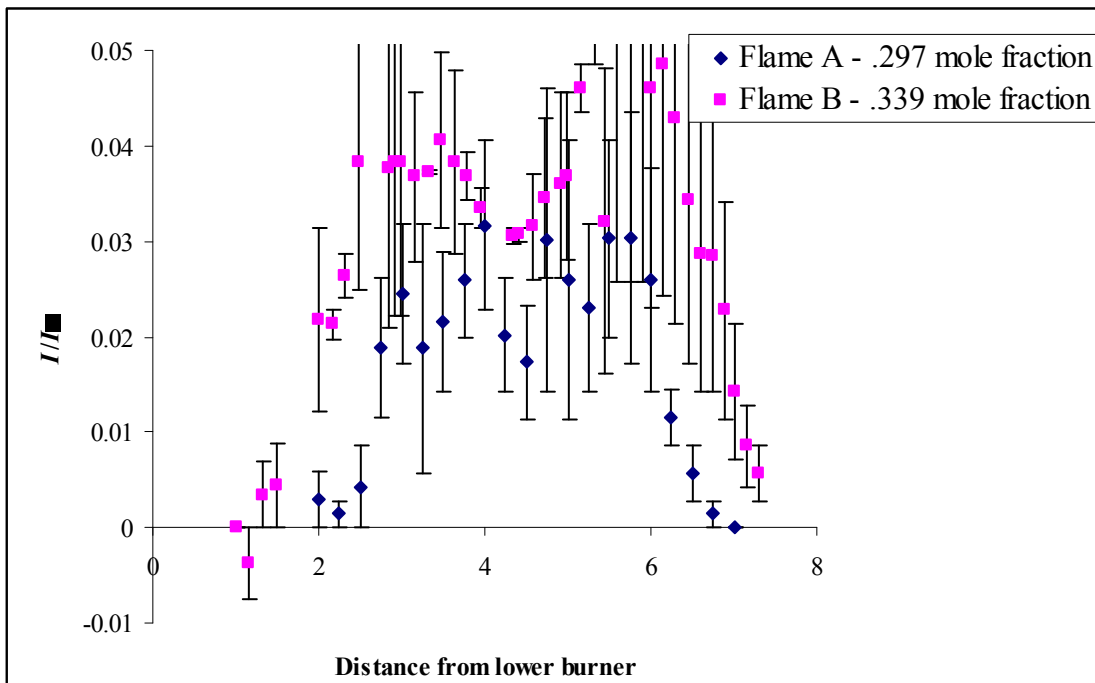
Figure 25.—Line of transmittance fraction (I/I_0) versus distance from bottom burner.

3.2.8 Development of a Counterflow Ignition Burner Rig

A new rig was also developed to study flame ignition that is achieved by heating air or N_2 in one of the two burners at temperatures well exceeding 1000 K. To achieve this, one burner is replaced by a quartz tube equipped with independently controlled helicoidal internal (SiC) and external (Kanthal AI) electric heating elements that are capable of raising the temperature of the air jet up to 1600 K; this is similar to the approach of Fotache et al. (Ref. 5). A temperature controller/power supply is used to operate the internal heater. Feedback to the temperature controller is provided by a B-type thermocouple (Pt-6% Rh/Pt-30% Rh) positioned in the hot air stream within the quartz tube close to the surface of the inner heater. For a given reactant configuration and reactant composition, the temperature at the quartz tube exit is increased and monitored via another B-type thermocouple, until flame ignition occurs, at which point the tube exit temperature is defined as the ignition temperature, T_{ign}. The ignition system is shown in Figure 26.

3.2.9 Results From Laminar Flame-Speed and Extinction Strain-Rate Measurements

The upgraded vaporization system described in the previous section had a massive impact on the accuracy and repeatability of the experiments, since the flames are noticeably more stable due to the fuel vaporization being much more constant. Hence, new and more accurate sets of laminar flame speeds were measured towards the end of the project for mixtures of S-8, R-8, n-$C_{12}H_{26}$, JP-7, and JP-8 with air at an unburned mixture temperature $T_u = 403$ K. All results are shown graphically in Figure 27 and numerically in Table 3 as a function of fuel/air mass ratio.
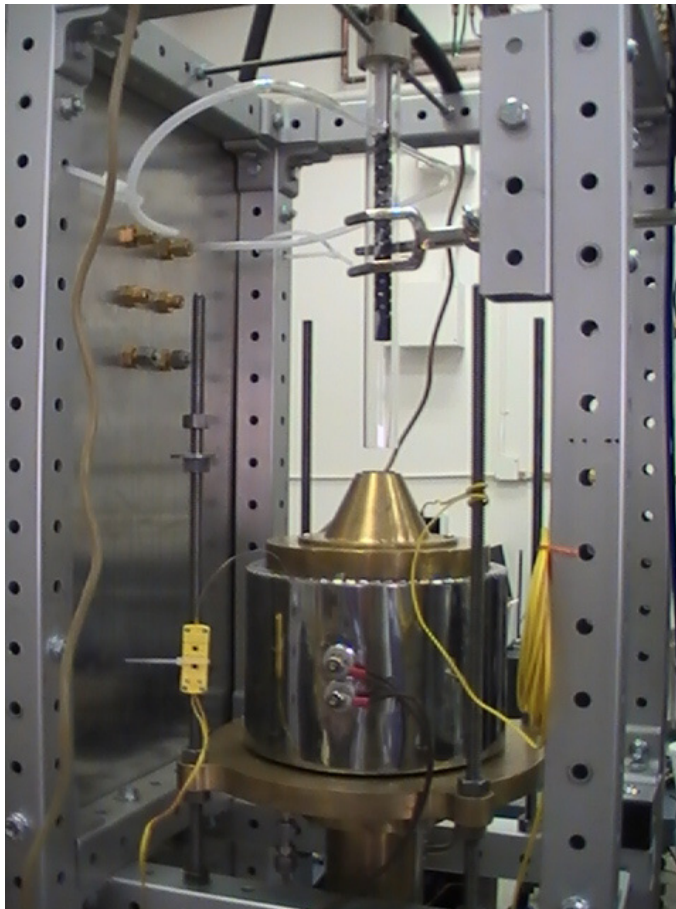
Figure 26.—Photograph of ignition counterflow burner setup.
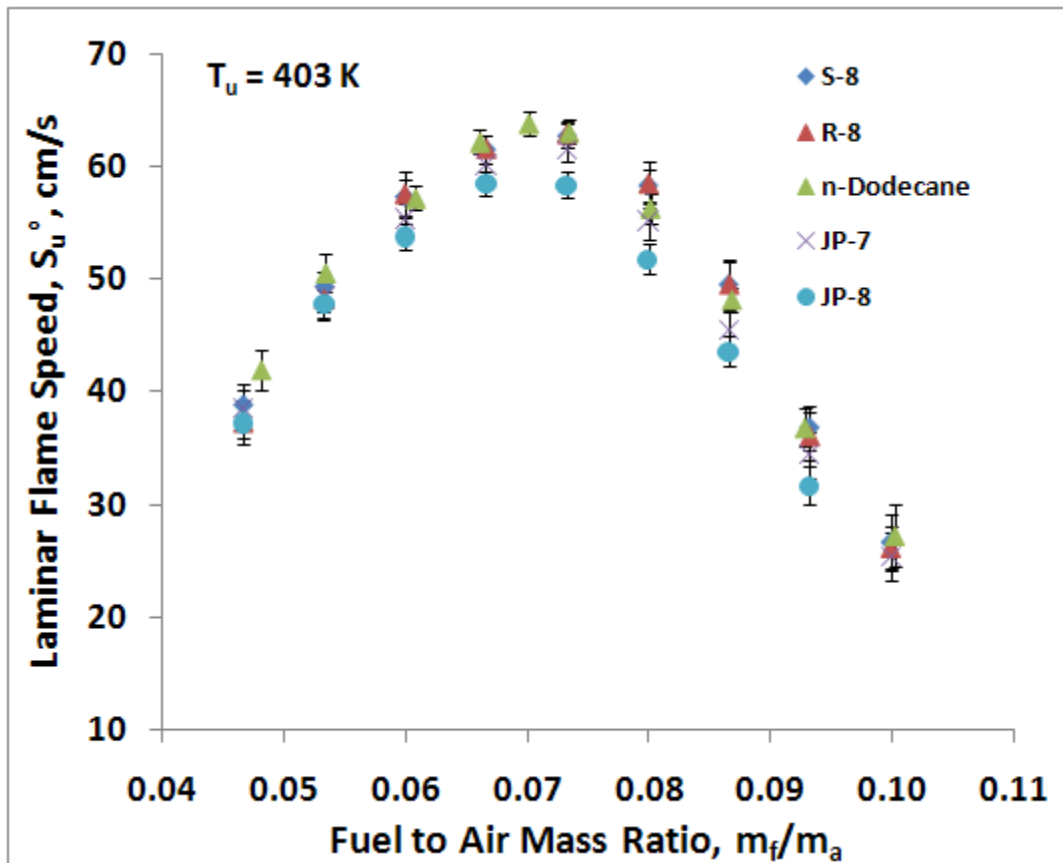
Figure 27.—Experimentally determined laminar flame speeds, S_u°'s, of mixtures of S-8, R-8, n-$C_{12}H_{26}$, JP-7 and JP-8 with air as a function of fuel to air mass ratio.

TABLE 3.—EXPERIMENTALLY DETERMINED LAMINAR FLAME SPEEDS, S_u°'s, OF MIXTURES
OF S-8, R-8, N-$C_{12}H_{26}$, JP-7 AND JP-8 WITH AIR AS A FUNCTION OF FUEL TO AIR MASS RATIO

S-8		R-8		n-$C_{12}H_{26}$		JP-7		JP-8	
m_F/m_A	S_u° [cm/s]	m_F/m_A	S_u° [cm/s]	m_F/m_A	S_u° [cm/s]	m_F/m_A	S_u° [cm/s]	m_F/m_A	S_u° [cm/s]
0.0466	38.8	0.0466	37.3	0.0481	42.0	0.0466	38.5	0.0466	37.3
0.0533	49.3	0.0533	48.2	0.0534	50.6	0.0533	48.4	0.0533	47.8
0.0599	57.3	0.0599	57.5	0.0608	57.2	0.0599	55.3	0.0599	53.8
0.0666	61.5	0.0666	61.5	0.0661	62.2	0.0666	60.1	0.0666	58.5
0.0732	62.7	0.0732	62.8	0.0701	63.8	0.0732	61.4	0.0732	58.4
0.0799	58.3	0.0799	58.4	0.0734	63.1	0.0799	55.1	0.0799	51.8
0.0865	49.5	0.0866	49.5	0.0801	56.3	0.0865	45.4	0.0866	43.6
0.0932	36.8	0.0932	36.1	0.0868	48.2	0.0932	34.4	0.0932	31.7
0.0999	26.6	0.0998	26.2	0.0928	36.8	0.0999	25.4	--------	--------
--------	--------	--------	--------	0.1002	27.2	--------	--------	--------	--------

The propagation rates of S-8/air and R-8/air flames are almost identical. Compared to n-$C_{12}H_{26}$/air, the S-8/air and R-8/air laminar flame speeds are 1 to 2 cm/s lower on average. The S-8/air and R-8/air flames propagate at approximately the same rate as JP-7/air flames, while they are 2 to 4 cm/s faster than JP-8/air flames.

The extinction strain rates of mixtures of S-8, R-8, n-$C_{12}H_{26}$, JP-7, and JP-8 with air are shown graphically in Figure 28 and numerically in Table 4 for an unburned mixture temperature $T_u = 403$ K. Due to Reynolds number constraints, i.e., for the counterflowing jets to remain laminar, 7-mm nozzles with a separation distance of 10 mm are used for higher extinction strain rates, i.e., for fuel-to-air mass ratios, F/A > 0.6, while 14-mm nozzles with a separation distance of 14 mm for F/A < 0.6 are used. Further experiments using 7-mm nozzles will be conducted soon to cover the entire range within the flammability limits for S-8/air and R-8/air flames. It can be seen that the S-8/air and R-8/air flames exhibit identical extinction characteristics. Compared to n-$C_{12}H_{26}$/air flames, they exhibit slightly lower resistance to extinction.
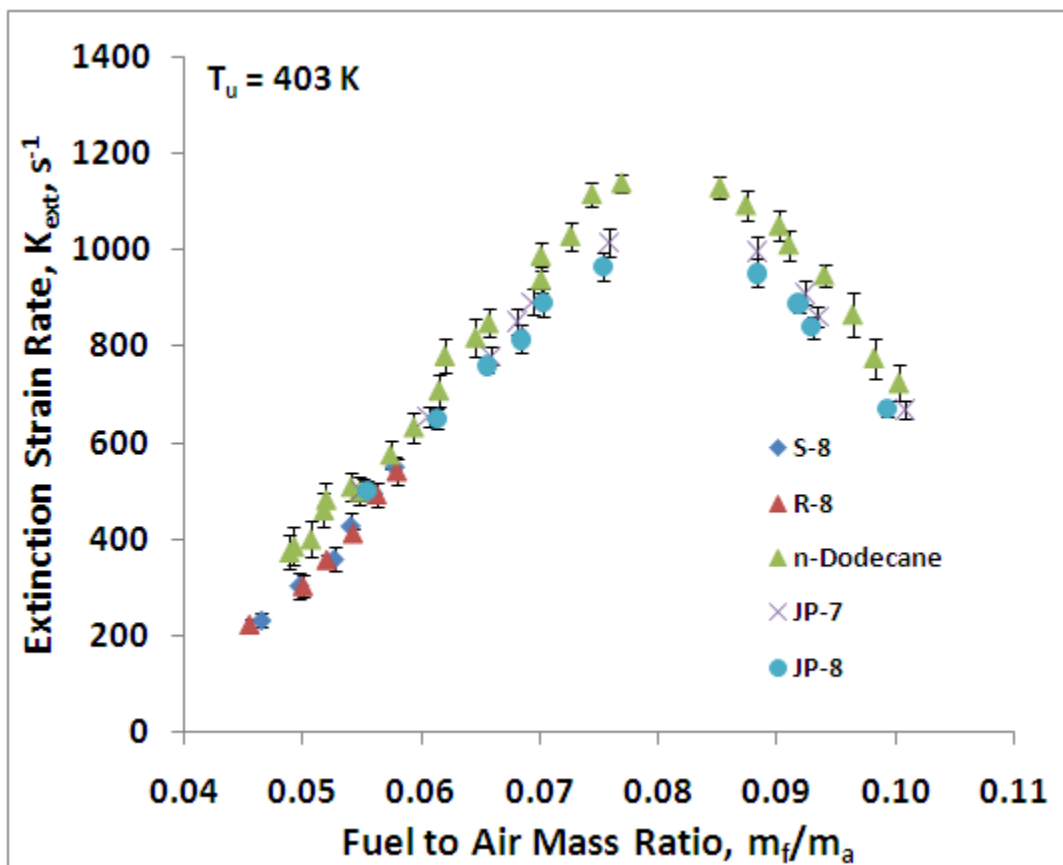
Figure 28.—Experimentally determined extinction strain rates, K_{ext}'s, of mixtures of S-8, R-8, n-$C_{12}H_{26}$, JP-7 and JP-8 with air, as a function of fuel-to-air mass ratio.

TABLE 4.—EXPERIMENTALLY DETERMINED EXTINCTION STRAIN RATES, K_{ext}'s, OF MIXTURES OF S-8, R-8, N-C$_{12}$H$_{26}$, JP-7 AND JP-8 WITH AIR AS A FUNCTION OF FUEL-TO-AIR MASS RATIO

S-8		R-8		n-C$_{12}$H$_{26}$		JP-7		JP-8	
m_F/m_A	K_{ext} [s^{-1}]	m_F/m_A	K_{ext} [s^{-1}]	m_F/m_A	K_{ext} [s^{-1}]	m_F/m_A	K_{ext} [s^{-1}]	m_F/m_A	K_{ext} [s^{-1}]
0.0466	232	0.0456	222	0.0491	373	0.0550	503	0.0555	500
0.0498	304	0.0501	302	0.0510	400	0.0607	655	0.0614	650
0.0527	359	0.0521	356	0.0550	499	0.0681	852	0.0684	814
0.0541	428	0.0543	411	0.0577	575	0.0934	862	0.0930	840
0.0560	496	0.0563	492	0.0618	708	0.1008	670	0.0993	670
0.0578	563	0.0580	540	0.0496	385	0.0694	892	0.0703	892
				0.0520	461	0.0759	1015	0.0754	965
				0.0523	483	0.0883	997	0.0883	951
				0.0543	509	0.0660	781	0.0656	760
				0.0596	632	0.0924	910	0.0918	889
				0.0967	776				
				0.0988	724				
				0.1019	693				
				0.0623	780				
				0.0649	818				
				0.0660	848				
				0.0949	835				
				0.0742	1065				
				0.0882	1042				
				0.0699	888				
				0.0937	897				
				0.0725	978				
				0.0911	1000				
				0.0699	937				
				0.0913	960				
				0.0767	1088				
				0.0853	1079				

3.2.10 Results From NO$_x$ Measurements

Experiments were carried out with jet fuel surrogate candidates, *n*-decane and *n*-dodecane, at an unburned mixture temperature, T_u = 403 K, and different equivalence ratios. The NO$_x$ concentration profiles for *n*-decane/air and *n*-dodecane/air flames at equivalence ratios of 0.8, 1, and 1.2 are shown in Figures 29 to 31, respectively. It can be seen that the *n*-decane/air and *n*-dodecane/air flames produce approximately the same amounts of NO$_x$ on the lean side, the stoichiometric point and the rich side.
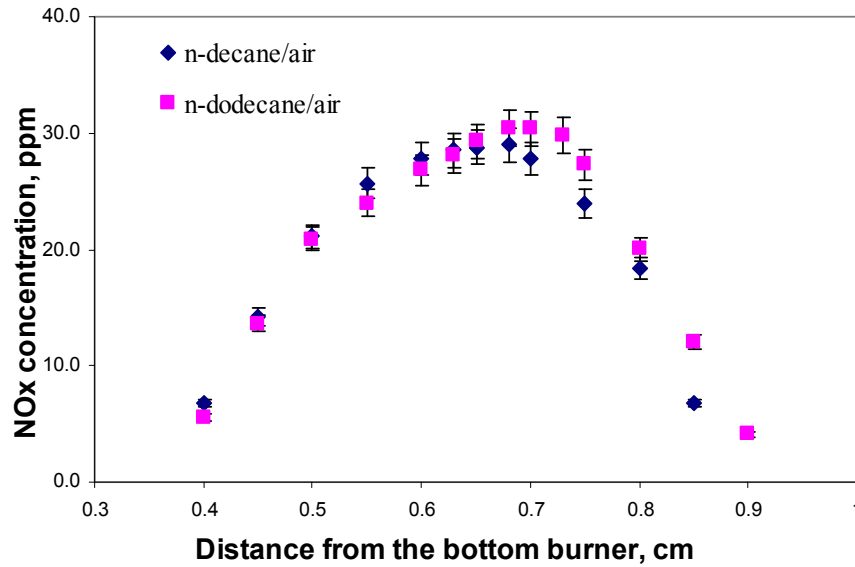
Figure 29.—Experimentally determined NO$_x$ concentration profiles as
a function of distance from the bottom burner for *n*-decane/air and
n-dodecane/air flames (equivalence ratio = 0.8, K = 166 s^{-1}; T_u = 403 K).
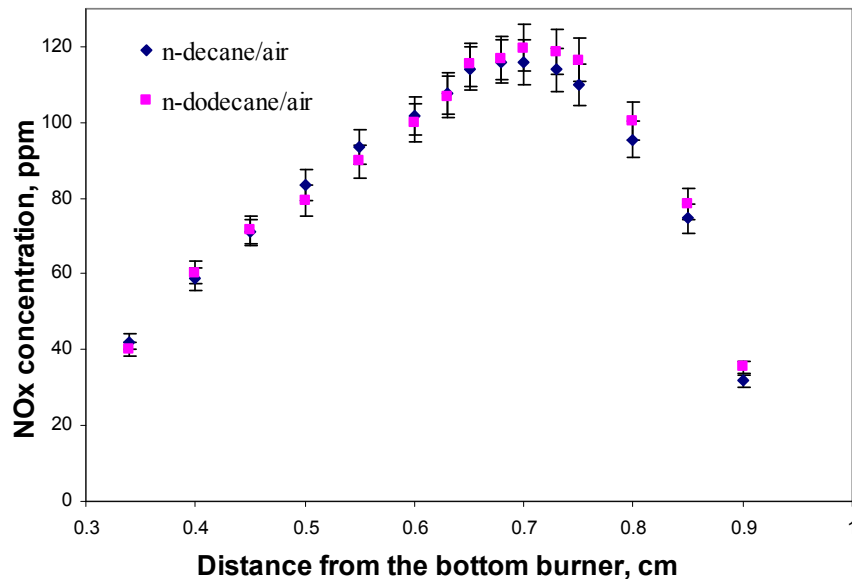
Figure 30.—Experimentally determined NO$_x$ concentration profiles as
a function of distance from the bottom burner for *n*-decane/air and
n-dodecane/air flames (equivalence ratio = 1.0, K = 166 s^{-1}; T_u = 403 K).
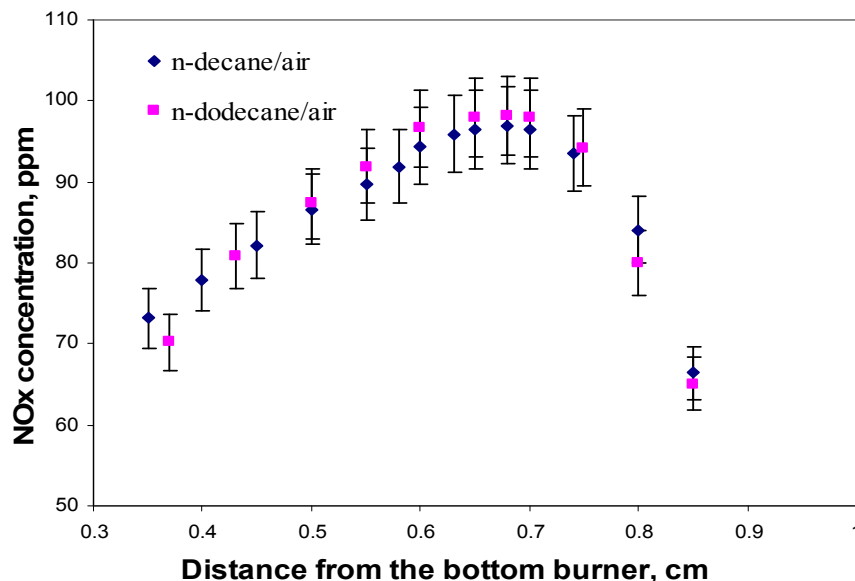
Figure 31.—Experimentally determined NO_x concentration profiles as a function of distance from the bottom burner for *n*-decane/air and *n*-dodecane/air flames (equivalence ratio = 1.2, K = 166 s^{-1}; T_u = 403 K).

3.3   Kinetic Model Development and Reduction

During this project, Reaction Design, in collaboration with Dr. Westbrook, has assembled, tested and improved a detailed surrogate mechanism for F-T fuels. Identification of an appropriate surrogate blend was based on chemical analysis data obtained by USC through their collaboration with the AFRL. These mechanisms were tested against flame data obtained at USC as well as data obtained from external sources, as described in the following section of this report. The validated mechanism has also been reduced successfully to a size that is reasonable for use in CFD simulations for jet-engine combustor design applications. Here we describe the details of the surrogate-blend determination, the mechanism development, and the mechanism reduction activities.

3.3.1   Identification of Appropriate Surrogate Blends for F-T Fuels

The results of the detailed qualitative analysis for the F-T fuel provided by the Air Force Research Laboratory, labeled S-8, are provided in the section titled (F-T) fuels.

It was found that the dominant components consisted mainly of *n*-and *iso*-paraffins of C_8 to C_{15} chains. As seen in Figure 32, *iso*-paraffins are the major components in the F-T fuel with over 70 mol% of the total composition, whereas the rest are *n*-paraffins. Although high in *iso*-paraffins, these are much less branched compared to gasoline or diesel. Most of the *iso*-paraffins in the F-T fuel consist of only one methyl branch (- CH_3) on a long- and straight-chain alkane. Based on the carbon number distribution shown in Figure 33, more than half of the alkanes have a C_{10} to C_{12} chain. Such long-chain alkanes will make the effect of the small branched methyl group less significant.

We therefore first proposed a binary surrogate mixture containing *n*-dodecane and *n*-decane, as shown in Table 5. Here, *n*-dodecane represents the *n*-alkane class and *n*-decane represents the *iso*-alkane class in the overall analysis. As discussed, *iso*-alkanes in the F-T fuels contain only one methyl branch on a long straight-chain alkane, so that it is reasonable to use *n*-decane as a representative of the *iso*-alkane class. However, a more complex surrogate could be used in the future (pending availability of mechanisms for low-branched *iso*-alkanes), as suggested in Table 5.

F-T fuel (S-8) overall analysis, mol%

- iso-alkane
- n-alkane
- cyclo-alkane
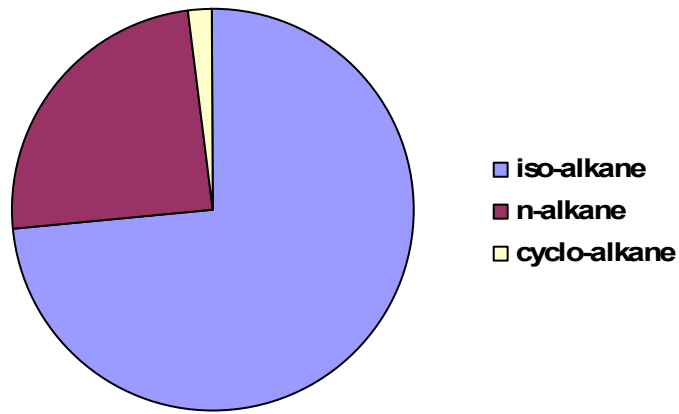
Figure 32.—Hydrocarbon class analysis of the F-T fuel.
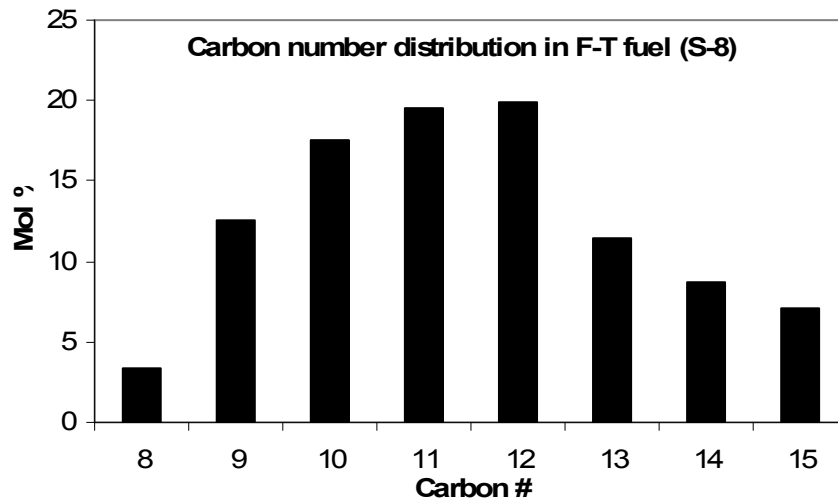
Figure 33.—Carbon number distribution in the F-T fuel.

TABLE 5.—INITIAL SURROGATE MIXTURES PROPOSED FOR THE F-T FUEL (S-8)

Component	Current, mol%	Possible alternative for future, mol%
n-dodecane	24	15
n-decane	76	10
4-methyloctane	--	38
2-methyldodecane	--	37

To better account for the branched alkanes in the F-T fuel analysis, we later recommended and assembled a 3-component surrogate mixture that included *iso*-alkane. This was due to the inability of the binary mixture of *n*-decane and *n*-dodecane to match measured cetane numbers for F-T fuels. Cetane number can be an important property to match for a fuel surrogate, as it represents the ignition behavior of the fuel. The F-T fuel samples that we received from AFRL have cetane numbers of approximately 60, as shown in Table 6. Since *n*-decane and *n*-dodecane have cetane numbers of 76 and 80, respectively, it is not possible to achieve a lower cetane number with their blends. *Iso*-alkanes, even with very small side chains, decrease the cetane number of F-T fuels. Therefore, we have added *iso*-octane as a third component for our F-T surrogate blend. This allows us to (1) represent the *iso*-alkane class, (2) match cetane number criteria by supplying a component with a very low cetane number of 14, and (3) include a component with a smaller carbon number that will facilitate matching the lower boiling point range of the real F-T fuel. In addition, having *iso*-octane as a surrogate component should improve NO_x emissions predictions for the surrogate model. We chose *iso*-octane due to its suitability for these purposes the availability of a well validated mechanism that was reasonably consistent with our *n*-alkane base mechanisms. Compared to the *iso*-alkanes with only one or two methyl side chains found in F-T fuels, *iso*-octane is a highly branched component. So the amount required in the blend to match the cetane number is much less than the fraction of total *iso*-alkanes in F-T fuels. Based on fuel analysis data on carbon number distribution (Fig. 1) and cetane number data (Table 6), we proposed two different surrogates as shown in Table 7. These surrogates not only match cetane numbers but also reflect the carbon number distribution in the F-T fuels. It is possible to add more components to the surrogate, especially for S-8, which has higher carbon-number alkanes, but for this work and the focus on flame simulations, we limited the number of components to three.

TABLE 6.—CETANE NUMBER OF TWO
F-T FUEL SAMPLES USING
DIFFERENT METHODS

Cetane no.	IQT	ASTM D976
Shell GTL	59.67	68
Syntroleum S-8	59.08	57

TABLE 7.—3-COMPONENT SURROGATE MIXTURES PROPOSED FOR TWO F-T FUELS

Model fuel component	Surrogate for Shell GTL, mol%	Surrogate for Syntroleum S-8, mol%	Cetane no.
n-dodecane	10	38	80
n-decane	65	34	76
iso-octane	25	28	14
Cetane number	60.9	60.2	--
H/C molar ratio	2.21	2.20	--

To optimize the match of the surrogate blend to targeted fuel properties, we have developed (under separate funding) a software tool called the Surrogate Blend Optimizer (SBO). The SBO software performs global and local optimization methods to determine the best surrogate blend, based on matching user-defined targets, which may include any combination of:

1. Chemical class composition
2. Ignition quality (octane and cetane numbers)
3. H/C ratio
4. Lower heating value (LHV)
5. Several points from the true boiling point curve (ASTM D-2892 method)

For calculating blend properties, we employed a linear-blending method for ignition quality and LHV. Such properties for neat fuel components are provided by reference as tagged input in the thermodynamic data portion of our reaction mechanisms that were used in CHEMKIN-PRO (Ref. 1) simulations. The SBO employs two different minimization algorithms: a genetic algorithm for searching for a global minimum, and then a directional-set algorithm for accurately finding the local minimum. Once a user selects the fuel components to be included in the blend and provides one or more targets to be achieved by the blend, the SBO will find an optimum blend that best satisfies all the targets. A weighting factor may also be used to give some targets more weight than others.

We used the SBO to obtain optimum 3-component blends for Shell GTL and for the Syntroleum S-8 fuels. The targets used for these two F-T fuels are shown in Table 8. The first four targets represent measured properties obtained for the real F-T fuels. The additional criteria on the range of boiling points have been specified to try to match the trends in boiling curve of the real F-T fuel while only considering a 3-component surrogate blend. Also, we have added additional constraints on *iso*-octane since this is a highly branched molecule compared to the *iso*-alkanes found in F-T fuels. An additional constraint is also placed on the *n*-dodecane mole fraction, which is especially important for the Shell GTL surrogate, since it has a very small number of components that are heavier than a C_{12} hydrocarbon. Based on these criteria, the SBO found different surrogate blends for the two F-T fuels, as shown in Table 9. The original blend in Table 7 was determined manually before we had completed work on the SBO software. We can see that both blends found by the SBO are close to those originally proposed in Table 7. In future, however, we will be able to use the SBO method for more complex surrogate blends and to match a wider range of properties of the real fuel.

TABLE 8.—CRITERIA USED IN SURROGATE BLEND OPTIMIZER
SOFTWARE TOOL FOR TWO F-T SURROGATES

Target/Criteria	Shell GTL	S-8
Cetane no.[a]	61	60
H/C molar ratio[a]	2.17	2.17
Lower heating value, MJ/kg[a]	44.14	44.14
T50 boiling point, K[a]	445	474
Additional criteria used to achieve better blend based on fuel analysis with limited number of components in the blend:		
T20 boiling point, K	433	449
T90 boiling point, K	456	522
iso-Octane, mol fraction	0.25	0.25
n-Dodecane, mol fraction	0.1	0.33

[a]Measured property of F-T fuels.

TABLE 9.—OPTIMUM COMPOSITION FOUND BY SURROGATE
BLEND OPTIMIZER FOR TWO F-T SURROGATES

Property	Shell GTL	S-8
iso-Octane, mol%	28	32
n-Decane, mol%	61	25
n-Dodecane, mol%	11	42
Cetane no.	61	61
H/C molar ratio	2.21	2.20
Lower heating value, MJ/kg	44.55	44.45
T50 boiling point, K	404	447

While we were not able to obtain detailed chemical analysis for bio-derived jet fuel from UOP or for the R-8 fuel discussed in the previous section, we believe it is very likely to have no aromatics, and we expect it to have mainly linear and branched paraffins. Thus, their composition is expected to be very similar to that of F-T fuel due to removal of oxygen from the ester molecules during the hydrogenation process for jet-engine application. For this reason, we expect the same 3-component blends discussed above will be applicable for bio-jet fuels as well. We would be able to match specific fuel-property targets for bio-jet fuel using the SBO method, but the component fuels should be the same.

3.3.2   Baseline *n*-Alkane Mechanism up to C_{12}

A detailed reaction mechanism has been developed for the proposed alternative jet-fuel surrogates. The surrogate components include *n*-dodecane, *n*-decane, *n*-heptane, and *iso*-octane. We started with the recent Westbrook et al. (Ref. 6) mechanism for *n*-alkanes that contains all linear alkanes from *n*-heptane and up to *n*-hexadecane and contains 2116 species. To reduce the size of the mechanism we (1) removed all the species containing more than 12 carbon atoms, and (2) removed reactions pertaining to the low-temperature kinetics. We removed reaction classes 10 to 25 as defined by Westbrook et al. to be important only for the low-temperature conditions. The reaction mechanism for *iso*-octane was obtained from Curran et al. (Ref. 7). The high-temperature sub-mechanism for *iso*-octane was extracted from the Curran mechanism and then merged with the reduced Westbrook mechanism for *n*-alkanes, up to *n*-dodecane. The resulting mechanism now contains all the necessary reactions for high-temperature oxidation of all the surrogate fuel components necessary for F-T and bio-jet fuels.

The initial Westbrook mechanism did not contain transport parameters required for flame simulations. Transport parameters for species involved in *n*-heptane and *iso*-octane combustion were obtained from Curran et al. (Refs. 7 and 8). We estimated the transport parameters for the rest of the species in the mechanism.

Our preliminary surrogate mechanism overpredicted the laminar flame speeds and significantly overpredicted the extinction strain rates for all the surrogate components. Based on rate and sensitivity analyses, we found that the base or core mechanism up to C_2 hydrocarbon has the greatest impact on such flame behavior. According to Ji et al. (Ref. 9), transport parameters have greater impact on flame extinction than that on propagation. Initially we updated the transport parameters for core species based on quantum calculations (Ref. 10). This change resulted in improved laminar flame speed predictions but did not improve the extinction strain rate predictions. In order to improve the predictions for flame speed as well as extinction strain rates, we took a comprehensive look at the coupling of transport and kinetic effects. We have improved both aspects during the term of the project.

The following changes were made to the core mechanism

1. Transport parameters for important species in the core mechanism have been updated based upon those used in the USC-"JetSurf" mechanism (Ref. 11).
2. Both the Westbrook et al. (Ref. 6) and the Curran et al. (Ref. 7) mechanisms use explicit reverse rate specification, which obfuscates testing of the thermodynamic consistency of the reactions. We removed explicit reverse rate specification. This forces the reverse rate calculation based on thermodynamics and thus guarantees the mechanism to be microscopically reversible.
3. Updated rate constants for a few key reactions. The specifics of these updates are shown in Table 10. Rate parameters were obtained from the NIST database (Ref. 12) where available.

TABLE 10.—UPDATED RATE COEFFICIENTS FOR KEY REACTIONS IN THE CORE MECHANISM. RATE COEFFICIENTS ARE IN CAL, MOL, CM^3, K UNITS

Reaction	A	n	Ea	Reference
h+o2=o+oh	1.97e+14	0	16540	Baulch et al. 1992
co+oh=co2+h	7.05e+04	2.053	−356	Joshi et al. 2006
Duplicate	5.76e+12	−0.664	332	
hco+m = co+h+m	1.87e+17	−1.0	17000	Friedrichs et al. 2002 * 2.00,
Collision efficiencies: h2/2.0/ h2o/12.0/ co/1.75/ co2/3.6/				adjusted collision efficiency
h+o2(+m)=ho2(+m)	5.12e+12	0.44	0	Troe et al. 2000,
Low	6.33e+19	−1.4	0	m = n2 * 1.10
Troe: 0.5 1e-30 1e+30				
o2/0.85/ h2o/11.89/ co/1.09/ co2/2.18/ ar/0.40/				
h+oh+m=h2o+m	4.40e+22	−2.0	0	GRI-mech 3.0 * 2.00
h2/0.73/h2o/12.0/ co/1.90/ co2/3.8/ ar/0.38/				
ch3+h(+m)=ch4(+m)	1.27e+16	−0.63	383	GRI-mech 3.0
Low	2.48e+33	−4.76	2440	
Troe: 0.7830 74.00 2941.00 6964				
Collision efficiencies: h2/2.0/ h2o/6.0/ ch4/2.0/ co/1.5/ co2/2.0/ c2h6/3.0/ ar/0.7/				
ch2(s)+o2=>h+oh+co	2.80e+13	0	0	GRI-mech 3.0
ch2(s)+o2=co+h2o	1.20e+13	0	0	GRI-mech 3.0
co+ho2=co2+oh	1.57E+05	2.18	17943	You et al. 2007
oh+ho2=h2o+o2	6.67E+28	−4.73	5503	Re-fitted You et al. 2007
Duplicate	2.51E+12	2.0	40000	
hco+h=co+h2	1.20e+14	0	0	Friedrichs et al. 2002
ch4+h=ch3+h2	6.60e+08	1.62	10840	GRI-mech 3.0
c2h5+h=2ch3	9.00e+13	0	0	Estimation
c2h5+h=c2h4+h2	2.00e+12	0	0	Estimation
c2h3+h=c2h2+h2	1.20e+13	0	0	Baulch et al. 1992
c2h3+h=h2cc+h2	8.00e+12	0	0	Estimation
c2h5+h(+m)=c2h6(+m)	5.21e+17	−0.99	1580	GRI-mech 3.0
Low	1.99e+41	−7.08	6685	
Collision efficiencies: h2/2.0/ h2o/6.0/ ch4/2.0/ co/1.5/ co2/2.0/ c2h6/3.0/ ar/0.7/				
ch3+ch3(+m)=c2h6(+m)	2.12e+16	−0.97	620	GRI-mech 3.0
Low	1.77e+50	−9.67	6220	
Troe: 0.5325 151.0 1038.00 4970.0				
Collision efficiencies: h2/2.0/ h2o/6.0/ ch4/2.0/ co/1.5/ co2/2.0/ c2h6/3.0/ ar/0.7/				
c2h4+h(+m)=c2h5(+m)	1.37e+09	1.463	1355	Miller et al. 2004,
Low	2.03e+39	−6.642	5769	adjusted collision efficiency
Troe: -0.569 299.0 9147.0 -152.40				
Collision efficiencies: h2/2.0/ h2o/6.0/ ch4/2.0/ co/1.5/ co2/2.0/ c2h6/2.0/ ar/0.7/				
c3h5-a+h(+m)=c3h6(+m)	2.00e+14	0	0	Tsang et al. 1991
Low	1.33e+60	−12.0	5968	
Troe: 0.020 1096.6 1096.6 6859.5				
Collision efficiencies: h2/2/ h2o/6/ ch4/2/ co/1.5/ co2/2/ c2h6/3/ ar/0.7/				
c2h3+ch3(+m)=c3h6(+m)	2.50e+13	0	0	Tsang et al. 1986
Low	4.27e+58	−11.94	9770	
Troe: 0.175 1340.6 60000.0 10139.8				
Collision efficiencies: h2/2/ h2o/6/ ch4/2/ co/1.5/ co2/2/ c2h6/3/ ar/0.7/c2h2/3.00/ c2h4/3.00/				

To verify that predicted flame speeds for the core components are still in agreement with data, we reran all of the simulations. Comparisons between flame speeds predicted using the current mechanism and data for methane, ethane, and propane (Ref. 13) are shown in Figures 34 to 36. New predictions are in good agreement with the data as well as other literature mechanisms, such as the JetSurF mechanism (Ref. 11).
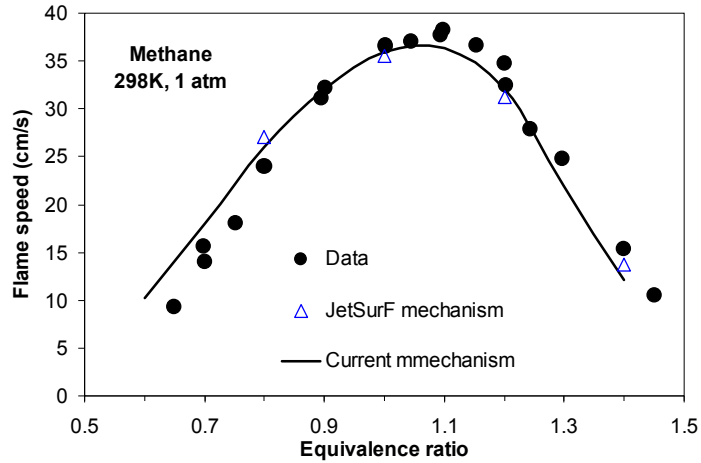
Figure 34.—Comparison of predicted laminar flame speed of methane to the literature data (Ref. 13). Predictions using USC JetSurF mechanism are also shown.
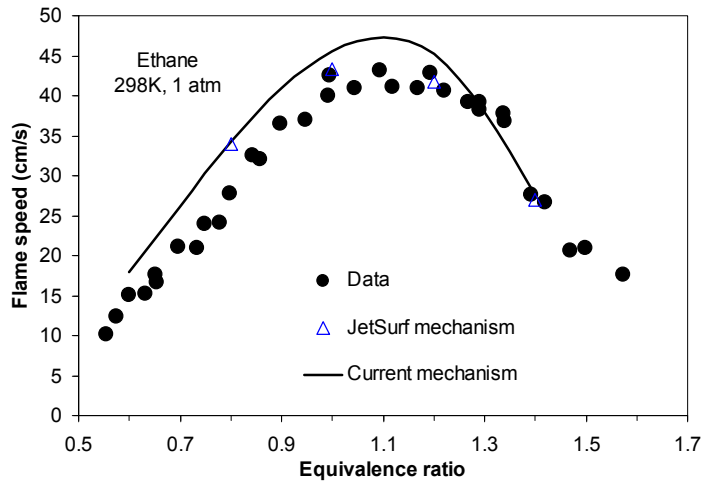
Figure 35.—Comparison of predicted laminar flame speed of ethane to the literature data (Ref. 13). Predictions using USC mech II are also shown.
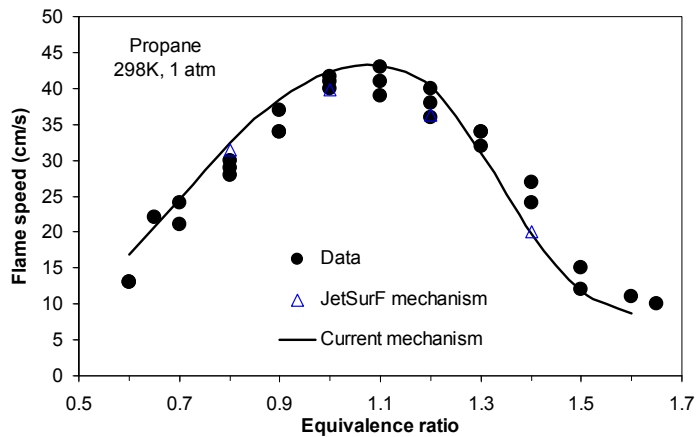
Figure 36.—Comparison of predicted laminar flame speed of propane to the literature data (Ref. 13). Predictions using USC mech II are also shown.
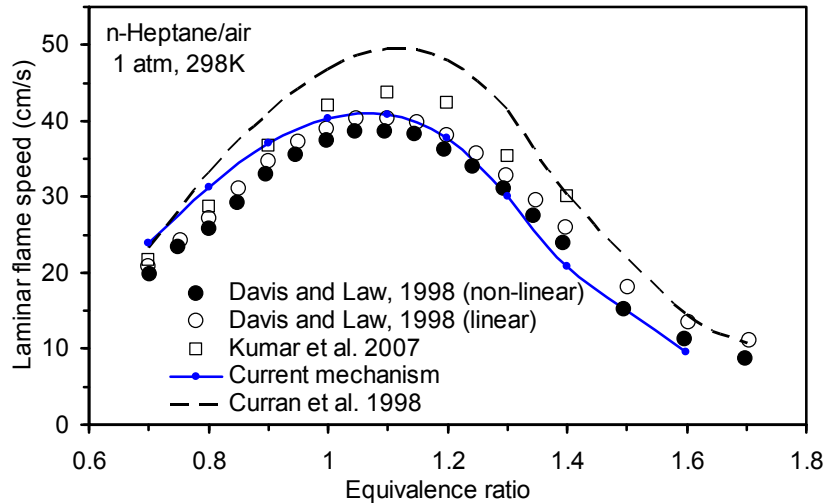
Figure 37.—Comparison of predicted laminar flame speed of *n*-heptane to the literature data (Refs. 14 and 15).

Flame-speed predictions for larger alkanes also agree very well with data. Comparison of the predicted laminar flame speed of *n*-heptane to the data from Davis and Law (Ref. 14) and Kumar et al. (Ref. 15) is shown in Figure 37. Also shown, for reference, is the original *n*-heptane mechanism from Curran et al., which was the baseline model prior to the mechanism-development work performed throughout this project.

Validation comparisons for extinction strain-rate predictions are shown in the next section of this report.

3.3.3   NO$_x$ Sub-mechanism

Building on the baseline alkane mechanism, we also focused on improving and testing a NO$_x$ sub-mechanism for use with the Fisher-Tropsch surrogate simulations. Initial testing of this sub-mechanism was based on experimental data from the literature, which set the stage for later comparisons to NO$_x$ data from the USC experiments.

Our starting point for the NO$_x$ sub-mechanism was an extraction of NO$_x$ kinetics from GRI-Mech 3.0 (Ref. 16). This set of kinetics predicts thermal and prompt NO reasonably well at high temperatures, as the sub-mechanism was validated against data primarily from flame experiments at high temperatures. However, at low- to mid-temperature (below 1500 K), the GRI-Mech 3.0-based sub-mechanism fails to capture some interesting NO$_x$-hydrocarbon mutual sensitization phenomena that has been observed (Ref. 17). Recently, several researchers have proposed new and updated mechanisms for the NO$_x$ sensitization effect, as well as for missing low-temperature NO$_x$ pathways, such as HONO production. These reactions can be important during ignition and for conditions where there are relatively high NO$_x$ levels. For this work, our goal is to include a fairly complete NO$_x$ sub-mechanism that covers a wide range of temperature, pressure, and fuel conditions. The complete mechanism can be subsequently reduced for specific applications (such as high-temperature-only conditions), using automated mechanism-reduction techniques that have been developed at Reaction Design.

In selecting GRI-Mech 3.0 as the starting point, three other sub-mechanisms were considered but after evaluation were discarded. During this quarter, four other mechanisms have been acquired for consideration of additional pathways. All eight of these NO$_x$ sub-mechanism sources are listed in Table 11, along with their applicability limits. The HCN mechanism from Dagaut et al. (Ref. 17) is the most recent one that considers various pathways and isomers in NO$_x$ production. However, it does not include NO-HC mutual sensitization. Mechanisms from Rasmussen, et al. (Ref. 18) and Sivaramakrishnan, et al. (Ref. 19) include such mutual sensitization effects. They include complex species such as R-NO$_x$ and R-O-NO$_x$, where R can be OH, CH$_3$, and C$_2$H$_5$ radical groups. All three

mechanisms (Nos. 5, 7, and 8) have been used to improve the GRI-Mech-based NO_x sub-mechanism. The 1998 sub-mechanism from Glarborg et al. (Ref. 20) contains unproven pathways that were discarded in more recent mechanisms, so was not considered in this work. Comparisons of the resulting NO_x sub-mechanism that will be used in this work to available experimental data will be reported in the next work period.

TABLE 11.—SURVEY OF RECENTLY PUBLISHED NO_X MECHANISMS

No.	Source	Temperature range, K	Pressure range, atm	Fuels used in validation	Comments	Considered in this work?	Ref.
1	GRI-Mech 3.0	>1300	0.03 to 80	CH_4	High temperature	Yes	16
2	Mueller et al. 2000	950 to 1040	0.5 to 10	$CO/H_2O/NO/$ SO_2	Not for HCs; no prompt pathways	No	21
3	Hori et al. 1998	600 to 1100	1	$C_1 - C_3$	No sensitization; limited validation	No	22
4	Konnov 2007	1100 to 2200	0.1 to 14	$N_2O/NH_3/$ N_2H_4	Not for HCs	No	23
5	Dagaut et al. 2008	900 to 1500	1 to 10	----------	HCN review	Yes	17
6	Glarborg et al. 1998	800 to 1500	1	$C_1 - C_2$	Superseded by later work	No	24
7	Rasmussen et al. 2007	600 to 900	10 to 100	CH_4	Low temperatures; high pressures	Yes	18
8	Sivaramakrishnan et al. 2007	1000 to 1500	10 to 50	$CH_4/C_2H_6/NO$	Low temperatures; high pressures	Yes	19

3.3.4 PAH Sub-mechanism

To facilitate future soot modeling, we further updated the detailed chemical kinetics mechanism for the F-T and bio-jet surrogate fuels to include pathways for PAH formation leading to soot and the HACA-based soot-growth mechanism. Several literature mechanisms have been developed to predict PAH from the combustion of small alkanes and alkenes, such as ethylene, methane, propane, etc. The hydrogen-abstraction-acetylene-addition (HACA) mechanism for molecular-weight growth from unsaturated C_2 hydrocarbon flames was first developed by Frenklach and coworkers (Refs. 25 to 27) and has been a popular mechanism used by many studying combustion-generated soot in the last decade. Appel et al. (Ref. 28) advanced this mechanism by improving the rate constants for several important pathways. In the last five years, other researchers have considered more reaction pathways to better describe the PAH chemistry and to account for reactions in non-C_2 flames. Skjøth-Rasmussen et al. (Ref. 29) studied PAH-formation mechanisms from fuel-rich methane oxidation in a laminar flow reactor. Richter et al. developed a mechanism for PAH formation in benzene flames. Recently Zhang et al. (Ref. 31) developed a mechanism to describe various benzene formation pathways in several fuels.

It is important to gather the kinetics knowledge available in the literature on various PAH reaction pathways to develop a comprehensive, detailed reaction mechanism that can apply to a broad range of combustion systems and fuels. We started this process by first incorporating the Appel et al. (Ref. 28) PAH sub-mechanism to the current F-T fuel surrogate mechanism. We then added the PAH sub-mechanisms from the Zhang et al. (Ref. 31) and Skjøth-Rasmussen et al. (Ref. 29). The addition of these PAH sub-mechanisms increased the size of the master mechanism by 159 species and 831 reactions. These three sources describe a variety of PAH formation pathways and we expect them to provide a reasonably good starting point for future mechanism improvements.

3.3.5 Soot Mechanism

The literature data on soot-growth mechanisms, i.e., after the particles are nucleated from PAH gas-phase precursors, is quite limited. In this project, we incorporated the Appel et al. (Ref. 28) soot-growth mechanisms as a starting point in development of a more comprehensive soot-growth description, using the very general surface-chemistry capabilities of CHEMKIN-PRO. We then extended the original mechanism to include condensation of various PAHs, such as pyrene, naphthalene, indene, etc., on the soot particle after nucleation. This path is included in addition to the traditional HACA growth mechanism that involves acetylene-based carbon addition only.

3.3.6 Mechanism Reduction

During the course of this project, Reaction Design tested recently implemented automated mechanism-reduction capabilities that work in combination with CHEMKIN-PRO simulations. These methods have been implemented to allow operation on a CHEMKIN-PRO "project" that may include a number of different conditions for one or more types of reactor models. These conditions are set up as a "parameter study" in the CHEMKIN context, and are run first with the full "master" mechanism that includes all the elementary reactions. The user can then specify an error tolerance for any target in the simulation, such as laminar flame speed, or a particular species concentration prediction. An iterative approach then employs one or more reduction methods to determine the smallest possible mechanism that can provide the targeted predictions within the specified error. All comparisons are made relative to predictions under the same conditions using the master mechanism. In this way, validation and improvement of predictions relative to experimental data are separable activities from the automated mechanism-reduction process.

To produce the smallest reasonable F-T surrogate for CFD modeling, we started with the 2-component surrogate rather than the 3-component surrogate, recognizing that we will have to make some compromises on applicability to reduce the compute time of a typical simulation. The high-temperature F-T surrogate master mechanism used for this study contains 549 species and 3246 reactions. The mechanism consists of elementary reactions and accounts for a multitude of reaction pathways that allow prediction of laminar flame speeds and flame-extinction strain rates, over a wide range of temperatures, pressures and equivalence ratios.

The CHEMKIN-PRO Flame-speed Calculator, which determines the flame-propagation speed for laminar, one-dimensional, steady-state, premixed flames, has been used for all the calculations described here. For these calculations, we used a 6-cm domain for the computational grid in all cases. This is to ensure enough space for the flame to be contained within the computational domain and to satisfy the flame-speed model requirements of zero gradients at both the hot and cold boundaries. The solution tolerances have been set using absolute and relative tolerances of 10^{-12} and 10^{-5}, respectively, for all calculations, assuring accurate predictions of trace radical species as well as major species. Mixture-averaged transport properties were used, since use of multicomponent transport properties was more computationally expensive and did not impact the calculated flame-speed values significantly. A grid-resolution dependency study was also performed, resulting in the conclusion that ~400 grid points should be required to eliminate any grid-related uncertainty in the simulations.

The mechanism reduction operates on model-solution results coming from a parametric matrix of runs representing the target conditions. The final reaction set is obtained from the union of the reduced reaction sets of the individual targets so that the reduced mechanism generated is valid for all the user-specified target conditions. The reduction can therefore be achieved accurately while accounting for spatial and temporal variations, as well as variations in operating conditions.

Three methods are available in the CHEMKIN-based mechanism-reduction facility; these have been tested here for the task of reducing the 2-component F-T surrogate mechanism.

1. Directed Relation Graph (DRG) method (Refs. 2 and 3).
2. Principle Component Analysis (PCA) method (Ref. 32).
3. Computational Singular Perturbation (CSP) method (Refs. 33 to 35).

The first two of these methods produce skeletal mechanisms. In skeletal mechanisms, the reactions that remain in the mechanism have the same reaction paths and reaction rate parameters as in the master mechanism, and the species identities for the remaining species are also identical to their counterparts in the master mechanism. In this way reactions and species have either been left unmodified or have been removed entirely in comparison to the master mechanism. In more severe mechanism-reduction methods, there can be lumping of species and/or reactions, also reactions can be replaced by algebraic expressions based on quasi-steady-state assumptions.

The first skeletal mechanism-reduction method, the Directed Relation Graph (DRG) method, was originally developed at Princeton to efficiently resolve species coupling, such that unimportant species can be identified and eliminated to create skeletal mechanisms (Refs. 2 and 3). Species coupling indicates that the removal of one species from the mechanism induces immediate errors to the production rate of another species. DRG relies on the directed relation graph constructed using the production rates of species to resolve species coupling. Using an efficient search algorithm, the entire reduction can be completed in a time scale that is linearly proportional to the number of reactions in the mechanism. The DRG method produces a skeletal reaction mechanism in CHEMKIN input format and can operate on species rates-of-production data determined from the solution of any CHEMKIN reactor model.

The other skeletal mechanism-reduction method considered, the Principle Component Analysis (PCA) method (Ref. 32), employs an eigenvalue-eigenvector analysis to extract kinetic information from linear sensitivities calculated for species of a reacting system. It studies the effect on the calculated behavior of a reaction mechanism brought about by a variation in the rate coefficients. The effect is most sensitive to changes in the rate coefficients along the principle axis corresponding to the largest eigenvalue of the sensitivity matrix and is least sensitive to changes along the axis corresponding to the smallest eigenvalue. Therefore reactions in the principle components with small eigenvalues can be dropped.

The third reduction technique is a severe reduction method, the Computational Singular Perturbation (CSP) method (Refs. 33 to 35). This method is based on the separation of time-scales between chemical species. It uses the time-dependent eigenvectors of the Jacobian matrix of the chemical source terms to decompose the phase space. The decomposition process introduces slow and fast importance indices assessing the relative influence of the slow and fast kinetic components, respectively. Using these indices, one can eliminate the quasi-steady-state-approximation (QSSA) species from the mechanism by solving for them explicitly in terms of those species that are treated kinetically. The rate equations of the remaining reactions are expressed in terms of the rate equations of the reactions in the original mechanism.

Skeletal mechanisms were first generated using the DRG and PCA methods, and these skeletal mechanisms were subsequently reduced further using the severe-reduction technique CSP. Our findings were that DRG performed better than PCA for generating skeletal mechanisms. Consequently, the mechanisms described in this section employ a combination of DRG and CSP reduction techniques.

Three reduced mechanisms have been generated. These differ in how much discrepancy we were willing to tolerate between the flame-speed predictions of the master mechanism and the reduced mechanism. In general, the more discrepancy we were willing to tolerate, the more we could reduce the mechanism. The master mechanism consisted of 549 species and we were able to achieve reductions from 73 to 90 percent in terms of the number of species. The three mechanisms generated were as follows:

1. A conservatively reduced mechanism, consisting of 148 species. The aim was to keep the discrepancies in flame speeds between the reduced and master mechanism to less than ±0.5 cm/sec.
2. A less conservatively reduced mechanism consisting of 95 species. The aim was to keep the discrepancies in flame speeds to less than ±1.5 cm/sec.
3. A more aggressively reduced mechanism consisting of 56 species. The aim was to get the number of species close to 50, while maintaining reasonable discrepancies over most of the equivalence ratio range.

These mechanisms were assembled based on a combination of the DRG and CSP methods. Table 12 shows the reduction achieved through DRG and the additional reduction through CSP. CSP was applied for mechanisms 1 and 3 only. We note that CSP reduction had limited additional reduction value compared to the pure skeletal DRG reduction.

The flame speed predictions were made for the same F-T surrogate described above, and for the same conditions of 403 K and 1 atm. Figure 38 shows the comparisons of flame-speed predictions between the reduced mechanisms and the master mechanism. Table 13 gives the corresponding discrepancy values, for ease of understanding the information.

TABLE 12.—REDUCTIONS ACHIEVED THROUGH DRG AND CSP

Mechanism	Number of species after DRG reduction	Number of species after subsequent CSP reduction
Master mechanism contains 549 species		
Reduced mech 1	174	148
Reduced mech 2	95	95 (no CSP applied)
Reduced mech 3	64	56

TABLE 13.—DISCREPANCIES OF PREDICTED FLAME SPEEDS USING REDUCED
MECHANISMS, IN COMPARISON WITH THE MASTER MECHANISM

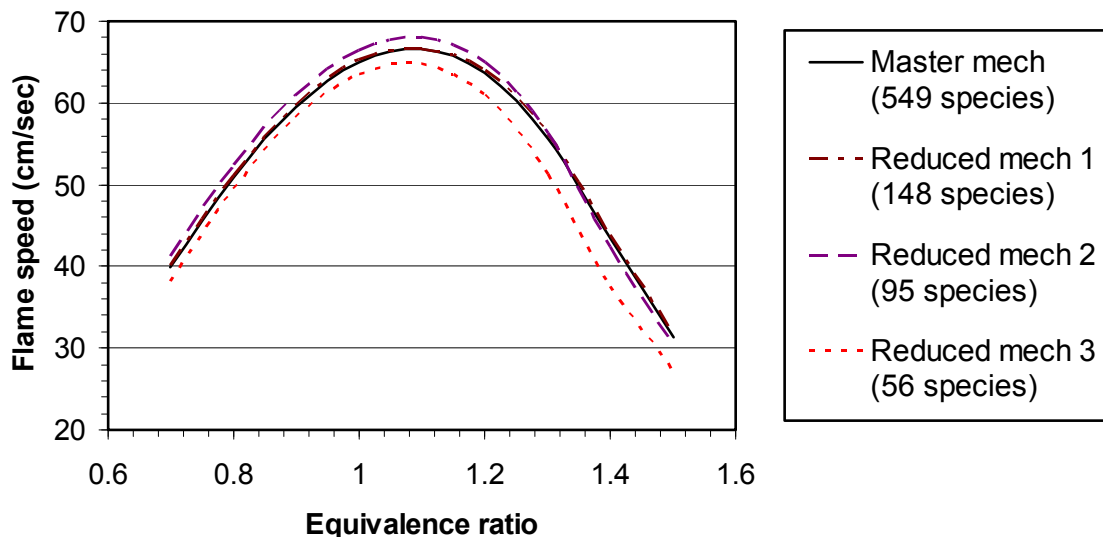| Equivalence ratio	Flame speed, master mechanism, cm/sec	Flame speed discrepancy: Master mechanism minus reduced mech 1 (148 species), cm/sec	Flame speed discrepancy: Master mechanism minus reduced mech 2 (95 species), cm/sec	Flame speed discrepancy: Master mechanism minus reduced mech 3 (56 species), cm/sec
0.7	39.85	−0.20	−1.27	1.74
0.8	50.93	−0.18	−1.39	1.53
0.9	59.47	−0.21	−1.52	1.30
1	65.00	−0.24	−1.51	1.52
1.1	66.62	−0.01	−1.48	1.87
1.2	63.69	−0.34	−1.32	2.73
1.3	55.61	−0.40	−0.66	4.36
1.4	43.44	−0.30	1.16	5.94
1.5	31.40	−0.27	1.15	4.23

Figure 38.—Comparisons of predicted flame-speed for *n*-dodecane, using the full master mechanism versus different degrees of mechanism reduction.

From Table 13, we can see that our most conservatively reduced mechanism (148 species mech) predicts flame-speed values that are very close to the master mechanism, within 0.4 cm/sec over the range of equivalence ratios. As we keep reducing the number of species, the discrepancy increases. The 95-species reduced mechanism is still reasonable, with discrepancies within ~±1.5 cm/sec. The 56-species mechanism is reasonable over equivalence ratios of 0.7 to 1.2, with discrepancies within 3 cm/sec. The discrepancy for the 56-species mechanism increases to ~4 to 6 cm/sec for more fuel-rich conditions. It fortuitously happens in this case that for these fuel-rich conditions, the 56-species reduced mechanism predicts values closer to data than the master mechanism. However, the main point for this study is that we can produce a range of reduced mechanisms and determine quantitatively the discrepancies associated with these reduced mechanisms. The Reaction Workbench, which is under development, gives the user control over how much discrepancy can be tolerated, and over what range of conditions the mechanism reduction is to be performed.

A logical question at this stage would be how large the discrepancy would be if we keep reducing the mechanism further. It appears that as we go below ~50 species, the discrepancy becomes fairly large. A 47-species mechanism had a significant discrepancy of the peak flame speed and flame speed at fuel-rich conditions, as much as 10 cm/s.

Using CHEMKIN-PRO's Reaction Path Analyzer for understanding the mechanism and reaction pathways, this section provides some insights as to why the mechanism becomes sensitive to further removal of species. For the flame speed case at equivalence ratio = 1.5, and using the master mechanism, Figure 39 shows the important pathways of *n*-decane, at 775 K. It can be seen that the large *n*-decane molecule breaks down into smaller alkenes, such as 1-hexene and ethylene. Figure 40 shows the normalized sensitivity of flow rate to reaction rates, which is equivalent to the sensitivity of the laminar flame speed to the reaction rates, for the equivalence ratio = 1.5 case. Again, the most sensitive reactions involve hydrogen chemistry, and small hydrocarbon chemistry. This leads us to conclude that the successful skeletal mechanism reduction extends to the reactions and species involved in this core C_0-C_3 mechanism, as well as the original decomposition of the fuel molecules.
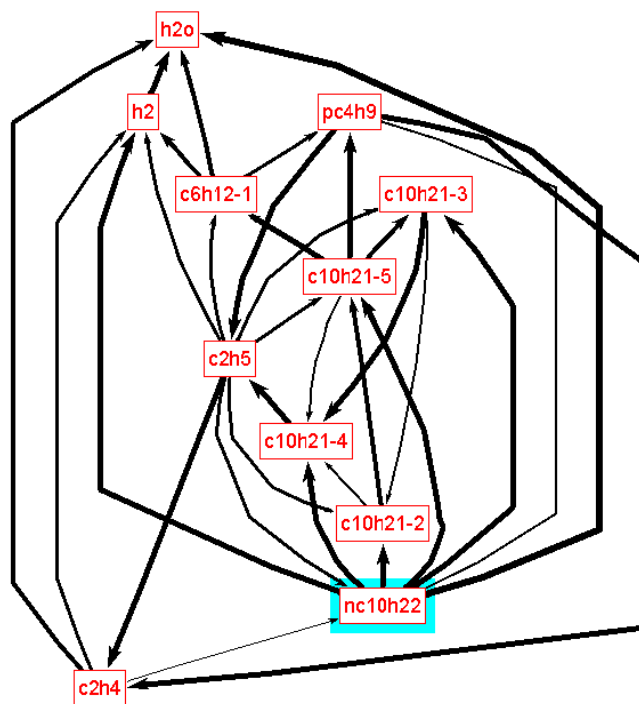

Figure 39.—Reaction pathways of *n*-decane at 775 K, and for the equivalence ratio = 1.5 case.
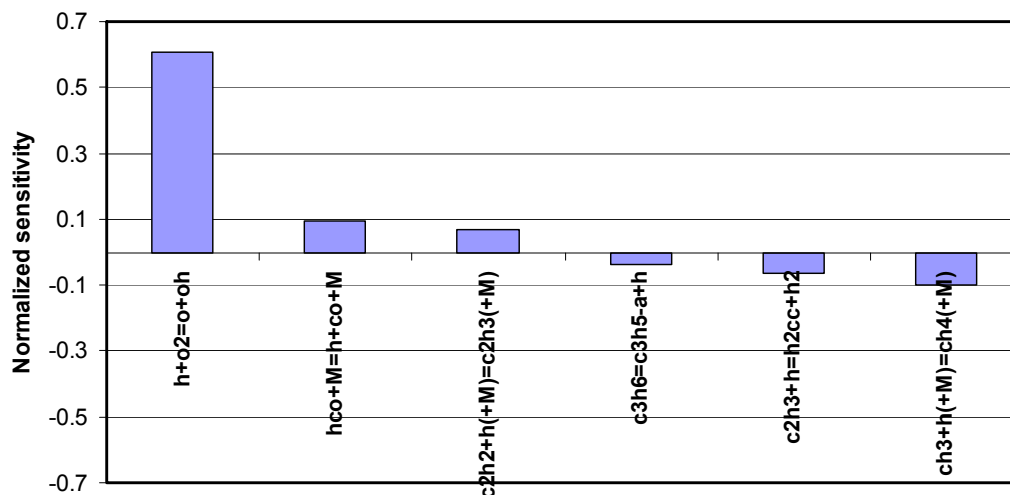
Figure 40.—The most sensitive reactions: Normalized sensitivity coefficients for flow rate, for the equivalence ratio = 1.5 case.

3.4   Simulations of the Flame Experiments With NO$_x$ and Soot Predictions

Throughout this project, we have performed numerous simulations of the USC flame experiments, as well as supplementary experiments reported in the literature, for the purpose of verifying and improving the fuel-component mechanisms and for testing the F-T fuel-surrogate definition. This was an iterative process that sometimes led to additions or corrections to the mechanism and sometimes led to re-assessment of the accuracy of or uncertainties in the experimental data. Here we report results using the latest version of the mechanism compared to the latest experimental data after improvements to both model and experiment were completed per the discussion in the previous sections. The reporting for these simulations is organized as follows: (1) general combustion behavior by fuel component or surrogate (*n*-dodecane, *n*-decane, *iso*-octane or F-T fuel surrogate), followed by (2) NO$_x$ predictions for a variety of fuel components (3) autoignition temperature predictions for various fuel components and the F-T surrogate, and (4) PAH and soot predictions.

3.4.1   *Iso*-Octane—Ignition Times and Laminar Flame Speeds

Ignition-delay time data from Davidson et al. (Ref. 36) and Vermeer et al. (Ref. 37) have been extracted and catalogued. Both the shock-tube experiments involved reflected shock waves. The modeling has been performed using the CHEMKIN-PRO (Ref. 1) zero-dimensional transient closed homogeneous reactor model, under constant volume conditions. This modeling approach is consistent with other reports in the literature for modeling ignition following reflected shock waves. CHEMKIN-PRO allows various definitions of ignition time. For the cases modeled, we have used an ignition time defined by the inflection point in the predicted temperature versus time profile.

Figure 41 compares the calculated ignition delay times with the experimental data of Davidson et al. (Ref. 36). The figure shows the effects of varying equivalence ratio on the ignition-delay times, over temperatures of ~1300 to 1750 K. The model predictions agree well with the experimental data. They also show that the fuel-lean mixtures ignite earlier than the stoichiometric and fuel-rich mixtures, at these temperatures. The conditions include 1.5 atm and Ar dilution of ~93 percent.

Figure 42 compares the model predictions with the experimental data of Vermeer et al. (Ref. 37). The stoichiometric *iso*-octane/O$_2$ is diluted in 70 percent Ar. The experimental data are taken at pressures of ~1.7 to 2.5 atm, and the model predictions have been performed at 2 atm. The model predictions agree well with the experimental data over the temperature range shown.
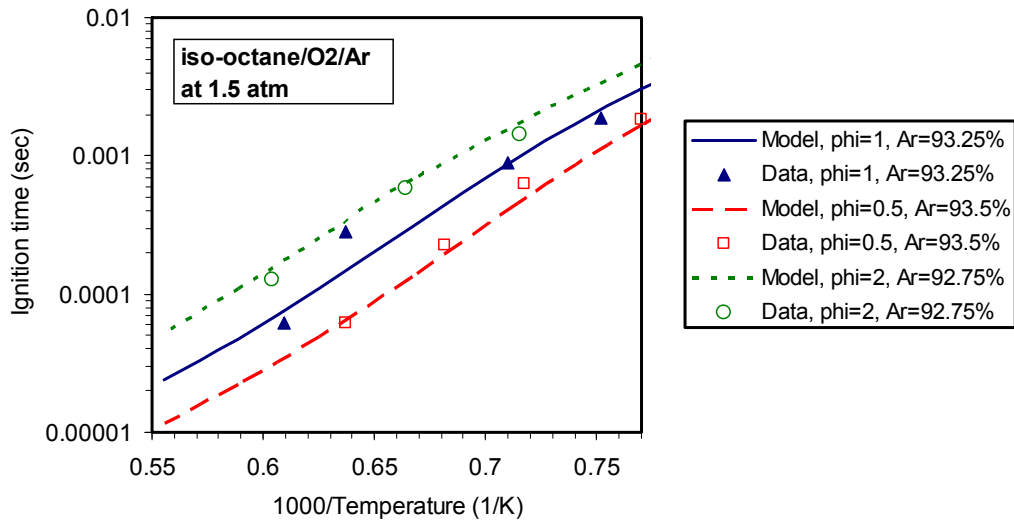
Figure 41.—Effect of equivalence ratio on *iso*-octane ignition-delay times. Comparison of calculated values with the experimental data of Davidson et al. (Ref. 36) at 1.5 atm. Mixture diluted with ~93 percent Ar.
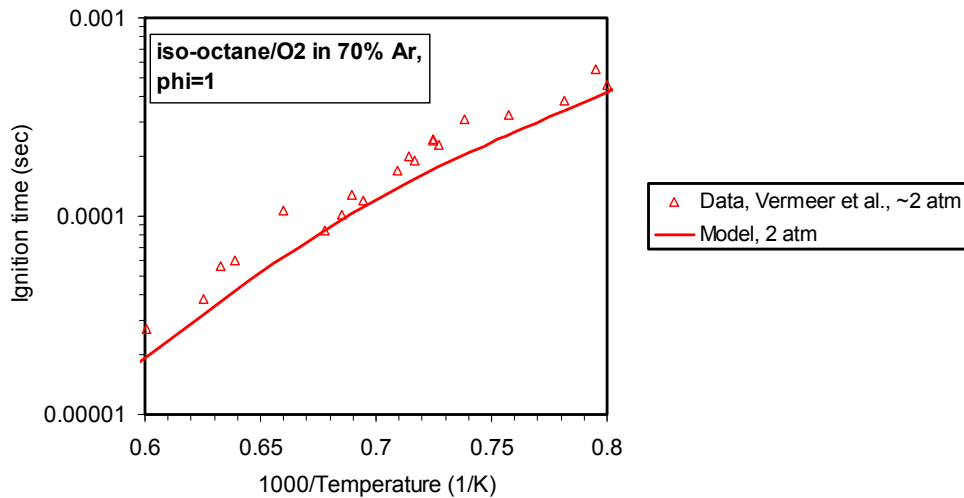
Figure 42.—Comparison of calculated *iso*-octane ignition-delay times with the experimental data of Vermeer et al. (Ref. 37). Conditions include 70 percent Ar dilution, pressure of 2 atm and a stoichiometric mixture.

Experimental data of *iso*-octane/air laminar flame speeds have been collected from Davis et al. (Ref. 14), Huang et al. (Ref. 38), Kumar et al. (Ref. 15), and Kwon et al. (Ref. 39). The model predictions are compared with these data in Figure 43. The uncertainty in experimental velocity measurements has been reported to be 1 to 2 cm/sec by Davis et al. Following the measurements, the unstretched laminar flame speed is determined using linear or non-linear extrapolation to zero stretch, and the differences between the two extrapolation techniques has been reported to be 1 to 2 cm/sec by Davis et al. and Huang et al. Linear extrapolation has been used by Davis et al., Kumar et al. and Huang et al., while Kwon et al. report using an empirical technique. Of the experimental flame-speed data in Figure 43, the data of Kwon et al. seems to have significant differences with the other three sets of data. Kwon et al. estimated a 10 percent uncertainty in their flame-speed data, and mention that experimental problems surrounding the vaporization and mixing of liquid fuels are factors contributing to experimental uncertainties. They do however account for flame stretch, and the reason for the differences with the other sets of data is not entirely clear.
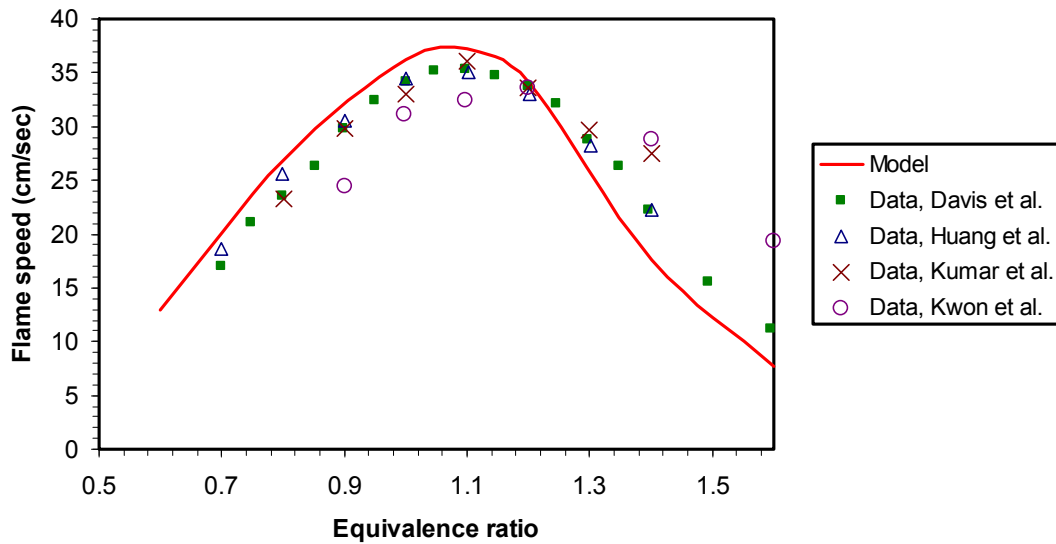
Figure 43.—Laminar flame speeds of *iso*-octane/air at ~298 K and 1 atm. Experimental data compared with model predictions over a range of equivalence ratios.

Figure 44.—Calculated *n*-decane/air ignition-delay times compared with the data of Zhukov et al. (Ref. 40). Conditions include pressure of 13 atm and a stoichiometric mixture.

Comparing the data of Davis et al., Huang et al., and Kumar et al. with the model predictions, the model predicts the flame speed well for the fuel-lean and stoichiometric conditions, but under-predicts flame speeds in the fuel-rich regime. In the fuel-lean and stoichiometric regime, considering the uncertainty in the flame-speed data discussed above, the model predictions can be considered to be in good agreement with the experimental data. The peak flame speed occurs at an equivalence ratio of ~1.1.

3.4.2 *n*-Decane—Ignition Times and Laminar Flame Speeds

Figure 44 compares the calculated ignition-delay times with the experimental data of Zhukov et al. (Ref. 40) for a stoichiometric *n*-decane/air mixture, at a pressure of 13 atm. The predictions agree well with the experimental data over the temperature range shown.

Figure 45 compares model predictions with the experimental data of Pfahl et al. (Ref. 41) for a stoichiometric *n*-decane/air mixture, at a pressure of 13 atm. The predictions compare well with the data at these temperatures.

As discussed in the first section of this report, the extraction of laminar flame speed from the raw measurement must be performed very carefully. Noticeable differences in results using linear versus non-linear extrapolation methods, for example, were observed by USC researchers. As seen in Figure 46, various extrapolations or experimental techniques may produce significantly different laminar flame-speed measurements. We expect non-linear extrapolation to provide more accurate indication of the laminar flame speed than one would expect to model with a one-dimensional flame-speed simulation. All data from the USC Flame Facility that has been used for comparison with our model, then, employs the non-linear extrapolation method, unless explicitly stated otherwise.
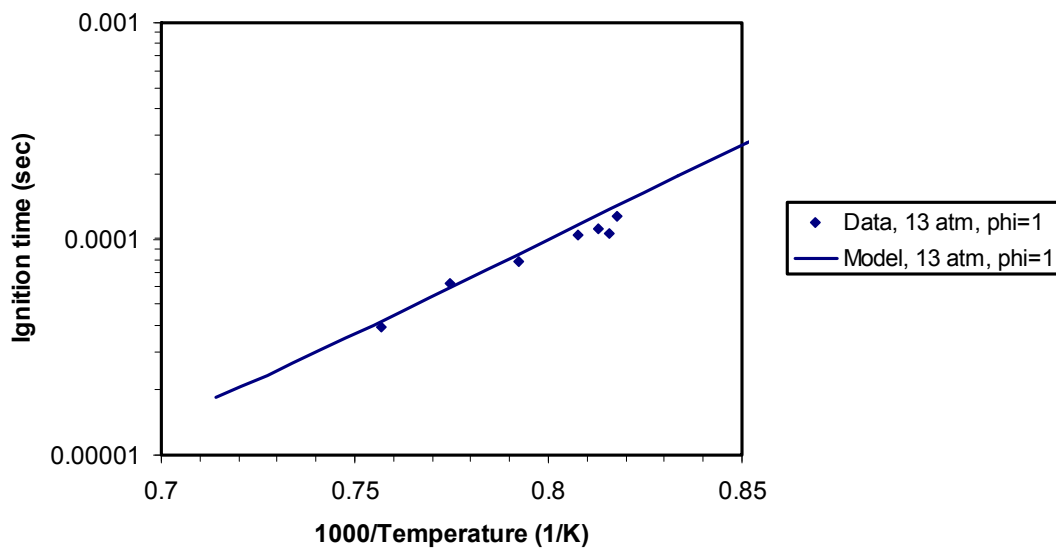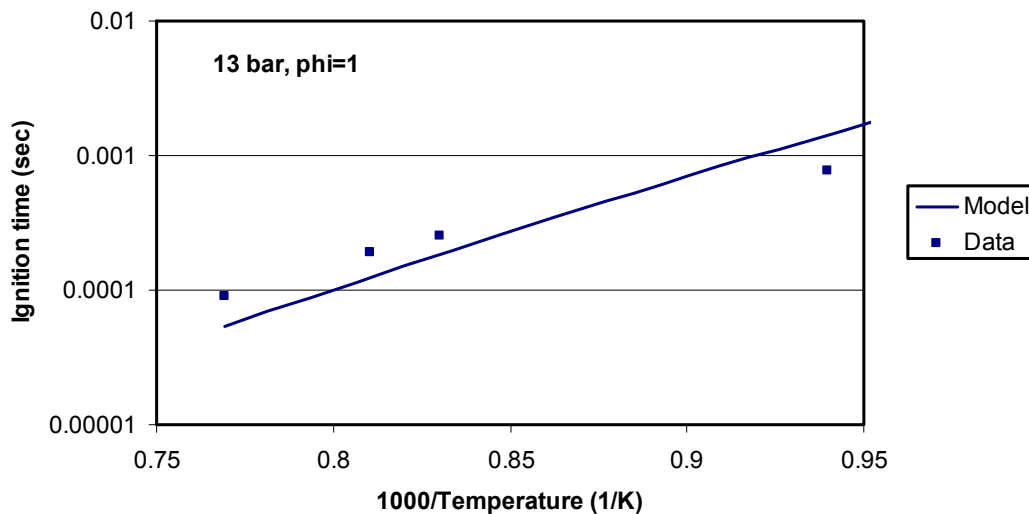

Figure 45.—Calculated *n*-decane/air ignition-delay times compared with the data of Pfahl et al. (Ref. 41). Conditions include pressure of 13 atm and a stoichiometric mixture.
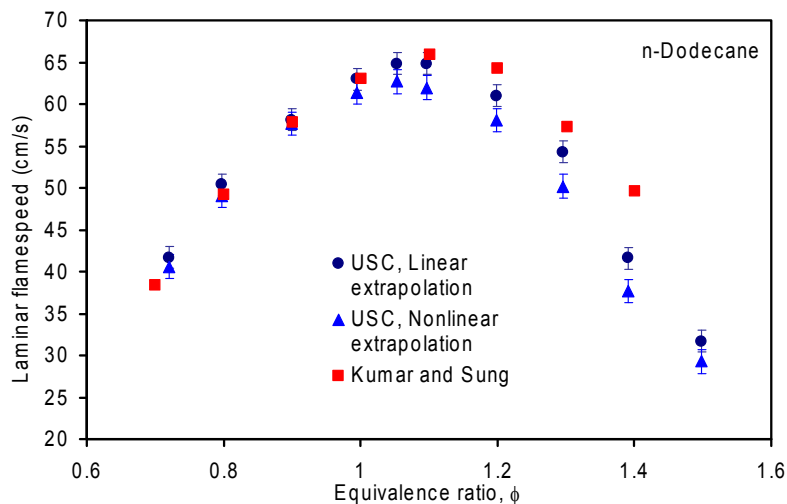

Figure 46.—Impact of linear and non-linear extrapolation of flame velocity to zero stretch to obtain laminar flame speed of *n*-dodecane using opposed flow burner configuration at USC Flame Facility. Data from Kumar and Sung (Ref. 42) are based on linear extrapolation method.
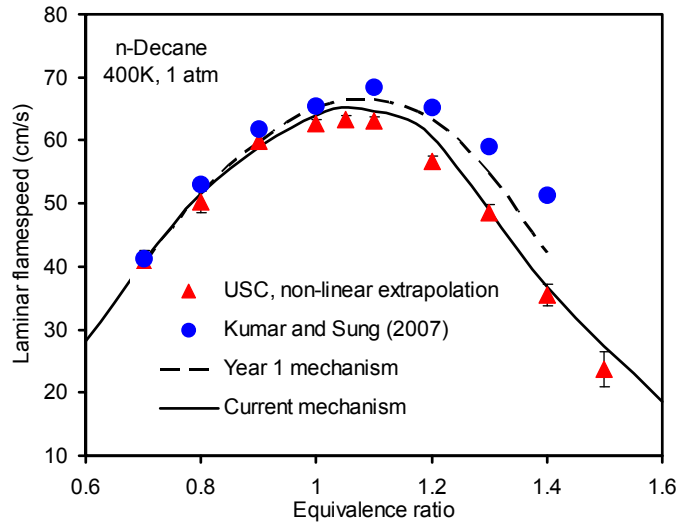
Figure 47.—Comparison of predicted laminar flame speed of
n-decane to the experimental data from USC and Kumar
and Sung (Ref. 42).

Comparison of the predicted laminar flame speed of *n*-decane to experimental data of USC and others is shown in Figure 47. We can see that the current mechanism displays improved flame-speed predictions over the presented range of equivalence ratios.

More experimental data for *n*-decane have been obtained from two literature sources: Delfau et al. (Ref. 43) and Doute et al. (Ref. 44). Both studied rich *n*-decane combustion using a burner-stabilized flame, but at different conditions. Delfau et al. studied the combustion at low pressure (6 kPa) and an equivalence ratio of 1.9 (*n*-decane/O_2/Ar), while Doute et al. used atmospheric pressure and an equivalence ratio of 1.7 (*n*-decane/O_2/N_2). Delfau et al. used molecular beam-mass spectrometer technique, and Doute et al. used gas chromatography.

The modeling of these experiments has been performed under fixed-temperature conditions, using the temperature profile reported in the papers. Doute et al. estimated the uncertainty in their temperature measurements as ±5 percent.

Figures 48 to 52 compare the calculated species profiles for the fuel-rich *n*-decane/O_2/N_2 flame at atmospheric pressure, with the experimental data of Doute et al. The conditions include atmospheric pressure and an equivalence ratio of 1.7 (mole%: 3.2% *n*-decane, 28.6% O_2, 68.2% N_2). The inlet velocity was 11.7 cm/sec. The comparisons show good agreement for most species. Figure 48 shows the profiles of the fuel and oxidizer, *n*-decane and O_2. These reactants are seen to be consumed within ~2 mm from the burner, and the model predictions agree well with the experimental data of Doute et al.

Figure 49 shows the profiles for CO and CO_2. For these fuel-rich conditions, more CO is formed than CO_2, and the model predictions follow the correct trends.

Figure 48.—Comparison of predicted species profiles for *n*-decane/O_2/N_2 burner-stabilized flame with the experimental data of Doute et al. (Ref. 44).

Figure 49.—Comparison of predicted species profiles for *n*-decane/O_2/N_2 burner-stabilized flame with the experimental data of Doute et al. (Ref. 44).

Figure 50 shows the profile for another major product, H_2. The model predictions of the H_2 profile agree well with the experimental data.

Figure 51 shows the profiles of the major hydrocarbon species ethylene and acetylene. The location of the ethylene peak concentration is modeled well, but the magnitude of the peak is under-predicted by the model. The model predicts correctly that ethylene has the highest peak concentration of all stable hydrocarbons. Acetylene, which is a potential soot precursor, has a significant concentration under these fuel-rich conditions, and the model prediction of the acetylene profile agrees well with the experimental data.

Figure 50.—Comparison of predicted species profiles for *n*-decane/O_2/N_2 burner-stabilized flame with the experimental data of Doute et al. (Ref. 44).

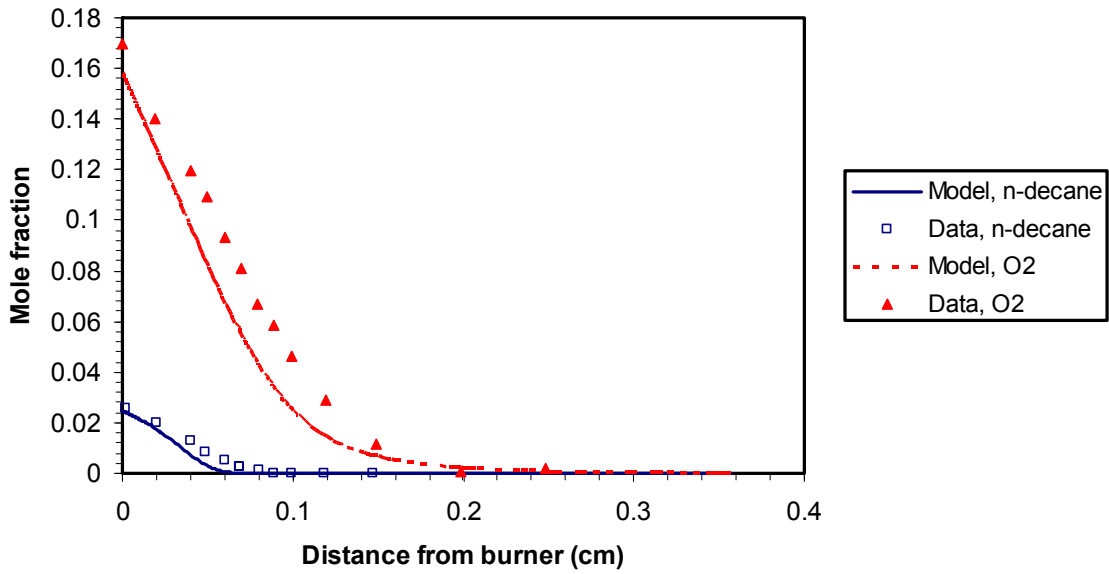Figure 51.—Comparison of predicted species profiles for *n*-decane/O_2/N_2 burner-stabilized flame with the experimental data of Doute et al. (Ref. 44).

Figure 52 shows the other major hydrocarbons. Both the alkanes methane and ethane have lower concentrations than the alkene (ethylene) and alkyne (acetylene) in the previous figure. The model predicts the correct trend that more methane is formed than ethane. While the model predictions agree well with the experimental data for methane, the model under-predicts the peak for ethane; the concentration of ethane is however small compared to the other hydrocarbons shown.

Figures 53 and 54 shows the comparisons of model predictions with the experimental data of Delfau et al. The fuel-rich n-decane/O_2/Ar combustion occurs at a low pressure of 6 kPa and at an equivalence ratio of 1.9 (mole%: 5.1% n-decane, 41.2% O_2, 53.7% Ar). The inlet velocity was 18.6 cm/sec. These simulations have also been performed using fixed-temperature conditions specified by the experimental temperature profile. Figure 53 shows the profiles of the major products CO and CO_2. Since the equivalence ratio employed by Delfau et al. is 1.9, the peak CO/CO_2 ratio is large. The model predictions agree well with the experimental data.
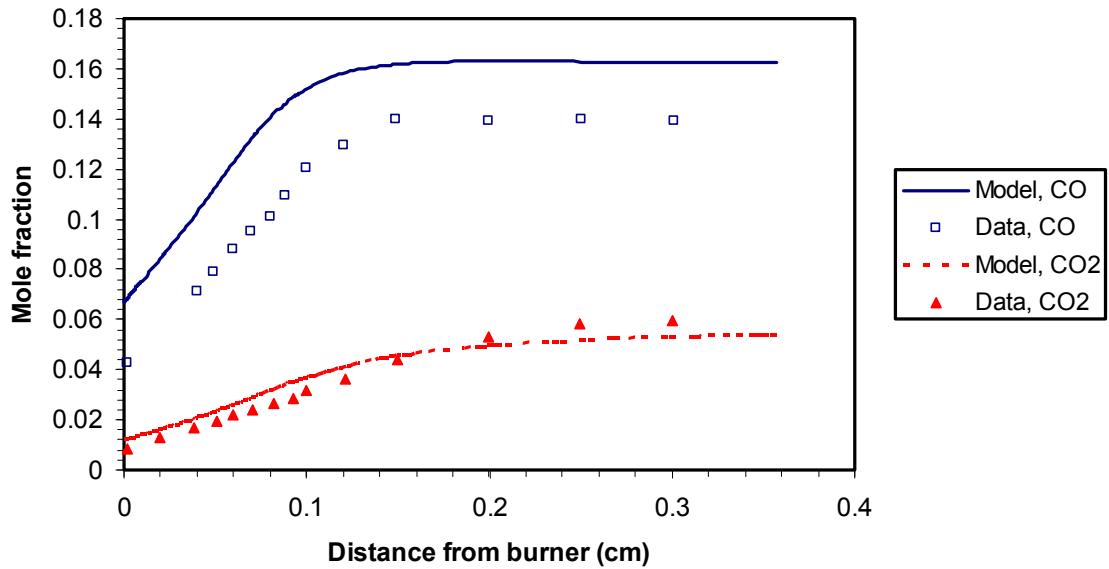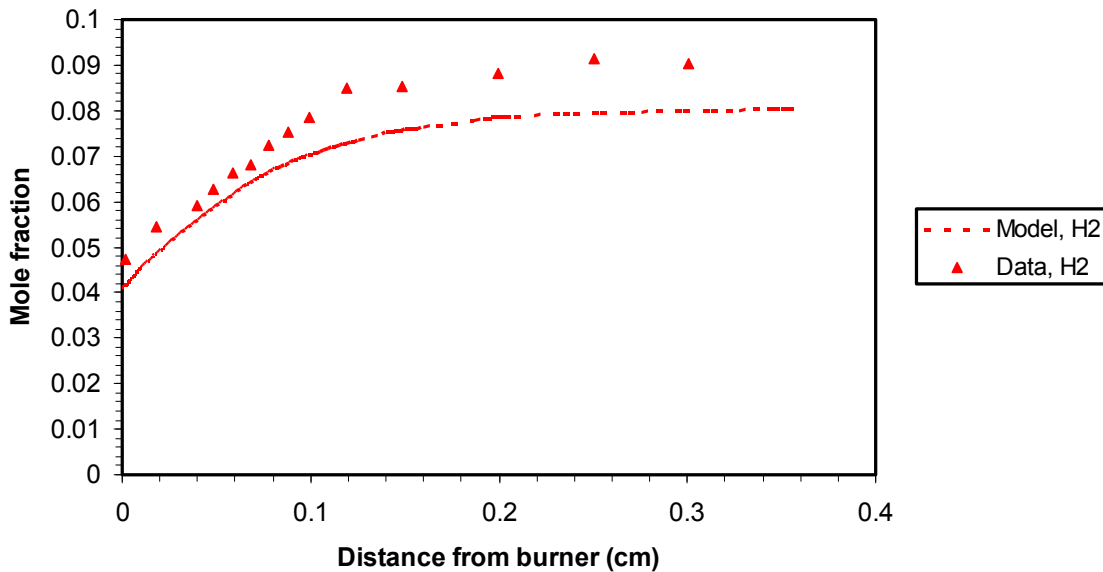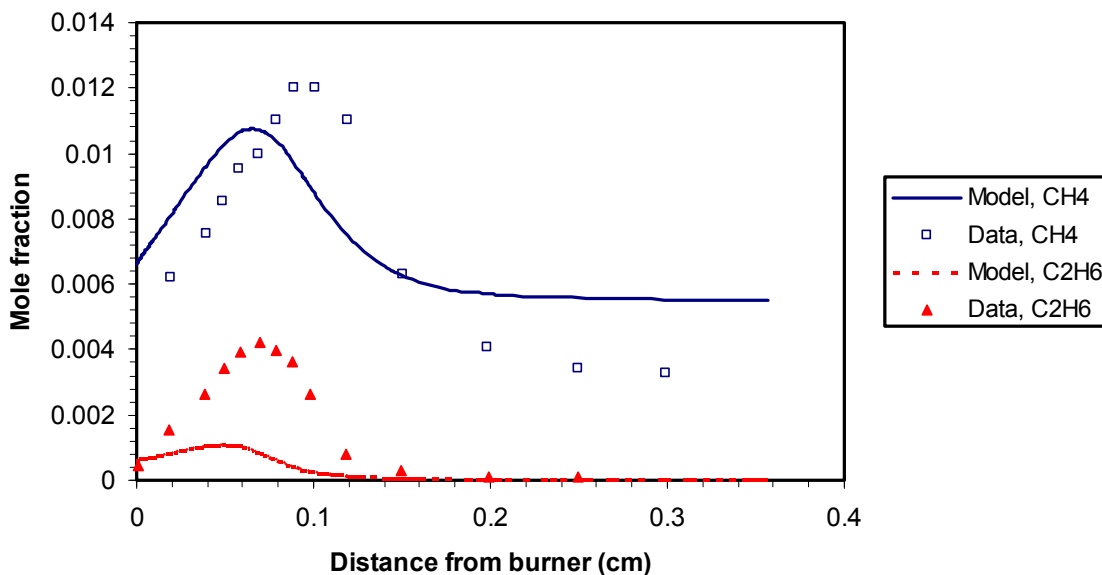

Figure 52.—Comparison of predicted species profiles for a decane/O_2/N_2 burner-stabilized flame with the experimental data of Doute et al. (Ref. 44).
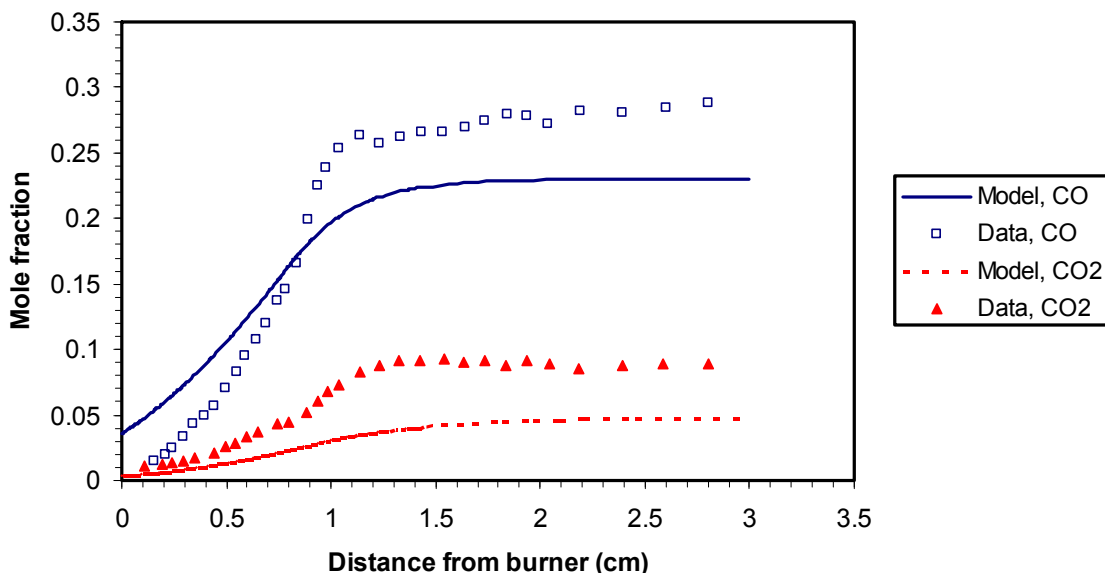
Figure 53.—Comparison of predicted species profiles for a fuel-rich n-decane/O_2/Ar burner-stabilized flame with the experimental data of Delfau et al. (Ref. 43).
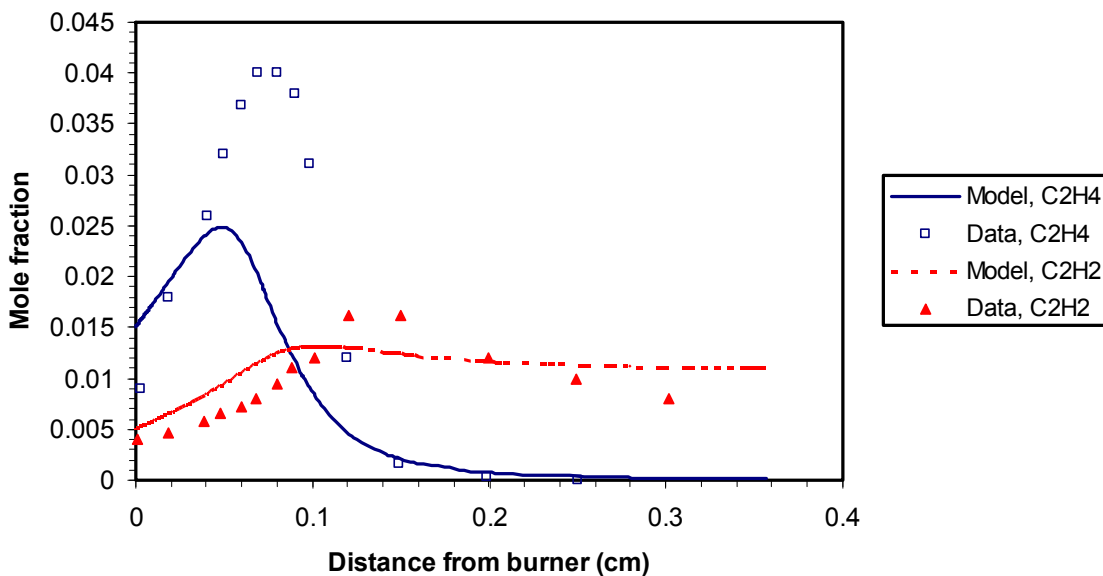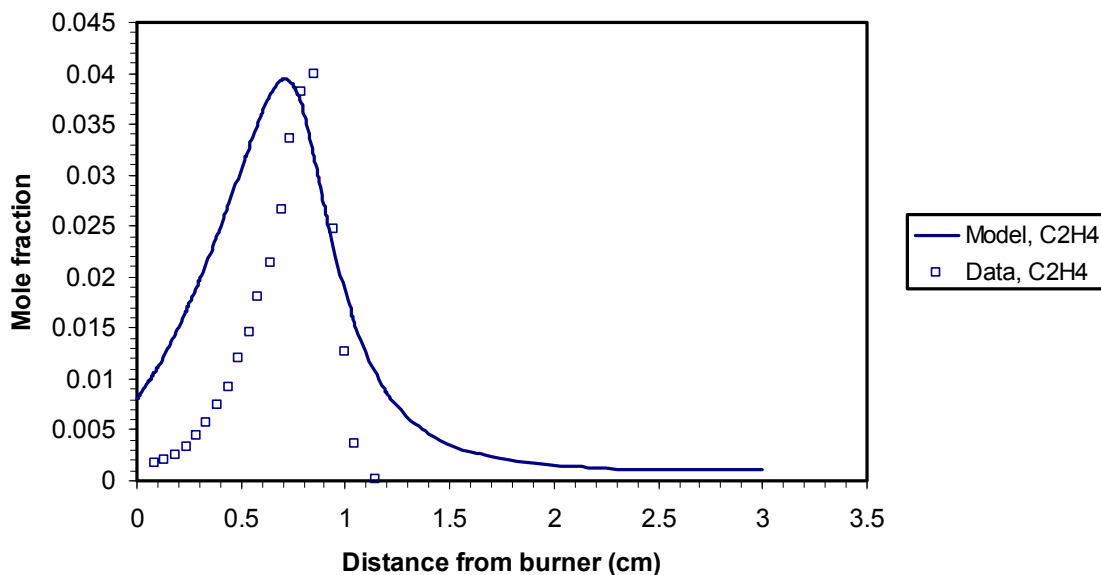
Figure 54.—Comparison of predicted species profiles for a fuel-rich *n*-decane/O₂/Ar burner-stabilized flame with the experimental data of Delfau et al. (Ref. 43).
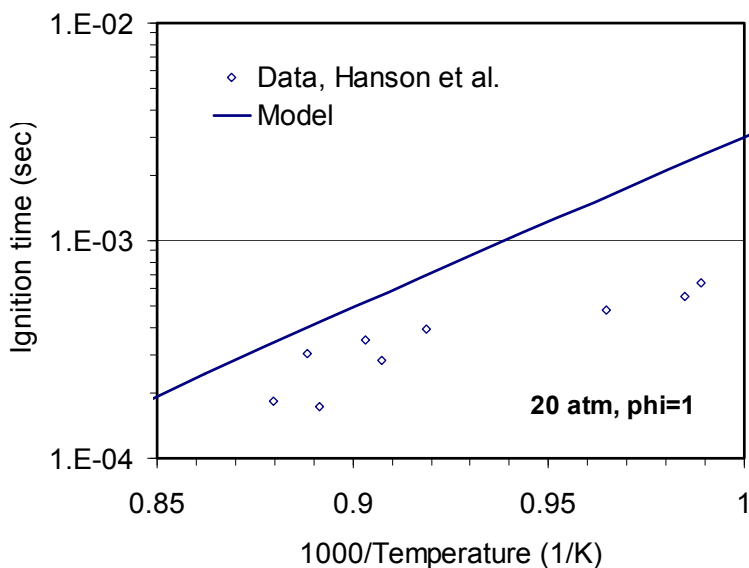
Figure 55.—Calculated *n*-dodecane/air ignition delay times compared with the data of Hanson et al. (Ref. 45). Conditions include pressure of 20 atm and a stoichiometric mixture.

Figure 54 shows the profiles of ethylene. The model predictions for the ethylene profile and its peak value are consistent with the experimental data.

Overall, the model predicts consistent trends of species profiles for both the low-pressure conditions of Delfau et al. and the atmospheric conditions of Doute et al.

3.4.3 *n*-Dodecane—Ignition Times and Laminar Flame Speeds

Figure 55 compares the calculated ignition-delay times with the experimental data of Hanson et al. (Ref. 45) for a stoichiometric *n*-dodecane/air mixture, at a pressure of 20 atm. The predicted ignition time at temperatures above 1100 K are within a factor of two. However, the mechanism could not capture the faster ignition measured near 1000 K. A lack of low-temperature kinetics in the current mechanism is the
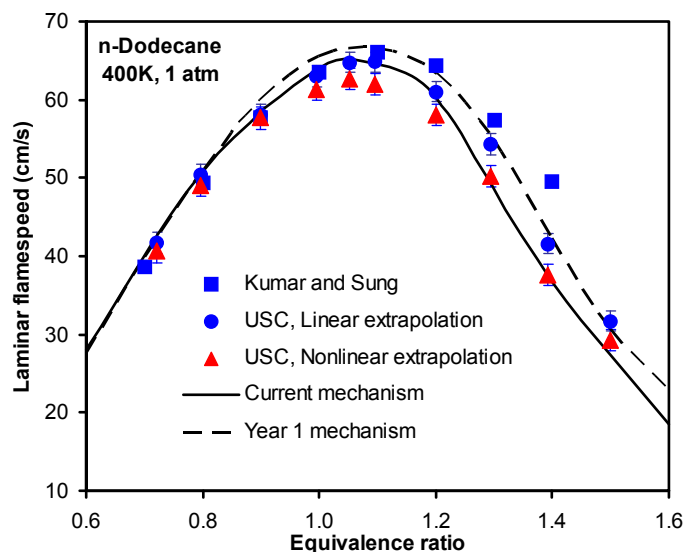
Figure 56.—Comparison of predicted laminar flame speed of
n-dodecane to the experimental data.

reason for this deviation at low temperatures. But for applications to jet engines, high temperature kinetics dominates and low temperature kinetics do not play a significant role. Also, we note that the data from Hanson et al. is preliminary, pre-published data.

Comparison of predicted laminar flame speeds of *n*-dodecane to the experimental data from USC and from the literature is shown in Figure 56. We can see the current mechanism displays improved flame speed predictions for *n*-dodecane components over a range of equivalence ratios.

3.4.4   F-T Fuel Surrogate—Laminar Flame Speeds, Flame-Extinction, and Stirred Reactor Data

With good agreement found from the model comparisons to data for the surrogate-fuel components, the next step was to test the surrogate blend proposed against the F-T fuel data. Here we have used surrogate proposed in Table 7 to test the model against the S-8 and R-8 real-fuel data measured by USC. The CHEMKIN-PRO flame-speed simulations included thermal diffusion, and used mixture-averaged transport properties. Grid-dependency studies were again performed to assure that the grid is sufficiently refined such that further refinement would not affect the flame-speed values predicted. As shown in Figure 57, predictions are in excellent agreement with the data for these alternative fuels. Any discrepancies between the predictions and the data are well within experimental uncertainties. We also note that in simulation trials, different surrogate compositions for both F-T fuels from Tables 7 and 8 give almost the same predicted laminar flame speed as that shown in Figure 57. This suggests that both F-T fuels should have the same flame-propagation behavior despite the differences in carbon number distributions. It also suggests that laminar flame-speed measurements are not sufficiently sensitive to differences in fuel composition when the fuels are mostly normal alkanes greater than ~C_5.

We next modeled extinction strain rates for this F-T surrogate. Since extinction strain rate calculations take more time to solve than flame-speed calculations, and since our kinetic mechanism is large, we first generated a reduced mechanism for the extinction strain rate calculations. The mechanism reduction was performed using methods previously reported, to produce a mechanism that is still accurate over a wide range of equivalence ratios. This was verified by comparing flame-speed predictions. The reduced mechanism consisted of 234 species and 1605 reactions. Since the mechanism reduction was targeted for a range of high-temperature conditions, and since we were conservative in the extent of reduction, we expect the reduced mechanism to perform as well as the full mechanism would for the extinction strain rate calculations.
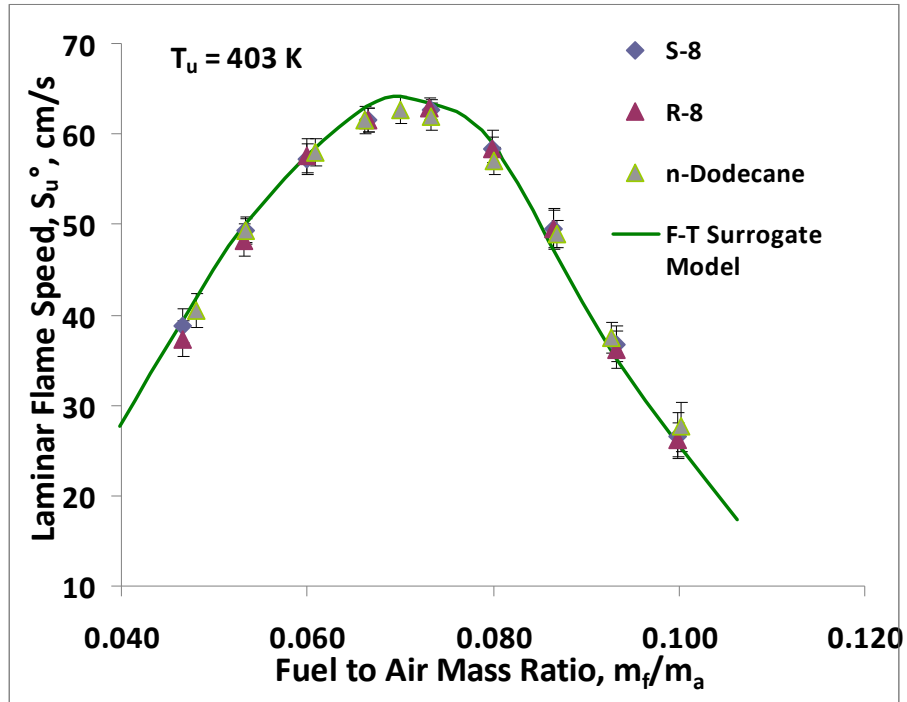
Figure 57.—Comparison of predicted flame speeds for the Shell F-T surrogate with the latest USC experimental data for S-8, R-8, and *n*-dodecane.
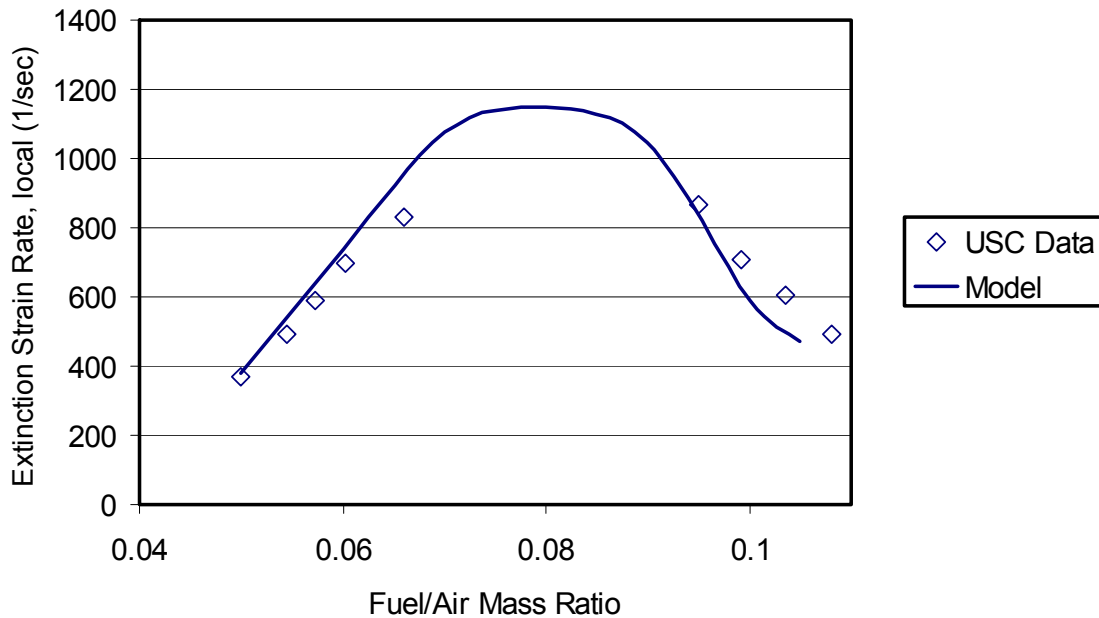
Figure 58.—Comparison of predicted extinction strain rates for the Shell F-T surrogate with the USC experimental data.

Figure 58 shows that the model predictions for extinction strain rates compare well with the USC experimental data, over the range of fuel/air ratios studied. The conditions involved fuel/air mixtures exiting from a nozzle at 403 K, and nitrogen exiting the other nozzle at 296 K. Mixture-averaged transport properties have been used in the simulations, and we included thermal diffusion effects. While the use of multicomponent transport properties is preferable for extinction strain-rate calculations, it is significantly more computationally expensive.

The good agreement between the predictions and the USC experimental data, for both the extinction strain rates and laminar flame speeds, provides confidence in the fuel-component mechanisms and in the surrogate-blending methodology used to determine the surrogate composition.

To supplement the flame experiments, we searched the literature for any available data that can augment our model validation of F-T surrogates. Results from a recent study by Stouffer et al. (Ref. 46) was provided to us by AFRL. They used a well-stirred reactor to study Syntroleum S-8 F-T fuel and measured combustion products, NO_x, and CO in the exhaust. They also studied Lean Blow Off (LBO) but this modeling is beyond the scope of this project. The fuel-air equivalence ratio of the study was from 0.4 to 0.6, which resulted in reactor temperatures of 1300 to 1700 K. Two different flow rates were tested that resulted in residence times ranging from 5 to 12 ms in the reactor. Despite mixing effects and heat losses observed in the reactor, modeling using the Perfectly Stirred Reactor in CHEMKIN-PRO captures the overall trends reasonably well.

We have used the proposed S-8 surrogate (Table 2) for all the CHEMKIN simulations. Measured and predicted well-stirred reactor temperatures are shown in Figure 59. Our initial simulations with adiabatic reactor conditions showed that the measured reactor temperatures are more than 50 K below those predicted by kinetics, or by thermodynamic equilibrium. Uncertainty in measured residence time up to 1 to 2 ms could not account for such a difference in temperature. Therefore, the lower reactor temperature has to be the result of heat losses or imperfect mixing in the experiment. Since it is not possible to account for mixing effects using a PSR model, we have used a fixed heat loss rate of 180 cal/sec (an arbitrary factor to match the temperature at one point) for all simulations. Predicted temperatures with this heat loss then correctly match the measured temperatures as shown in Figure 59. Data and predictions for two different residence times with nominal values of 5.5 and 11 ms are shown in all comparisons. For predictions, the parallel lines represent the differences due to different residence times. Figure 60 shows the comparison of measured and predicted species profiles in the reactor exhaust. Predicted profiles agree well with the data for adiabatic simulations as well as those with heat loss adjustment.
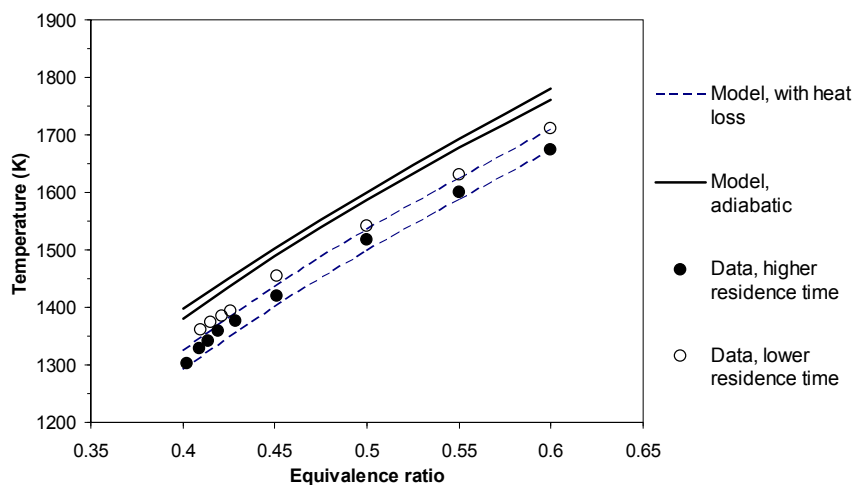
Figure 59.—Comparison of measured well-stirred reactor temperature by Stouffer et al. (Ref. 46) to those predicted.
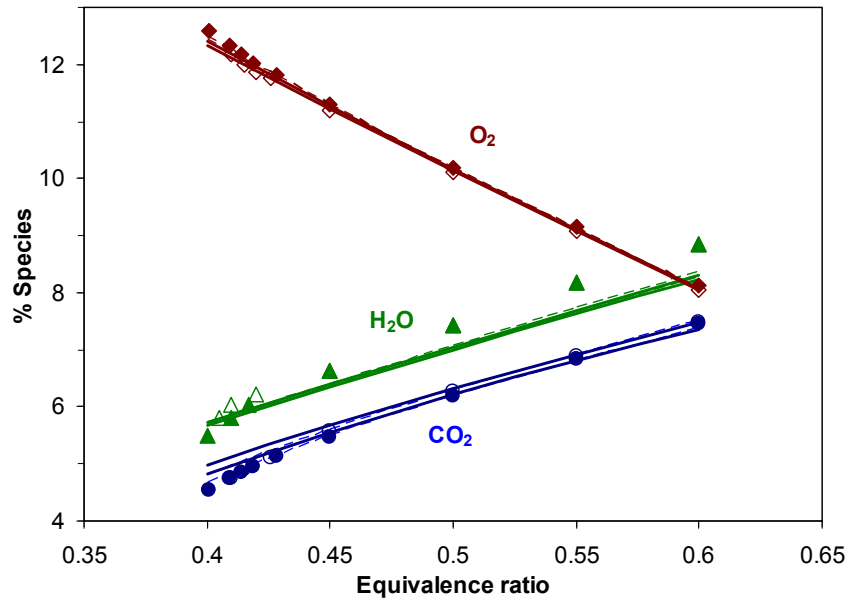
Figure 60.—Comparison of measured species in the well-stirred reactor exhaust by Stouffer et al. (Ref. 46) to those predicted. Dashed lines represent predictions with heat loss in CHEMKIN-PRO model.
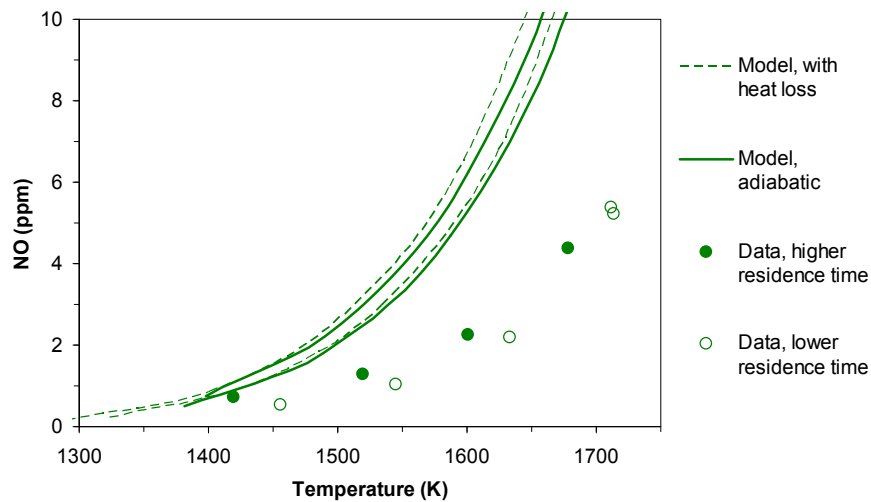
Figure 61.—Comparison of NO levels in the well-stirred reactor exhaust measured by Stouffer et al. (Ref. 46) to those predicted.

Emissions of NO at different temperatures are shown in Figure 61. Predictions capture the onset of NO production but the predicted increase in NO with temperature is more rapid than that observed. This could be due either to the impact of imperfect mixing or merely to the uncertainty in measuring such low levels of NO. The emission indices for CO are shown in Figure 62. The predicted emission index of CO for the high residence time agrees well with the data. However, measurements did not show as significant an impact on NO due to changes in residence time as was predicted. Despite such differences, overall predictions are reasonably good, considering the simplicity of the surrogate for these F-T fuels.
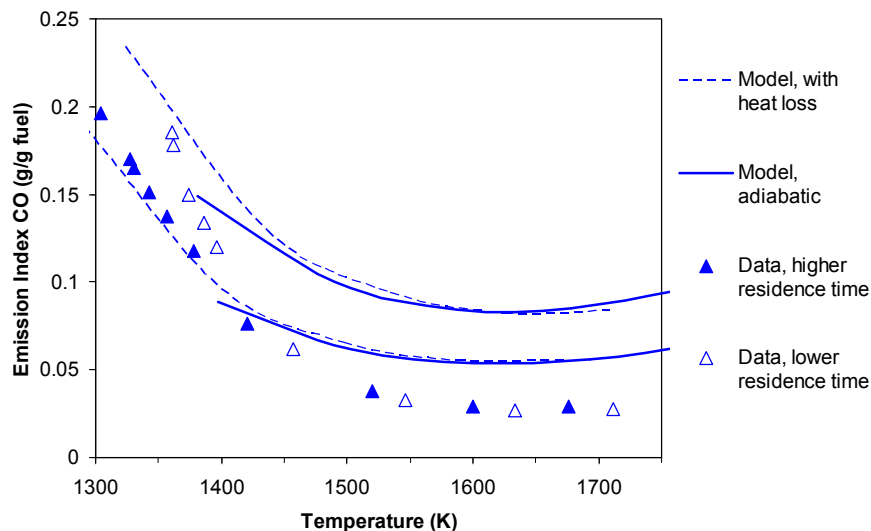
Figure 62.—Comparison of emission index of CO in the well-stirred reactor exhaust measured by Stouffer et al. (Ref. 46) to those predicted.

3.4.5 NOx Predictions

For the NO_x measurements in flames, USC provided data on small alkanes as well as for the heavier hydrocarbon fuels. This allowed us to first test the model's predictive capabilities against data where experimental uncertainties were smaller. It is expected that the core mechanism controlling NO_x production is the same for all of the hydrocarbon species, with small differences due to the alkane size or branching, but this is something that we wanted to test and confirm systematically.

Predicted NO_x from *n*-pentane/air flame is shown in Figure 63. Experimental data were obtained by USC using the counter-flow burner assembly with fuel/air from the bottom burner at elevated temperature to vaporize the mixture and nitrogen from the top burner at room temperature. The burner separation distance was 1.4 cm and the equivalence ratio used was 0.8. As seen in the figure, predictions and measured NO_x are in excellent agreement. Based on the model, we found that most NO_x is in the form of NO.

Comparisons of predicted and measured NO_x for *n*-decane/air and *n*-dodecane/air flames are shown in Figure 64. Note that the fuel/air mixture temperature and strain rate for these flames are higher than for the *n*-pentane/air flame shown in Figure 63, which contributes to the higher overall NO_x levels. The measured NO_x peak is around 30 ppmd (ppm on dry basis) for both *n*-decane and *n*-dodecane flames. The model under-predicts the peak NO_x by 4 ppmd for *n*-decane and by 7 ppmd for *n*-dodecane. In further analysis, however, we found that the chemical pathways for NO_x productions in *n*-dodecane and *n*-pentane flames are similar, which led us to question whether the higher measured values were reliable.

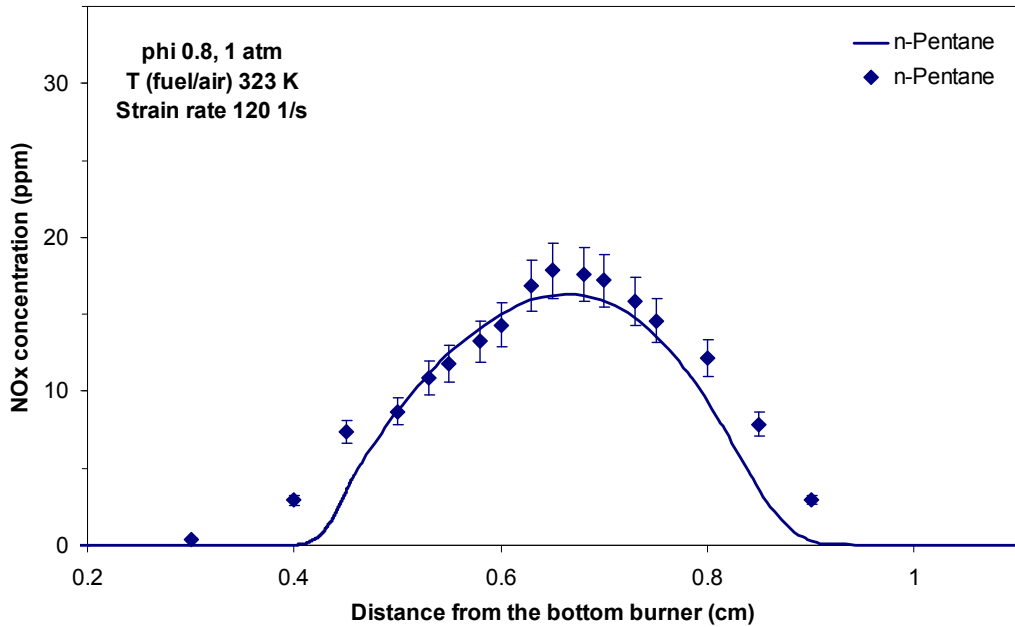Figure 63.—Comparison of predicted and measured NO$_x$ levels for *n*-pentane/air flame. Symbols represent experimental data and lines represent model predictions.
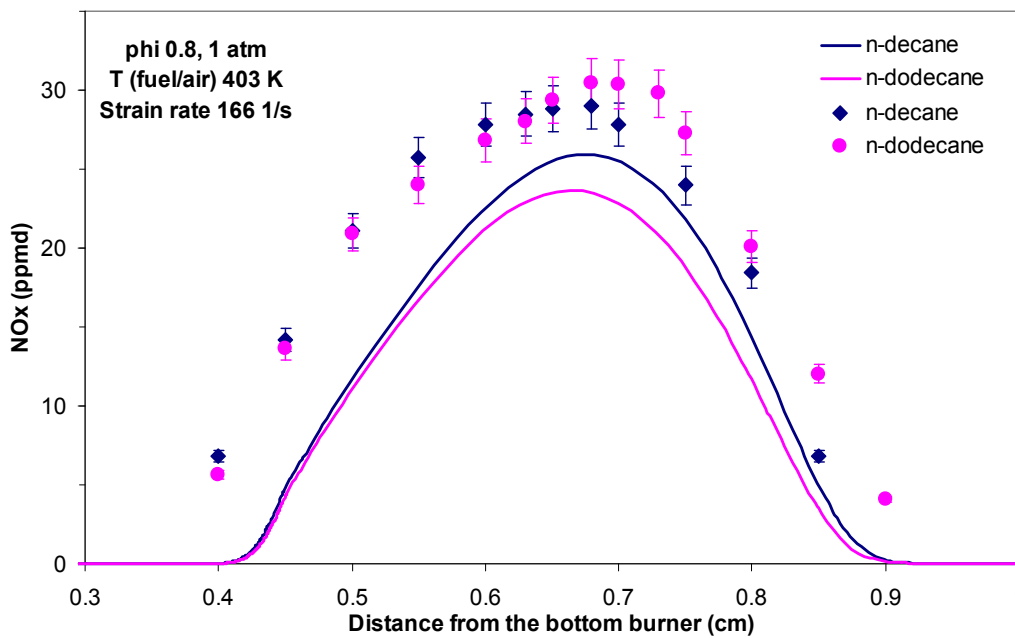

Figure 64.—Comparison of predicted and measured NO$_x$ levels for *n*-decane/air and *n*-dodecane/air flames. Symbols represent experimental data and lines represent model predictions.
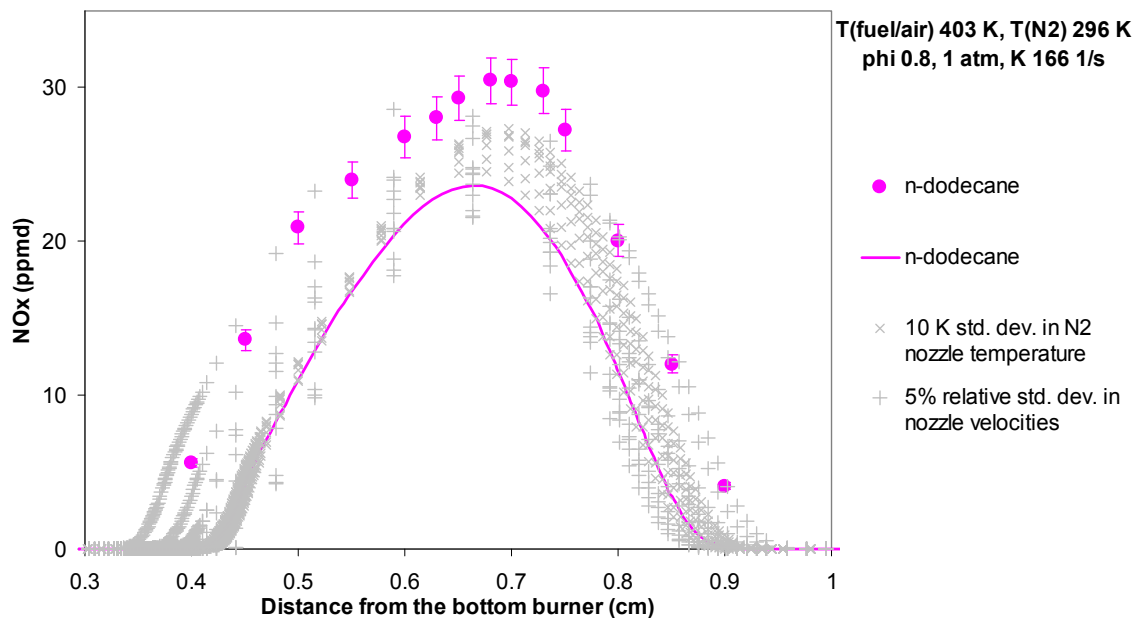
Figure 65.—Impact of uncertainty in nozzle velocities and nitrogen burner (top burner) temperature on NO$_x$ predictions for *n*-dodecane/air flames. Gray symbols represent predictions from Uncertainty Analyses in CHEMKIN-PRO. Filled circles are the experimental data.

In order to estimate the impact of the uncertainty of various experimental parameters on NO$_x$, we performed an uncertainty analysis on (1) burner velocities and (2) nitrogen nozzle temperatures. Uncertainty in fuel/air burner temperature was not considered for the uncertainty analysis, since that burner is heated and maintained at a specified temperature, whereas the temperature of the nitrogen burner was not controlled. The Uncertainty Analysis feature in CHEMKIN-PRO was used for the simulations. As shown in Figure 65, a 5 percent relative standard deviation in nozzle velocities can change the peak NO$_x$ level by 7 ppmd. Uncertainty in the nitrogen burner temperature can also significantly affect the NO$_x$ levels at distances closer to that burner. Considering the impact of these experimental uncertainties on NO$_x$ levels, we concluded from this that the model predictions for *n*-decane and *n*-dodecane should be considered to be good, or within the range of experimental accuracy possible.

3.4.6 Prediction of Autoignition Temperature

To augment the USC flame data in providing a broader test of the surrogate-fuel mechanisms, we investigated the availability of ignition data that may better differentiate different surrogate-fuel components. Recently, Bieleveld et al. (Ref. 47) measured autoignition temperature of various fuels in a counter-flow burner assembly as shown in Figure 66. They increased the temperature of air until the fuel auto-ignites. Measured autoignition temperatures of *n*-heptane and *iso*-octane as a function of strain rates for a fixed fuel mass fraction of 0.4 are reported and reproduced in Figure 67. Simulations of these experiments have been performed using the CHEMKIN-PRO Opposed-flow Flame model (Ref. 1), by gradually increasing the temperature of air. Comparison of predicted and measured autoignition temperatures are shown in Figure 67. As shown in the figure, the model captures the autoignition temperatures of *n*-heptane and *iso*-octane very well.

To predict the autoignition behavior of F-T fuels, we performed simulations using the 3-component surrogate for S-8 fuel (*n*-dodecane/*n*-decane/*iso*-octane: 38/34/28 mol%). As shown in Figure 67, autoignition temperatures for F-T fuels are closer to those of *iso*-octane at lower strain rates and shift towards those of *n*-heptane at higher strain rates.
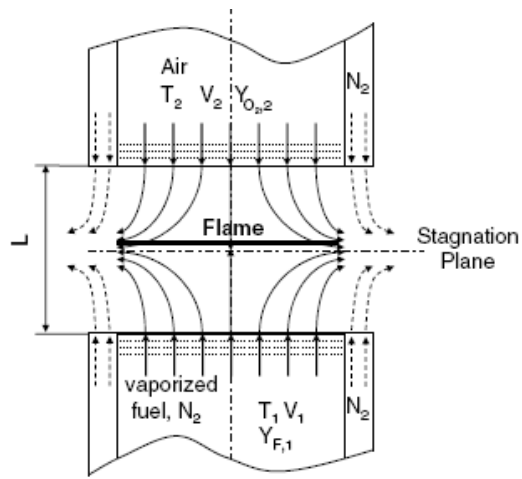
Figure 66.—Schematic illustration of the counterflow
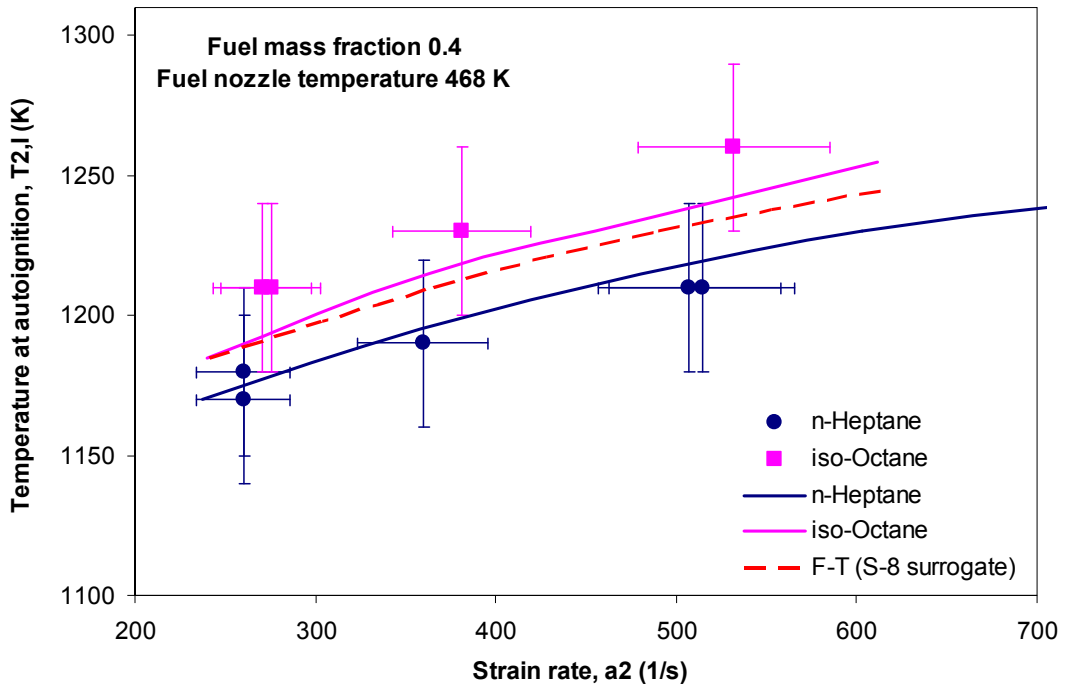burner assembly of Bieleveld et al. (Ref. 47).

Figure 67.—Comparison of predicted and measured autoignition temperatures for various fuels.
Symbols represent experimental data from Bieleveld et al. (Ref. 47) and lines represent predictions.

3.4.7 Prediction of Gas-Phase PAH Species

Many researchers have performed PAH and soot measurements for burner-stabilized flames of various smaller hydrocarbon fuels. In order to validate the PAH and soot-growth mechanism recently incorporated into the F-T fuel-surrogate mechanism, we started by performing flame simulations for core fuel components (C_3 and smaller). During this quarter, we used two sets of experimental data for simulation under sooting flame conditions with an equivalence ratio of 2.5 at 1 atm: (1) Senkan and Castaldi (Ref. 48) propane/O_2 flame diluted with 45.1% Ar, and (2) Wang et al. (Ref. 49) ethylene/O_2 flame diluted with 68.9% Ar. Senkan and Castaldi measured profiles of various product species but did not measure soot. Wang et al. did not report the measured PAH species profiles but reported the measured particle density, diameter, and volume fraction. The CHEMKIN-PRO Burner-Stabilized Premixed-Flame model (Ref. 1) was used for simulations, with the measured temperature profile as a fixed-temperature constraint on the simulations.

Comparisons of various species predicted and measured by Senkan and Castaldi are shown in Figures 68 to 71. Major products acetylene (C_2H_2) and benzene (C_6H_6) are predicted reasonably well. Propyne-propadiene (C_3H_4) and butadiene (C_4H_2) are slightly underpredicted. Trends in PAH species naphthalene, phenanthrene, and pyrene are captured by the model, but the predicted levels were more than an order of magnitude lower than those observed between 4 to 16 ppm. Underprediction of these soot precursors will potentially result in underprediction of soot particles. This suggests that there is more work needed to extend and refine the reaction paths involved in PAH-formation, before meaningful refinement of the soot-particle growth models can be achieved.

Figure 68.—Comparison of predicted and measured acetylene profile by Senkan and Castaldi (Ref. 48) for a burner stabilized propane flame. Symbols represent experimental data and lines represent predictions.
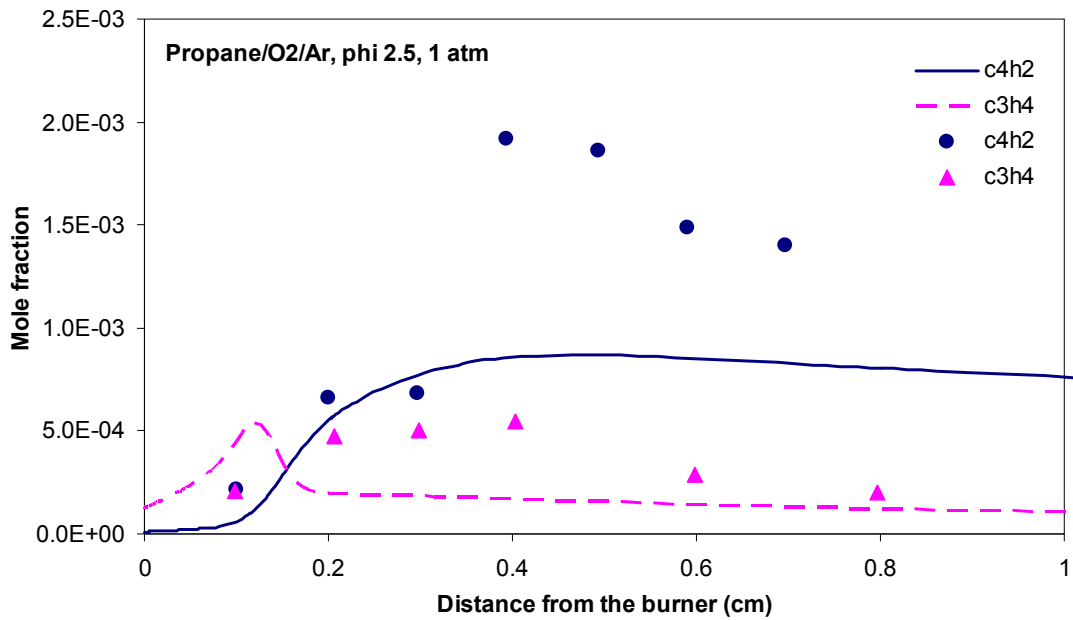
Figure 69.—Comparison of predicted and measured propyne-propadiene (C_3H_4) and butadiene (C_4H_2) profile by Senkan and Castaldi (Ref. 48) for a burner stabilized propane flame. Symbols represent experimental data and lines represent predictions.
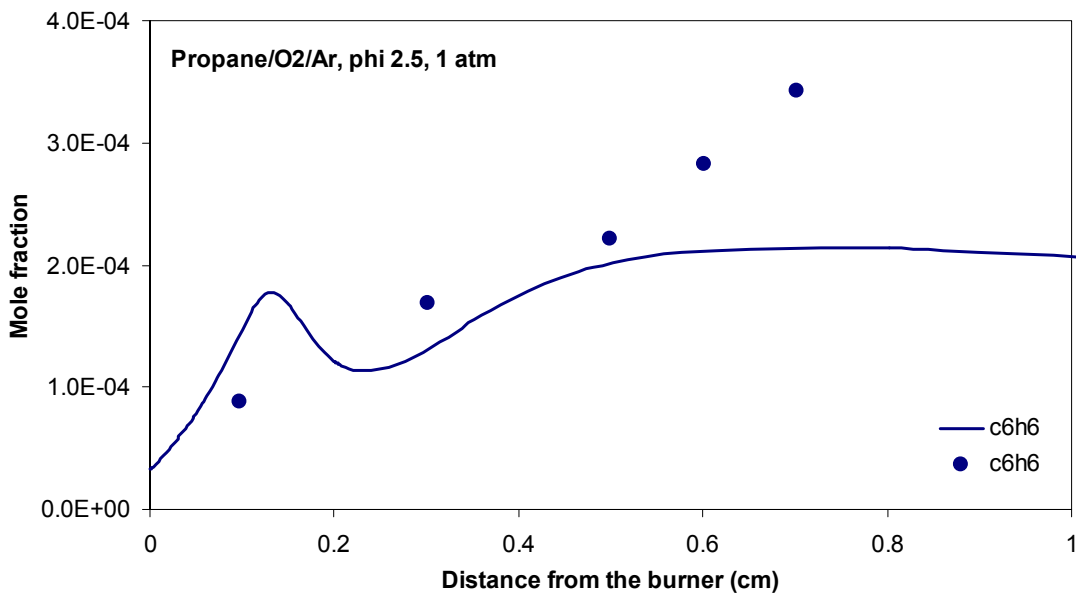
Figure 70.—Comparison of predicted and measured benzene profile by Senkan and Castaldi (Ref. 48) for a burner stabilized propane flame. Symbols represent experimental data and lines represent predictions.
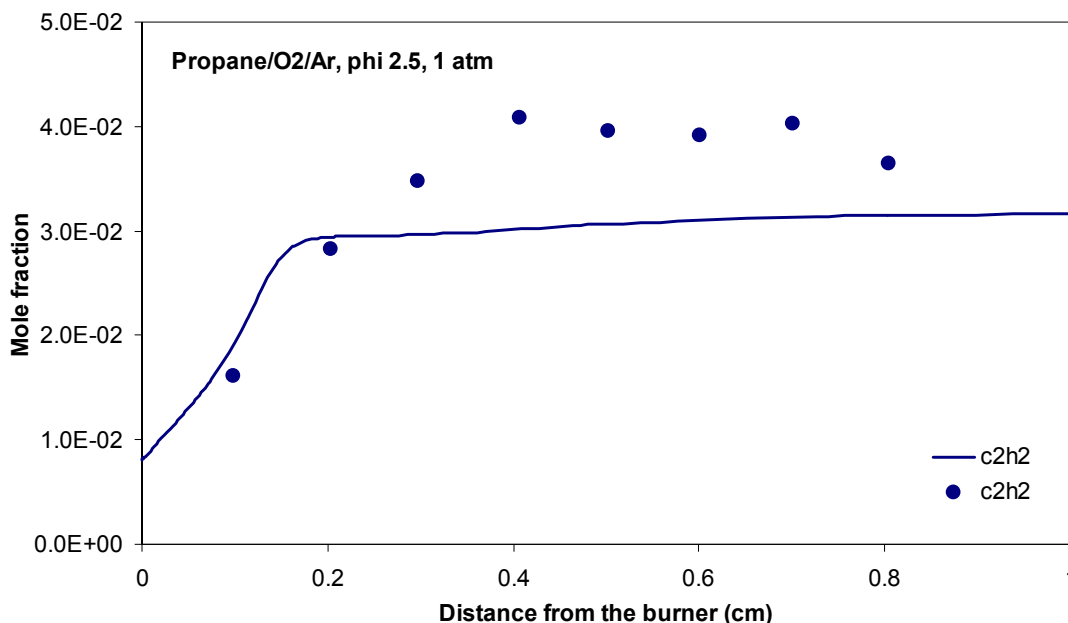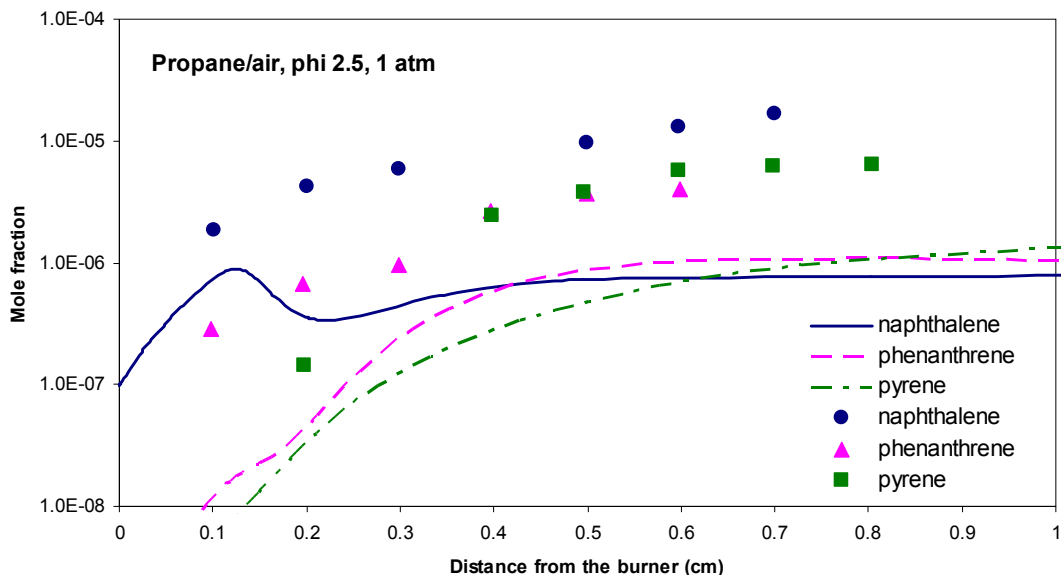
Figure 71.—Comparison of predicted and measured PAH species profiles by Senkan and Castaldi (Ref. 48) for a burner stabilized propane flame. Symbols represent experimental data and lines represent predictions.
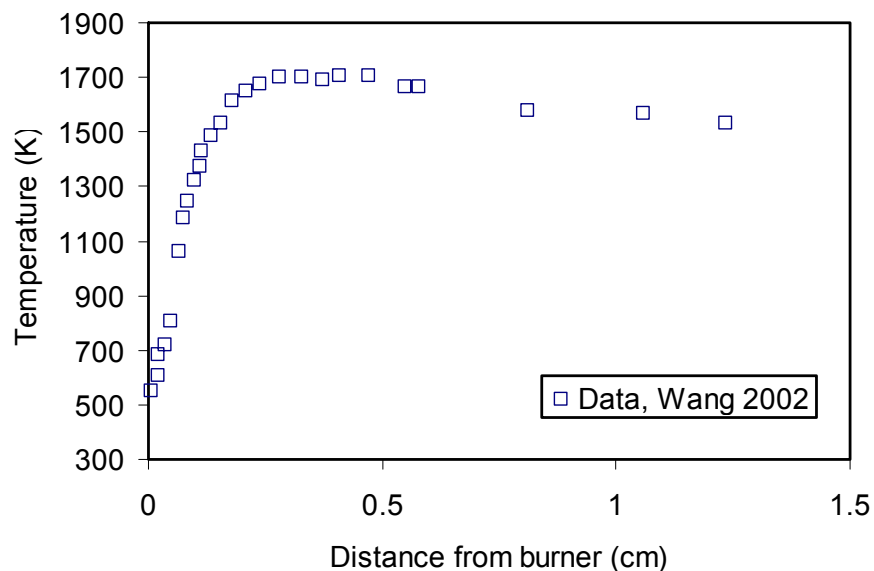
Figure 72.—Temperature profile of Wang et al. (Ref. 49) used in current simulation. Conditions include atmospheric pressure, inlet velocity of 7.8 cm/sec and an equivalence ratio of 2.5 (mole fractions: C_2H_4- 0.141, O_2- 0.170, Ar- 0.689).

3.4.8 Soot-Particle Growth Predictions

To test both the PAH sub-mechanism and the soot-particle growth mechanism, we also performed some validation studies against soot measurements in the literature. During this quarter, we used the experimental data of Wang et al. (Ref. 49), under sooting flame conditions. Wang et al. (Ref. 49) studied soot in burner-stabilized premixed flames of fuel-rich ethylene/O_2/Ar at atmospheric conditions. The equivalence ratio was 2.5, and the inlet velocity was 7.8 cm/sec. They reported their temperature profile; this profile, shown in Figure 72, has been used in our simulations.

Figure 73.—Comparison of calculated particle volume fraction with the data of Wang et al. (Ref. 49). Conditions include atmospheric pressure, inlet velocity of 7.8 cm/sec and an equivalence ratio of 2.5 (mole fractions: C_2H_4- 0.141, O_2- 0.170, Ar- 0.689).

Wang et al. studied soot development using small-angle neutron scattering (SANS) (Ref. 49). They could characterize and quantify particles of sizes in the 1 to 100 nm size range in flames using this technique. They reported that the soot contained only carbon and hydrogen with a carbon-to-hydrogen ratio of 5.5±0.1, a value consistent with the ratio for mature soot particles measured in similar ethylene flames. The soot-growth mechanism includes the surface reactions that describe the HACA-soot growth mechanism of Appel et al. and the newly added PAH-condensation on the soot-particle surface.

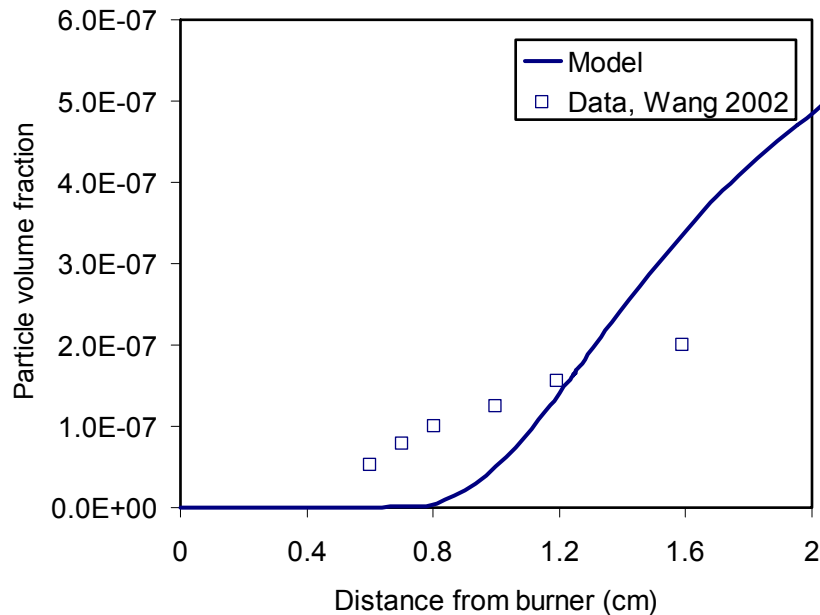Figure 73 compared the calculated particle volume fraction with the experimental data of Wang et al. The model shows the soot forming at a slightly more distant location from the burner surface than the data, but the trends exhibited by the model are consistent with the experimental data.

Figure 74 compares the calculated particle number density with the experimental data of Wang et al. Both the model and the data show the number density on the order of $\sim10^{11}$, with the model under-predicting by about a factor of two. The experimental number density reported is for particles with radius greater than or equal to 4 nm. Regarding experimental uncertainties, Wang et al. noted that a worst case of uncertainties might result in the number density values increasing by a factor of three.

The modeling results show particle number density increasing as a function of distance until ~1.2 cm, and subsequently the number density decreases. Factors contributing to this behavior include the decrease in particle number due to coagulation, and the increase in particle number due to nucleation and growth of new particles. Until 1.2 cm, the formation of new particles is more than the decrease in particle number due to coagulation, and the particle number density increases. Figure 73 shows the particle volume fraction continuously increasing as a function of distance. This, in combination with the results shown in Figure 74, indicates that increase in soot volume fraction as a function of distance at locations far away from the burner is primarily due to increases in particle size.

Figure 75 compares the calculated average particle diameter with the experimental data of Wang et al. The experimental data shows a fairly tight range for the particle diameters, and the model is not able to capture that effect. These results show that the models are "in the right ball-park" but will need refinement to be quantitatively predictive. The starting point should be to improve the formation pathways for soot precursors and the second step will be to then refine the nucleation and soot-growth as well as oxidation descriptions. While such a project is beyond the scope of this work, these tests provide a good understanding of the baseline capability with our current surrogate-fuel mechanisms.

Figure 74.—Comparison of calculated particle number density with the data of Wang et al. (Ref. 49). Conditions include atmospheric pressure, inlet velocity of 7.8 cm/sec and an equivalence ratio of 2.5 (mole fractions: C_2H_4- 0.141, O_2- 0.170, Ar- 0.689).
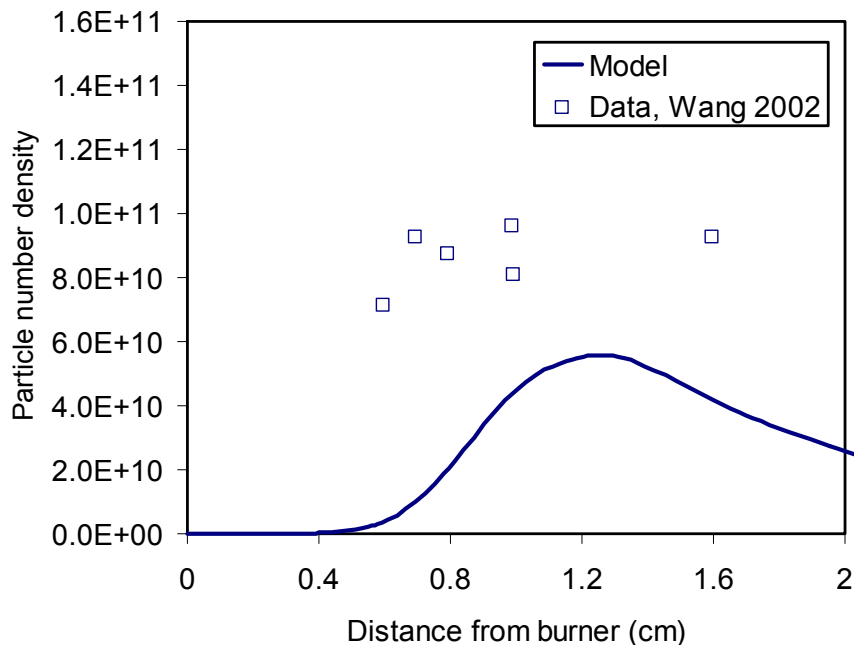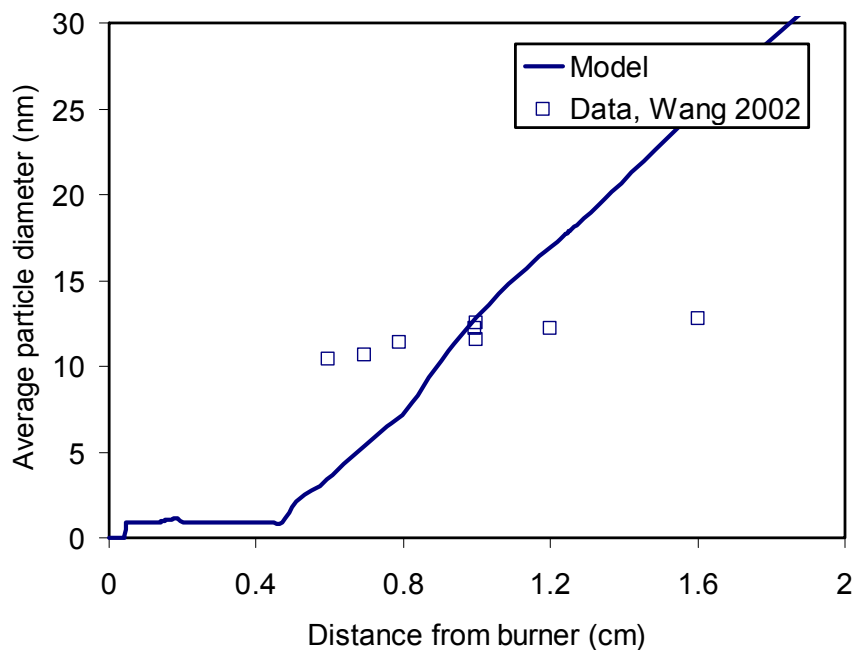

Figure 75.—Comparison of calculated average particle diameter with the data of Wang et al. (Ref. 49). Conditions include atmospheric pressure, inlet velocity of 7.8 cm/sec and an equivalence ratio of 2.5 (mole fractions: C_2H_4- 0.141, O_2- 0.170, Ar- 0.689).

4.0   Conclusions

This project combined state-of-the-art experimental investigation of heavy (liquid) hydrocarbon fuels in flame experiments with state-of-the-art kinetics and numerical modeling. While results include improvements to both the models and the experimental methods, the important outcome is a deeper understanding of the similarities and differences in combustion behavior of different conventional and alternative jet fuels.

In comparing F-T fuels to bio-derived jet fuels, we find almost no discernable difference in the combustion behavior, based on the limited samples available for the bio-derived jet fuel. This is largely due to the strict jet-fuel standard that both alternative fuels must meet, but also due to the chemical nature of the process used to produce the bio-derived fuel. Fuel derived from plant oils are typically in the form of long-chain methyl esters. To meet the jet-fuel requirements, these are further processed (through hydrogenation) to remove the oxygen from the oxygenate compounds. This processing results in a dominant composition of long-chain alkane molecules, very similar to what the chemical analysis showed for F-T jet fuels.

Similarly, despite significant differences in the carbon-number distribution for two different F-T fuels, the combustion behavior measured appears to be identical. This can be explained by the very similar combustion behavior observed for different long-chain alkane molecules that have chain length greater than ~6. In this way, different distributions of alkane chain length do not have a significant effect on flame propagation or flame extinction, although they might affect the quantitative degree of NO_x production. Furthermore, though branched alkanes are prevalent in the F-T fuels, these tend to have very low branching, such that normal-alkane behaviore tends to dominate the F-T fuel combustion.

In experimentally comparing the alternative fuels with JP-7 and JP-8, we find that the alternative fuels have almost the same flame-propagation speed as JP-7 and that the flame-speed for JP-7 is slightly faster than for JP-8. This is consistent with JP-8 fuel containing more aromatic compounds than JP-7 (or than the F-T and bio-derived fuels), which tends to lower the flame speed. For flame-extinction measurements, a similar trend is apparent, although the difference in extinction between JP-7 and JP-8 is smaller in that case and close to experimental uncertainty for those measurements.

In comparing the flame-propagation and flame-extinction behavior of the normal alkane, n-dodecane, which matches the typical average carbon number of an F-T fuel, with the same measurements for the alternative and conventional jet fuels, we find that *n*-dodecane has about the same laminar flame speed and slightly higher resistance to extinction. This makes *n*-dodecane a reasonable single-component surrogate for all of these fuels under flame-simulation conditions. However, a multicomponent surrogate blend is needed to match other fuel properties, such as cetane number or sooting propensity.

Laminar flame-speed, flame-extinction strain rate, ignition time, auto-ignition temperature, NO_x and other species-concentration measurements are well predicted by the chemistry models developed for n-alkane/iso-alkane surrogate blends. In most cases, predictions are within experimental uncertainty of the data. The mechanisms underwent significant improvement during the project. The only area where the mechanisms provide mixed results is for PAH and soot predictions. Systematic improvement of these sub-mechanisms was beyond the scope of this project, although the results provide a good baseline for such an undertaking.

We have recommended surrogate blends for F-T blends that consist of mixtures of n-dodecane, *n*-decane, and *iso*-octane. In addition, we have described a systematic approach to generating a specific blend to match a specific fuel. Compositions for specific surrogates of two different F-T fuels have been proposed that provide a best match to cetane number, H/C ratio, lower heating value, T50 boiling point, and chemical-analysis data. Tests of these blends against experimental data for flame-propagation and flame-extinction strain rate show good agreement.

A successful reduction of the high-temperature F-T surrogate mechanism has been achieved that provides a ~90 percent reduction in the number of species without significant loss of accuracy in flame-speed predictions for a range equivalence ratios. The mechanism was reduced using a combination of

Directed Relation Graph and Computational Singular Perturbation mechanism-reduction methods, applied to a range of conditions. The results are verified against the full "master" mechanism that was independently validated in the experiment/model comparisons.

References

1. CHEMKIN-PRO Release 15081, Reaction Design, San Diego, CA, 2008.
2. Lu, T.; Law, C.K. "A directed relation graph method for mechanism reduction," *Proceedings of the Combustion Institute* 2005, 30, 1333–1341.
3. Lu, T.; Law, C.K. "Linear time reduction of large kinetic mechanisms with directed relation graph: n-heptane and iso-octane," *Combustion and Flame* 2006, 144, 24–36.
4. Wang, H.; Du, D.X.; Sung, C.J.; Law, C.K. "Experiments and Numerical Simulation on Soot Formation in Opposed-Jet Ethylene Diffusion Flames," *Proceedings of the Combustion Institute* 1996, 26, 2359–2368.
5. Fotache, C.G.; Kreutz, T.G.; Zhu, D.L.; Law, C.K. "An experimental study of ignition in nonpremixed counterflowing hydrogen versus heated air," *Combustion Science and Technology* 1995, 109, 373–393.
6. Westbrook, C.K.; Pitz, W.; Herbinet, O.; Curran, H.J.; Silke, E.J. "A Detailed Chemical Kinetic Reaction Mechanism for Combustion of n-Alkanes from n-Octane to n-Hexadecane," *Combustion and Flame* 2009, 156, 181–191.
7. Curran, H.J.; Gaffuri, P.; Pitz, W.J.; Westbrook, C.K. "A Comprehensive Modeling Study of Iso-Octane Oxidation," *Combustion and Flame* 2002, 129, 253–280.
8. Curran, H.J.; Gaffuri, P.; Pitz, W.J.; Westbrook, C.K. "A Comprehensive Modeling Study of n-Heptane Oxidation," *Combustion and Flame* 1998, 114, 149–177.
9. Ji, C.; You, X.; Holley, A.T.; Wang, Y.L.; Egolfopoulos, F.N.; Wang, H. "Propagation and Extinction of Premixed n-Dodecane/Air Flames," 32nd International Symposium on Combustion, Montreal, Canada, 2008.
10. Lengyel, I.; Naik, C.V.; Puduppakkam, K.; Meeks, E. "Automatic Generation of Model-fuel Mechanisms for Use in Engine Combustion Simulation," 235th ACS National Meeting, New Orleans, 2008.
11. Wang, H.; You, X.; Joshi, A.V.; Davis, S.G.; Laskin, A.; Egolfopoulos, F.; Law, C.K. *USC Mech Version II. High-Temperature Combustion Reaction Model of H2/CO/C1-C4 Compounds*, http://ignis.usc.edu/USC_Mech_II.htm, 2007.
12. NIST *Chemical Kinetics Database*, http://kinetics.nist.gov/kinetics/, NIST.
13. Vagelopoulos, C.M.; Egolfopoulos, F.N. "Direct experimental determination of laminar flame speeds," Twenty-seventh Symposium (International) on Combustion, 1998; p. 513.
14. Davis, S.G.; Law, C.K. "Laminar flame speeds and oxidation kinetics of iso-octane-air and n-heptane-air flames," 27th Symposium (International) on Combustion, 1998; pp. 521–527.
15. Kumar, K.; Freeh, J.E.; Sung, C.J.; Huang, Y. "Laminar flame speeds of preheated iso-octane/O_2/N_2 and n-heptane/O_2/N_2 mixtures," *Journal of Propulsion and Power* 2007, 23, 430.
16. Smith, G.P.; Golden, D.M.; Frenklach, M.; Moriarty, N.W.; Eiteneer, B.; Goldenberg, M.; Bowman, C.T.; Hanson, R.K.; Song, S.; Gandiner, W.C., Jr.; Lissianski, V.V.; Qin, Z. *GRI-Mech Home Page*, http://www.me.berkeley.edu/gri_mech/.
17. Dagaut, P.; Glarborg, P.; Alzueta, M. U. "The Oxidation of Hydrogen Cyanide and Related Chemistry," *Progress in Energy and Combustion Science* 2008, 34, 1–46.
18. Rasmussen, C.L.; Rasmussen, A.E.; Glarborg, P. "Sensitizing effects of NOx on CH4 oxidation at high pressure," *Combustion and Flame* 2008, in press.
19. Sivaramakrishnan, R.; Brezinsky, K.; Dayma, G.; Dagaut, P. "High pressure effects on the mutual sensitization of the oxidation of NO and CH_4–C_2H_6 blends," *Phys. Chem. Chem. Phys.* 2007, **9**, 4230–4244.
20. Dagaut, P.; Daly, C.; Simmie, J.M.; Cathonnet, M. "The oxidation and ignition of dimethylether from low to high temperature (500-1600 K): Experiments and kinetic modeling," 27th Symposium (International) on Combustion, 1998; pp. 361–369.

21. Mueller, M.A.; Yetter, R.A.; Dryer, F.L. "Kinetic Modeling of the $CO/H_2O/O_2/NO/SO_2$ System: Implications for High-Pressure Fall-off in the $SO_2 + O(+M) = SO_3(+M)$ Reaction," *Int. J. Chem. Kinet.* 2000, 32, 317–339.
22. Hori, M.; Marinov, N.; Matsunaga, N.; Pitz, W.; Westbrook, C. "An Experimental and Kinetic Calculation of the Promotion Effect of Hydrocarbons on the," Twenty-Seventh Symposium (International) on Combustion, United States, 1998; p Size: 1.7 Mbytes.
23. Konnov, A.A. *Detailed Reaction Mechanism for Small Hydrocarbons Combustion Release 0.5*, http://homepages.vub.ac.be/~akonnov/, 2000.
24. Glarborg, P.; Alzueta, M.U.; Dam-Johansen, K.; Miller, J.A. "Kinetic Modeling of Hydrocarbon/Nitric Oxide Interactions in a Flow Reactor," *Combustion and Flame* 1998, 115, 1–27.
25. Frenklach, M.; Warnatz, J. "Detailed Modeling of PAH Profiles in a Sooting Low-Pressure Acetylene Flame," *Combustion Science and Technology* 1987, 51, 265–283.
26. Frenklach, M.; Wang, H. "Detailed Modeling of Soot Particle Nucleation and Growth," *Proceedings of the Combustion Institute* 1990, 23, 1559–1566.
27. Wang, H.; Frenklach, M. "A detailed kinetic modeling study of aromatic formation in laminar premixed acetylene and ethylene flames," *Combustion and Flame* 1997, 110, 173.
28. Appel, J.; Bockhorn, H.; Frenklach, M. "Kinetic Modeling of Soot Formation with Detailed Chemistry and Physics: Laminar Premixed Flames of C_2 Hydrocarbons," *Combustion and Flame* 2000, 121, 122–136.
29. Skjøth-Rasmussen, M.S.; Glarborg, P.; Østberg, M.; Johannessen, J.T.; Livbjerg, H.; Jensen, A.D.; Christensen, T.S. "Formation of polycyclic aromatic hydrocarbons and soot in fuel-rich oxidation of methane in a laminar flow reactor," *Combustion and Flame* 2004, 136, 91–128.
30. Richter, H.; Granata, S.; Green, W.H.; Howard, J.B. "Detailed modeling of PAH and soot formation in a laminar premixed benzene/oxygen/argon low-pressure flame," *Proc. Comb. Inst.* 2005, 30, 1397–1405.
31. Zhang, H.R.; Eddings, E.G.; Sarofim, A.F.; Westbrook, C.K. "Fuel Dependence of Benzene Pathways," *Proc. Comb. Inst.* 2009, 32.
32. Vajda, S.; Valko, P.; Turanyi, T. "Principle component analysis of kinetic models," *International Journal of Chemical Kinetics* 1985, 17, 55–81.
33. Lam, S.H. "Using CSP to understand complex chemical kinetics," *Combustion Science and Technology* 1993, 89, 375.
34. Lam, S.H.; Goussis, D.A. "The CSP method for simplifying kinetics," *International Journal of Chemical Kinetics* 1994, 26, 461–486.
35. Massias, A.; Diamantis, D.; Mastorakos, E.; Goussis, D.A. "An algorithm for the construction of global reduced mechanisms with CSP data," *Combustion and Flame* 1999, 117, 685–708.
36. Davidson, D.F.; Oehlschlaeger, M.A.; Herbon, J.T.; Hanson, R.K. "Shock tube measurements of iso-octane ignition times and OH concentration time histories," *Proceedings of the Combustion Institute* 2002, 29, 1295–1301.
37. Vermeer, D.J.; Meyer, J.W.; Oppenheim, A.K. "Auto-ignition of hydrocarbons behind reflected shock waves," *Combustion and Flame* 1972, 18, 327–336.
38. Huang, Y.; Sung, C.J.; Eng, J.A. "Laminar flame speeds of primary reference fuels and reformer gas mixtures," *Combustion and Flame* 2004, 139, 239–251.
39. Kwon, O.C.; Hassan, M.I.; Faeth, G.M. "Flame/stretch interactions of premixed fuel-vapor/O_2/N_2 flames," *Journal of Propulsion and Power* 2000, 16, 513–522.
40. Zhukov, V.P.; Sechenov, V.A.; Starikovskii, A.Y. "Autoignition of n-decane at high pressure," *Comb. Flame* 2008, 153, 130–136.
41. Pfahl, U.; Fieweger, K.; Adomeit, G. "Self-ignition of diesel-relevant hydrocarbon-air mixtures under engine conditions," 26th Symposium (International) on Combustion, 1996; pp. 781–789.
42. Kumar, K.; Sung, C.-J. "Laminar Flame Speeds and Extinction Limits of Preheated n-Decane/O_2/N_2 and n-Dodecane/O_2/N_2 Mixtures," *Comb. Flame* 2007, 151, 209–224.
43. Delfau, J.-L.; Bouhria, M.; Reuillon, M.; Sanogo, O.; Akrich, R.; Vovelle, C. "Experimental and Computational Investigation of the Structure of a Sooting Decane-O_2-Ar Flame," *Proc. Comb. Inst.* 1990, 23, 1567–1572.

44. Doute, C.; Delfau, J.-L.; Vovelle, C. "Modeling of the structure of a premixed n-decane flame," *Combustion Science and Technology* 1997, 130, 269–313.

45. Hanson, R.K.; Davidson, D.F.; Haylett, D.; Farooq, A.; Vasu, S.S.; Ranganath, S. In *NIST Fuel Summit*; ed., 2008; Vol.

46. Stouffer, S.D.; Heyne, J.; Justinger, G.; Ballal, D.; Pawlik, R.; Zelina, J. "Combustion Performance and Emissions Characteristics for a Well-Stirred Reactor for Low Volatility Hydrocarbon Fuels," American Institute of Aeronautics and Astronautics, 2007.

47. Bieleveld, T.; Frassoldati, A.; Cuoci, A.; Faravelli, T.; Ranzi, E.; Niemann, U.; Seshadri, K. "Experimental and kinetic modeling study of combustion of gasoline, its surrogates and components in laminar non-premixed flows," *Proc. Comb. Inst.* 2009, 32, 493–500.

48. Senkan, S.; Castaldi, M. "Formation of Polycyclic Aromatic Hydrocarbons (PAH) in the Methane Combustion: Comparative New Results from Premixed Flames," *Combust. Flame* 1996, 107, 141–150.

49. Wang, H.; Zhao, B.; Wyslouzil, B.; Streletzky, K. "Small-angled Neutron Scattering of Soot Formed in Laminar Premixed Ethylene Flames," *Proc. Comb. Inst.* 2002, 29, 2749–2757.

1. REPORT DATE (DD-MM-YYYY) 01-05-2011	2. REPORT TYPE Final Contractor Report	3. DATES COVERED (From - To)

4. TITLE AND SUBTITLE Experimental and Modeling Studies of the Combustion Characteristics of Conventional and Alternative Jet Fuels Final Report	5a. CONTRACT NUMBER NNC07CB45C
	5b. GRANT NUMBER
	5c. PROGRAM ELEMENT NUMBER
6. AUTHOR(S) Meeks, Ellen; Naik, Chitral, V.; Puduppakkam, Karthik, V.; Modak, Abhijit; Egolfopoulos, Fokion, N.; Tsotsis, Theo; Westbrook, Charles, K.	5d. PROJECT NUMBER
	5e. TASK NUMBER
	5f. WORK UNIT NUMBER WBS 561581.02.08.03.16.02

7. PERFORMING ORGANIZATION NAME(S) AND ADDRESS(ES) Reaction Design	8. PERFORMING ORGANIZATION REPORT NUMBER E-17292

9. SPONSORING/MONITORING AGENCY NAME(S) AND ADDRESS(ES) National Aeronautics and Space Administration Washington, DC 20546-0001	10. SPONSORING/MONITOR'S ACRONYM(S) NASA
	11. SPONSORING/MONITORING REPORT NUMBER NASA/CR-2011-216356

12. DISTRIBUTION/AVAILABILITY STATEMENT
Unclassified-Unlimited
Subject Categories: 07, 25, and 28
Available electronically at http://www.sti.nasa.gov
This publication is available from the NASA Center for AeroSpace Information, 443-757-5802

13. SUPPLEMENTARY NOTES

14. ABSTRACT
The objectives of this project have been to develop a comprehensive set of fundamental data regarding the combustion behavior of jet fuels and appropriately associated model fuels. Based on the fundamental study results, an auxiliary objective was to identify differentiating characteristics of molecular fuel components that can be used to explain different fuel behavior and that may ultimately be used in the planning and design of optimal fuel-production processes.The fuels studied in this project were Fischer-Tropsch (F-T) fuels and biomass-derived jet fuels that meet certain specifications of currently used jet propulsion applications. Prior to this project, there were no systematic experimental flame data available for such fuels. One of the key goals has been to generate such data, and to use this data in developing and verifying effective kinetic models. The models have then been reduced through automated means to enable multidimensional simulation of the combustion characteristics of such fuels in real combustors. Such reliable kinetic models, validated against fundamental data derived from laminar flames using idealized flow models, are key to the development and design of optimal combustors and fuels. The models provide direct information about the relative contribution of different molecular constituents to the fuel performance and can be used to assess both combustion and emissions characteristics.

15. SUBJECT TERMS
Aerothermodynamics; Chemistry; Combustion physics; Fluid mechanics thermodynamics; Gas dynamics; Aircraft fuels; Jet engine fuels; Synthetic fuels; Fuels; Chemical reactions; Hydrocarbon fuels; Liquid fuels

16. SECURITY CLASSIFICATION OF:			17. LIMITATION OF ABSTRACT	18. NUMBER OF PAGES	19a. NAME OF RESPONSIBLE PERSON STI Help Desk (email:help@sti.nasa.gov)
a. REPORT U	b. ABSTRACT U	c. THIS PAGE U	UU	74	19b. TELEPHONE NUMBER (include area code) 443-757-5802

Standard Form 298 (Rev. 8-98)
Prescribed by ANSI Std. Z39-18